ON THE APPLICABILITY OF SELECTIVE LASER MELTING ON PISTONS FOR THE OIL & GAS INDUSTRY

FATIGUE LIMIT AND FRACTURE TOUGHNESS OF SELECTIVE LASER MELTED TI6AL4V

by EA Niehaus

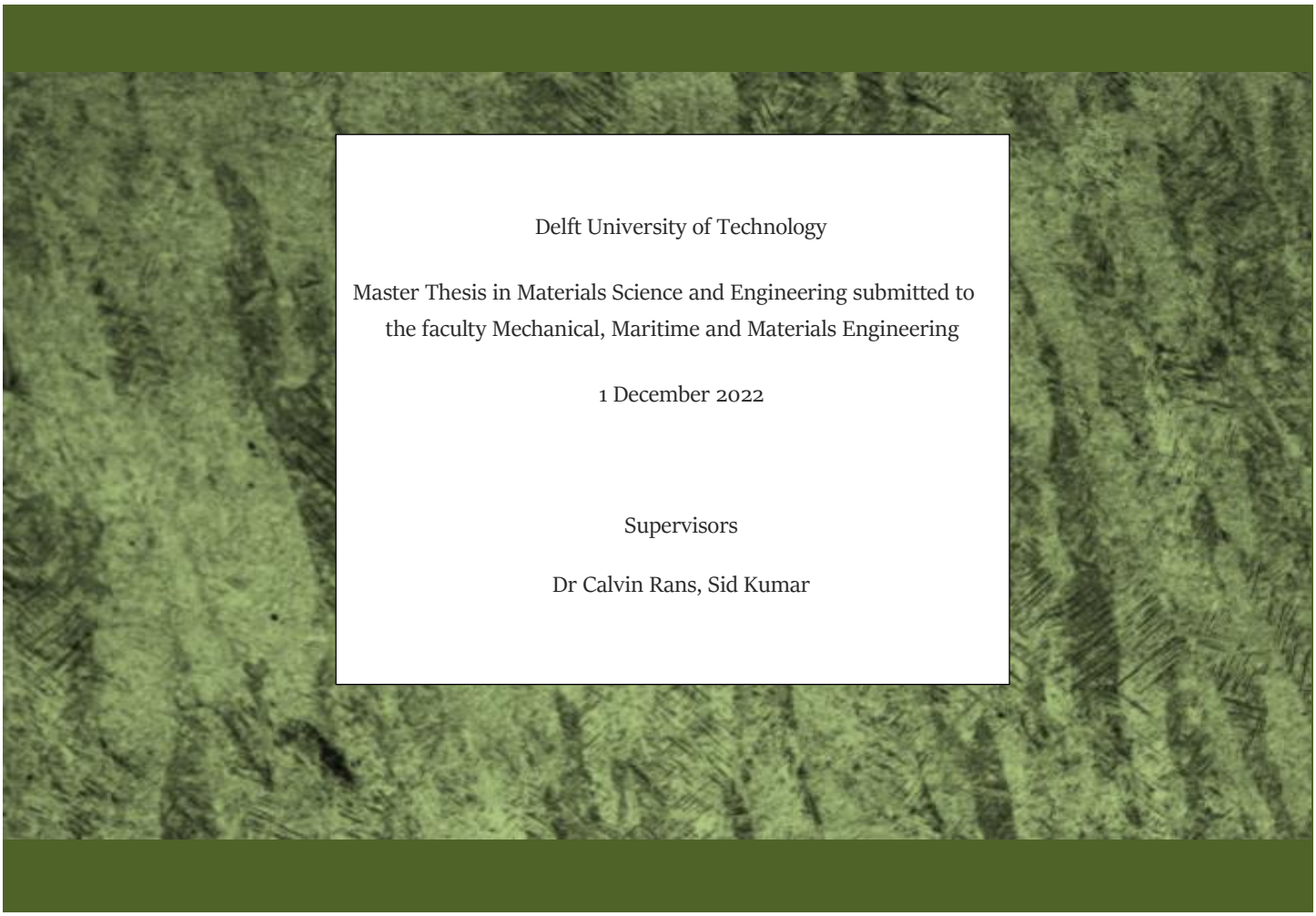

Delft University of Technology

Master Thesis in Materials Science and Engineering submitted to the faculty Mechanical, Maritime and Materials Engineering

1 December 2022

Supervisors

Dr Calvin Rans, Sid Kumar

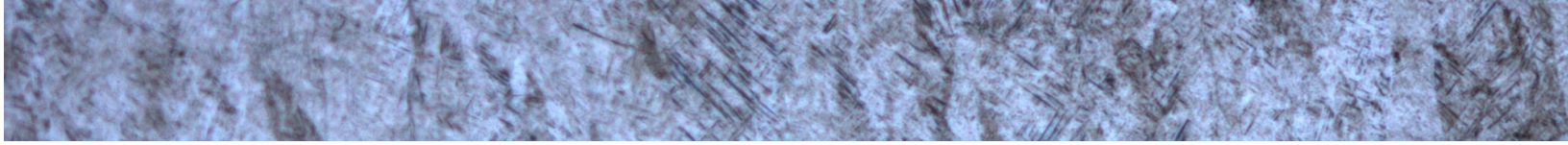

On the applicability of selective laser melting on pistons for the oil & gas industry

Fatigue limit and fracture toughness of selective laser melted Ti6Al4V

Abstract

Pistons for reciprocating compressors for industrial applications are often made of specialised materials. These prove to have problems with manufacture due to the high quality and short production times needed in combination with a low production volume per design. Additive manufacturing, specifically selective laser melting, could solve the production problems, provided that the material retains the needed mechanical properties. Ti6Al4V is the most appropriate material for this application. The most important mechanical properties for the application are the fatigue limit and the stress intensity factor, which are not well established properties for printed materials. For this reason fatigue limit and stress intensity factor tests were performed for both stress relieved and hot-isostatic pressed test pieces on longitudinal and transverse directions. Strength, toughness and fatigue limit is higher in hot-isostatic pressed test pieces of Ti6Al4V, and these are proven to be appropriate for application in compressor pistons. However the fatigue limit of stress relieved Ti6Al4V is lower, anisotropic, and has more scatter, and as such is insufficient for the application, which is due to deleteriously oriented microstructure and the presence of porosities. This can be solved by changing the printing parameters – laser power, cooling rate or heat treatment – although the exact combination of parameters for optimised values is not known and will be part-specific.

Table of Contents

List of figures

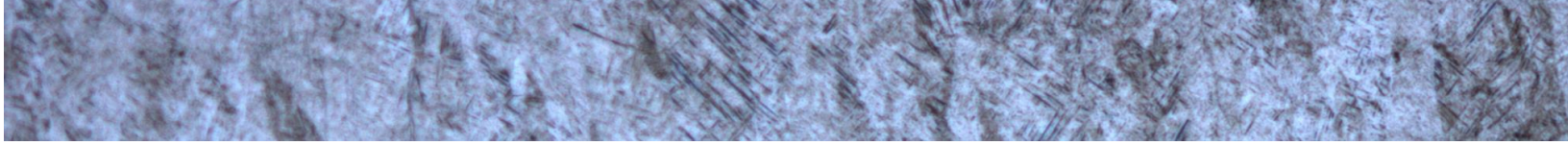

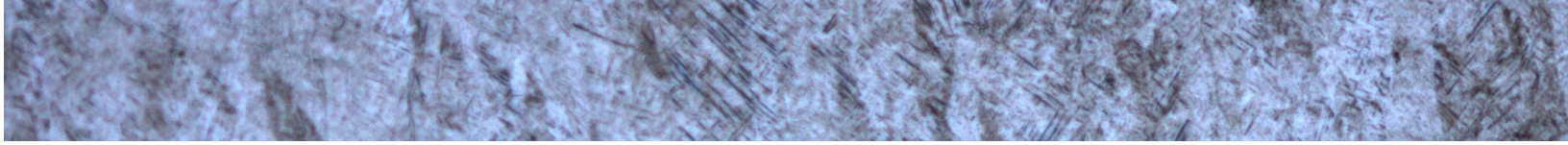

INTRODUCTION

Selective laser melting (SLM) has made substantial inroads into being an established technology for manufacture. As such it is being applied in aerospace, orthopaedics, tooling and niche manufacture, a long way from initially being dismissed as a prototyping fad. However some more conservative industries are still hesitant. Because selective laser melting is a relatively new technology, the full set of mechanical properties is not sufficiently known and reproducible, and the factors influencing these properties are not always clear. Until this is resolved the hesitancy will be difficult to put to rest.

The oil and gas industry specifically tends to be conservative in the application of new methods and materials, and applicability must be thoroughly proven. However due to the current instability in oil and gas there is more room to try out technologies that might not strictly be allowed according to the applicable standards, as long as they do the job and are economical. Additionally, suppliers to the oil and gas market are having to diversify into different markets, giving them the chance to broaden the processes they apply. This is also true for suppliers of large scale reciprocating compressors. The method of production for most parts of reciprocating compressors is largely settled, but for some parts, pistons in particular, there is room for improvement. These compressors, and so also the parts thereof, are custom-designed specifically for each intended application and tend to low volume production, seldom rising above single digits per design. This low production volume, combined with the properties needed for such a critical compressor part, lead to difficulties in finding an ideal production method. Traditionally pistons have been made by sand casting. This is ideally suited for low production runs, but is occasionally susceptible to casting defects. In addition the materials needed for more specialised applications are not particularly suitable for casting. Another often used option is machining the pistons from a solid forged block, but this is an expensive process with a large amount of material loss per piston. Both these methods have significant drawbacks, and tend to be used for the lack of anything better. SLM is ideal for parts with a low production numbers, without the problems posed by machining and casting, and gives a great deal of freedom in design that the others do not. However SLM also has its own drawbacks. Most significant of these problems is that the structure and properties of SLM materials are not as well-known as conventional materials. Some properties, most notably static strength, are known and give reproducible values, but while the strength of SLM materials is known to be high, toughness suffers correspondingly. Also fatigue behaviour, which is known to be affected by more factors than simple static strength, varies greatly between different studies.

Both fatigue and toughness are critical properties for successful operation of a compressor piston, so the parameters and underlying factors influencing these properties and contributing to their variation need to be determined in order to better predict the values from a given parameter set.

If SLM can be applied it could mean more economical fabrication, shorter delivery time, reduction in manufacturing defects and more control over design, ultimately enabling the rapid turnaround of high value parts. In order to facilitate this, the ultimate purpose of this study is exploratory research aimed at evaluating to potential of SLM in the context of reciprocating compressor pistons and to ascertain whether the drawbacks of SLM are insurmountable for this application, or whether it can be successfully be utilized now, or in the future.

Background

For a variety of reasons applications in oil and gas are faced with increasingly greater problems regarding corrosion. Reserves that are currently being exploited or explored are in more challenging, hence often more corrosive, conditions (Perez 2013). This in turn causes the need for more corrosive resistant materials. Also, due to the reduction in investment (Biscardini, et al. 2019) and current instability in the traditional oil and gas industry, suppliers of reciprocating compressors are looking further afield for promising markets, the conditions of which also mean different requirements for piston materials.

The more specialised materials pose problems for the manufacturing method traditionally used for compressor pistons, namely sand casting. Large production numbers would allow the casting moulds for more challenging materials to be optimised for successful casting, but the consistently unique designs coupled with low production numbers make this uneconomical. This causes issues like castings with cold shuts, porosity and residual sand inclusions. Castings defects in turn necessitate the use of various methods of non-destructive examination like magnetic, ultrasonic and in some cases radiographic testing, depending on the material. Testing adds more time and cost to a process that is already time-consuming due to time needed for preparation of moulds, casting, cooling, and on occasion heat-treatment. Testing can lead to additional unforeseen delays in cases where defects are encountered and need to be repaired. In the worst case the entire castings can turn out to be unusable do to critical defects and will need to be replaced at considerable cost, both financial and in terms of production time.

This unpredictability combined with the tendency to causing delays favour the use of machining, but some of the same reasons that pistons are suitable for casting cause problems for machining. The piston consists mostly of negative space, as can be seen in Figure 1, making machining a lengthy and expensive process. The depth and angles between the piston ribs in particular prove difficult to reach for machining bits. This leads to a substantial reduction in surface quality in those areas which is a problem for a part intended for dynamic loading.

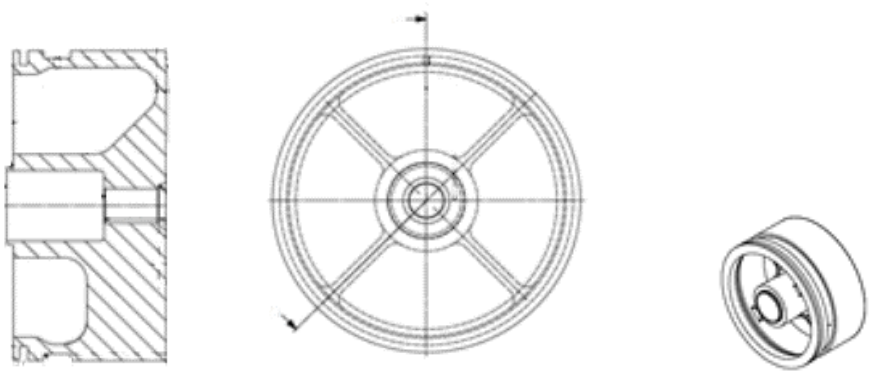

Figure 1: Drawing of a typical piston-half

Furthermore the design of pistons has long been optimised for casting, and changes made for ease of machining leave pistons heavier than before. This problem is even more significant with changing times where lowering the mass of moving parts is becoming more important for lower energy expenditure of the drivers, lower vibrations in the compressor, or to facilitate higher operating speeds.

A different solution is needed for the fabrication of reciprocating compressor pistons for specialised situations. The question is whether selective laser melting can live up to all the requirements of the application.

Reciprocating Compressors in the Oil & gas Industry

The oil and gas industry consists of upstream (exploration and extraction) and downstream (refining and transportation) activities. Oil usage world-wide is approximately 30 billion barrels (4.8 km^3) per year (CIA 2019).

Reciprocating compressors are applied both in upstream and downstream activities, including the compression and transport of (sometimes highly corrosive) petroleum gas instead of flaring, injection of gas into oil wells to maintain reservoir pressure, maintaining flow for pipeline gas transport, and hydrocracking. Many of these are crucial processes to plant operation, and while there will often be work-arounds and redundancies at a refinery, compressor down-time can cause a reduction in plant productivity or necessitate flaring, both of which are highly expensive. Refinery downtime, even for a modest refinery at low profit, can cause losses starting at €300 000 per day (Vukovich 2015). This means that failures must absolutely be avoided whenever possible, and when they do occur replacement parts need to be readily available. A plant of significant size may have spare parts on-site, but this is not always the case and is often not economical as parts are both unique and expensive, making it uneconomical to have a spare of every possible part. For this reason speed of manufacture becomes an important issue.

While current events have caused significant instability in the oil and gas market, the general trend before then has been downward. There has been a downturn in the oil and gas market for a number of years, bringing with it a reduction in investment (45% reduction in expenditure in upstream alone), and while the situation is no longer as dire as it was a few years before that, there also does not seem to be any clear signs that this that market is about to return to its earlier strength, current crisis notwithstanding. Furthermore reserves and profitable new discoveries are down (Biscardini, et al. 2019), necessitating exploitation of more challenging wells, as well occasionally diversifying into more corrosive processes like exploitation of oil sands and fracking.

The lower investment by the oil and gas industry means that suppliers to the oil and gas industry need to look further in order to remain competitive, and this of course includes suppliers of reciprocating compressors. Other applications that compressors are being applied in include LNG, CO_2 sequestration, polysilicone for solar panels, hydrogen for fuel cells and high-speed compressors for heavy industry. Each of these have their own challenges and requirement for compressor materials, like high corrosivity in CO_2 and potentially polysilicone due to chlorosilanes, and cryogenic temperature for LNG.

The reciprocating compressor and piston

The maximum allowable pressure and temperature and pressure of a reciprocating compressor is in the range of 300 bar and 180°C at a rate of around 400 rpm, although typically not all of these maximums are applied simultaneously. A typical example of a large scale reciprocating compressor can be seen in Figure 2.

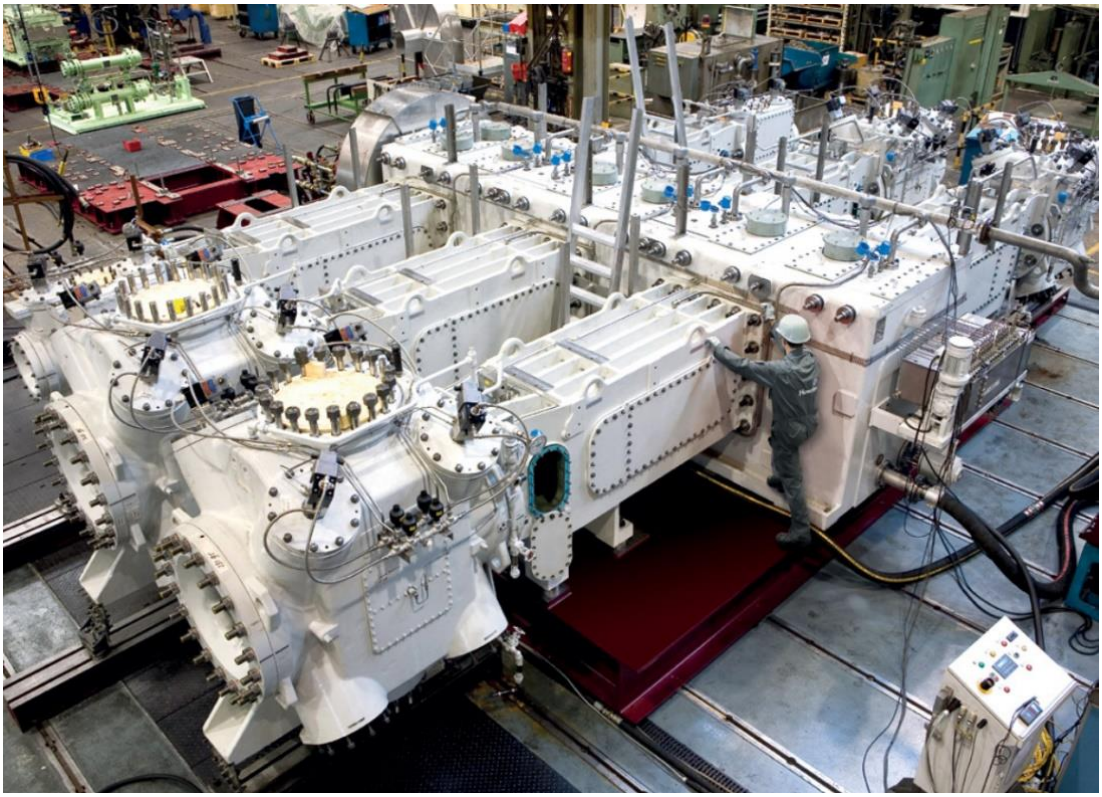

Figure 2: Howden Thomassen reciprocating compressor

The basic principle of operation of a reciprocating compressor is that of a positive displacement machine. Rotation, usually from an electric motor, turns the crankshaft, which in turn drives the crosshead which converts rotational movement to the linear movement of the piston rod, moving the piston in the compressor cylinder. This is the crucial point for the function of the compressor. Gas is delivered to the compressor by the plant at a given pressure as the piston moves to increase internal volume. At the point of highest volume the suction valves close and the piston reverses its motion to decrease volume, thereby increasing pressure (and temperature) until the piston reaches the extreme position and discharge pressure is reached causing discharge valves to open. In a dual action compressor, which these typically are, there are suction valves at both extreme positions of the piston, and compression on one side of the piston is simultaneous with the suction valves on the other side of opening. This means compression happens on both sides of the piston in contrapoint.

The end result of this is that the piston is subjected to complete reversed loading (from compressive to tensile and back) due to pressure differential from minimum to maximum pressure first on one side, and then the other, of the piston. Pre-tension is applied to the piston via the piston shaft in an attempt to keep the forces compressive, as well as to avoid relative movement between the compressor halves. The pre-tension induces a

substantial static load on the piston hub, but fatigue is still the dominating loading case, as well as the most frequent cause of failure.

Additionally sporadic shock loading can occur due to the occasional slug of incompressible fluid entering the compressor. This can cause catastrophic failure so a sufficiently high fracture toughness is needed.

Standards applied to reciprocating compressors in oil and gas

Apart from the material requirements determined by the application in general, compressors and the parts thereof also need to conform to a number of external norms and standard specifications.

For the oil and gas industry the most generally applicable standard is API 618, published by the American Petroleum Institute, which covers requirements for reciprocating compressors in oil and gas. It is based on accrued experience by both suppliers and operators of reciprocating compressors and serves to establish minimum requirements for all applications. It is applied to almost all large scale reciprocating compressors. In regard to the topic at hand, API 618 specifies the general quality of parts and the allowable methods of repair. More specifically cast iron, steel (forged or cast) or aluminium (forged or cast) is specified for pistons. In case of the presence of H_2S, API 618 refers to NACE MR 0175.

NACE (National Association of Corrosion Engineers) publishes standards on the topic of corrosion for a variety of industries. NACE MR 0175 and NACE MR 0103 cover prevention of embrittlement due to wet H_2S above a certain partial pressure in upstream and downstream applications respectively. Both standards are relatively rough guides, most significantly containing a list of materials and a required condition (usually just hardness) for each if wet H_2S (known as sour gas) is present above a given limit.

API 618 and NACE MR 0103 and 0175, being standards of American origin, all refer to American material standards and designations. These are AISI/SAE (American Iron and Steel Institute / Society of Automotive Engineers) and ASTM/ASME (American Society for Testing and Materials / American Society of Mechanical Engineers) designations. These may initially be American designations, but they are applied world-wide. There are however numerous countries that also have their own sets of material designations, as well as the European EN standards. The NACE standards have a procedure for having a non-listed materials approved, but for strict adherence to API 618 the given American material designations must be used.

It is however possible to take an exemption on certain points of the API 618 and still have it apply. More significantly, due to the downturn in the oil and gas market and compressor suppliers looking further afield, there is more of an inclination to produce compressors without the restrictions inherent to the specification.

Apart from these standard norms and requirements various compressor users and suppliers tend to have their own sets of requirements. An example of this is the Shell DEP (design and engineering practice) which can cover, add to, or take exemption to other standards.

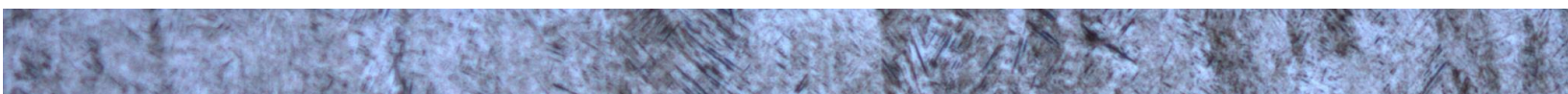

STATUS QUO FOR COMPRESSOR PISTONS

Piston halves for large scale reciprocating compressors vary from 300 mm to 1200 mm in diameter, with a typical depth of around 200 mm. They usually consist of a central hub, connected with a number of ribs to the outer rim for the distribution of force. Subsequently the highest load tends to be on the radius of the ribs. The ribs are also connected to the outer face which is the compressing surface. PTFE rings around the rim are the actual carrying contact with the cylinder liner. The amount and depth of the ribs may vary with the design, as may the outer diameter and depth.

Two piston halves are connected by the piston rod and pre-tensioned with a nut. The complete assembly can be seen in Figure 3. Sometimes an additional central segment is added, depending on the piston length required by the design.

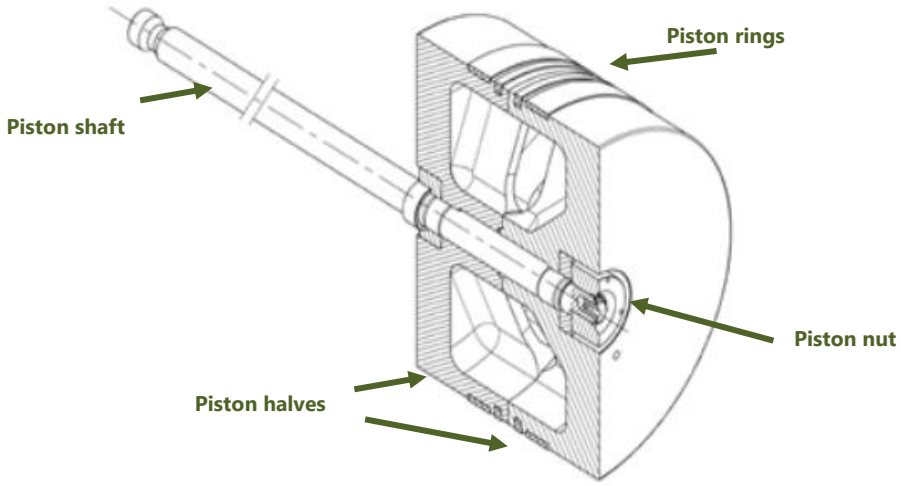

FIGURE 3: SECTION VIEW PISTON ASSEMBLY – PISTON HALVES MOUNTED ON PISTON ROD

The combination of this general design with the low production volumes needed is ideally suited for sand casting in cast iron. For most run-of-the-mill applications piston halves are cast from grey (flake) cast iron (according ASTM A278 as specified by API 618, or EN 1561 EN-GJL-250), for which only tensile strength is specified. For applications with slightly higher requirements ductile nodular cast iron (according to ASTM A395 as specified by API 618 or EN 1563 EN-GJS-400-15) is used, for which the graphite structure and full set of static tensile properties are indicated, as well as the toughness being specified by API 618. Both these materials have been in use for this application for multiple decades. As such their suitability is based as much on proven track record as on detailed quantified material properties. This can mean that introducing a new material is challenging, because they must be proven to be able to withstand the application, while there are limited quantifiable values to compare them to.

Moving away from cast iron, as becomes necessary for more challenging applications, brings with it problems with procurement. The combination of this design and general dimensions with the quality needed for the part and low production numbers make it difficult to find suppliers willing and able to produce compressor pistons.

Often the material and processes selection is based purely on the practical logistics of what is available (and economical), and not what the ideal material and production method would be.

There is a general trend toward lowering the weight of moving parts in order to reduce the energy needed from the drivers and to reduce the vibrational forces on the compressor as a whole. This is particularly important in the case of high-speed compressors. Weight reduction can be achieved either by applying a lightweight material, or using a material with a higher strength and reducing wall thickness to reduce weight.

For light-weight pistons the application of aluminium sounds like an easy solution, with the additional advantage of being applicable in more corrosive environments, barring the presence of mercury or chlorides. However is not without its drawbacks. Pure or low-alloyed aluminium alloys do not have a high enough yield strength to withstand the necessary pre-tension, while high-strength aluminium alloys (2xxx copper alloyed and 7xxx zinc alloyed series) have issues with lower corrosion resistance and lower fracture toughness. Silicon alloyed A13560 (AlSi7Mg) is usually applied for castings, but it can be challenging to find a foundry willing and capable of casting small runs of this material at the dimensions needed. While it is readily castable in general it has proven to have the inclination to form gas porosities throughout the material that can lead to sudden brittle failure, as well as an significantly lowered fatigue life. Adjusting the casting process to avoid porosities would require extensive modelling not feasible for the production volume. Simply machining a piston from a solid block is a solution, but there is a very limited amount of aluminium alloys available in the dimensions needed for a piston. Alloy 6082, a magnesium silicon alloy, and alloy 5083, which is a magnesium alloy that is specifically designed for low temperature service, are sometimes applied, but their mechanical properties are limited. Due to practical problems in procurement and the amount of failures in the field aluminium pistons are currently seldom applied.

A more commonly applied option would be high-strength martensitic stainless steel. It has sufficient corrosion resistance for most applications and is strong enough to allow pistons with a reduced wall thickness. It does however have to disadvantage of not being in the material classes specified for piston materials in API 618 and an explicit exception must be requested. X3CrNiMo13-4 is used due to the appropriate combination of properties. Traditionally this material has been sand-cast, but the unpredictable nature of casting and the challenging nature of the material requires extensive non-destructive examination in the form of magnetic and ultrasonic testing in order to find incidental casting defects, which then need to be repaired. This unpredictability causes scheduling problems on top of an already long production time and must be avoided. For this reason X3CrNiMo13-4 is often also machined from a solid block, even though the process is more expensive because of the sheer volume of material that must be machined away. Unfortunately piston design has long been optimised for casting and adjustment for successful machining leave the part heavier than before. The depth and angle in the radius between the piston ribs also cause problems with reach for the machining bits. This can partially be resolved by changes to the radius (leaving the piston even heavier) but still leaves a very rough-machined surface which is not ideal for a part loaded in fatigue. Another general issues it that this material is not available in the state prescribed by NACE MR 0175 and NACE MR 0103, which is a problem since it is used for applications with corrosive process gas, which in oil and gas very often means wet H_2S making NACE applicable. For this reason, after fabrication the piston half is subjected to heat treatment. On occasion this heat treatment does not yield the required results, making a near finished piston-half unusable, causing both delay and financial loss.

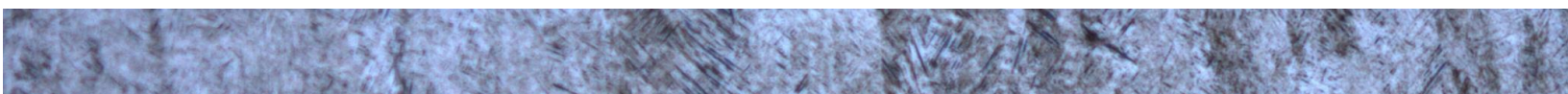

Austenitic cast iron, also known as Ni-Resist, is a range of cast irons with a nickel content of roughly 30%, depending on the alloy. It combines good castability and high corrosion resistance. Austenitic cast iron is not automatic permitted in any state according to the NACE standards, but can be used under certain circumstances. ASTM A439 D3A is used for pistons for very corrosive process gas, while ASTM A571 D2M is specifically designed for low temperature use and is applied for LNG compressors. Both however need a specialised foundry for casting. Non-destructive examination by magnetic and ultrasonic testing is not possible for these materials, leaving radiographic testing as the only option. It is not economically feasible to apply radiographic testing to every Ni-Resist piston so care must be taken with design to avoid possible defects during casting.

There are other materials that are applied for compressor pistons on occasion, but the above covers most applications. As can be seen there are various issues with the different materials and manufacturing methods, at least partially due to the low productions numbers and general shape. Additive manufacturing is most effective for low productions numbers, and the specific design and shape is no challenge this method of manufacture.

Literature Review

There are a variety of processes that can fall under the header of additive manufacture, including sheet lamination, material extrusion, binder jetting, and many others (ASTM International 2012). In fact additive manufacture is defined in contrast to more traditional methods of either casting or subtractive manufacture i.e. machining. The underlying idea is that of building a part or shape up layer by layer, ideally with minimal post-processing or shaping needed. The different methods use sheets, liquid, wire or powder as construction material, but all have in common that the end-part is built into near-final shape from the base up. For the sake of clarity the term 'additive manufacture' will subsequently be used as a catch-all term for the various material-incremental methods. The various forms of additive manufacture, including methods for producing parts from polymers or other materials are in modern parlance often known as 3D-printing.

Development of Additive manufacture

Additive manufacture originally started out as a method for rapid prototyping of models and prototypes, often of otherwise difficult to fabricate parts. It was often used both by students and medical professionals. Initially the go-to method was stereolithography, which is a liquid based curing process developed in the 70's. Rapid prototyping quickly gave rise to the idea of rapid manufacture, in other words using additive manufacture as a method for producing not just models, but functional parts.

Additive manufacture has several benefits over conventional methods of manufacture. The most significant of these is the greater design freedom. Factors that influence traditional manufacture like draft angles, ribs, radii and overhangs are no longer an issue (Gibson, et al. n.d.). This gives designers the freedom to focus more on design optimisation and lends itself to faster time to market in general (Brandt, et al. 2013). Once a CAD image of the part exists it must be converted to STL (from stereolithography) format. This format has become industry standard for additive manufacture and the process is included in CAD software packages. Following this the STL file needs to be segmented into layers, depending on size, necessary layer thickness, and build orientation. There are various programs available to build this layered file. Once this file is available the part can be directly manufactured. This is a far faster process than getting from design to finished part for a cast, machined or moulded part (D. Gu 2015).

The computing power used in forming the file the part is based in can also be used to find the component shape that complies with all the geometrical, structural and mechanical constraints while optimising the given objectives of the application, be they weight, strength any other. Due to the flexibility of additive manufacture the resulting design can be produced almost irrespective of shape, including shapes that would not be possible using conventional manufacturing (Brandt, et al. 2013).

While additive manufacture cannot compete on cost with methods used in mass production, with complex parts in low production runs there can be substantial savings (D. Gu 2015). There is essentially no material loss, and also indications that there might be a reduction in energy use (Brandt, et al. 2013), making for a more efficient method of manufacture.

Those advantages notwithstanding, for many industries the mechanical properties of polymers are simply not sufficient for functional parts. Practical application of rapid manufacture necessitates methods of producing metals.

Metals can be produced via additive manufacture by various powder or wire methods. Initially many high-melting point materials were produced by binder jetting (also known as Prometal), in which a liquid binder was locally added to bed of metal or ceramic powder, building up a green part that subsequently needed to be sintered. This quickly led to laser sintering, in which the sintering is inherent to the build-up process. Both these methods need post-processing in the form of hot-isostatic-pressing (HIP) or similar in order to reach useful mechanical properties and full density (Wong and Hernandez 2012), and even then are known to be brittle (D. Gu 2015).

The production of useful, finish-produced parts by rapid manufacture was only possible after the development of higher powered lasers (D. Gu 2015). The two laser melting (LM) methods available are laser metal deposition (LMD), also known as laser engineered net shaping (LENS), and selective laser melting (SLM), sometimes also known as direct metal laser sintering (DMLS), although this last is a misnomer, as it is a melting, not sintering process. One disadvantage of laser melting processes compared to laser sintering is that the degree of shrinkage occurring during solidification imparts significant residual stresses in the part (Gu, et al. 2012).

LENS is a process whereby the metal powder is deposited by means of a nozzle and locally laser melted. In this manner a part can be built of, or an existing part repaired or cladded, almost irrespective of size and shape, although in practice the process needs to be done in a sealed chamber for the best result. It also has the advantage of being able to vary the material used within a part by changing the powder being fed, giving the possibility of varying mechanical properties, or the ability to add wear or corrosion resistant coatings.

Wire-arc additive manufacture (WAAM) also works by feeding the material by means of a nozzle and locally melting it, only the form of the additive material is different – wire instead of powder. By means of WAAM a large part can be built up relatively quickly, even more so than with LENS, but the attendant surface quality and structure is worse, and there is less control over the process (Frazier 2014).

SLM, in contrast to LENS and WAAM, is a powder-bed method in which the laser melts only that section of the powder bed which in intended to become the finished part. This produces finer parts and sections, better surface quality and a higher as-printed tensile strength (Dutta and Froes 2017) than any of the other methods listed, but the process slower than LENS and WAAM (D. Gu 2015). With the currently available SLM machines the maximum printing chamber is smaller than is the case for LENS, although this could easily change in future.

Electron beam melting (EBM) is a very similar process than SLM, only using an electron beam instead of laser to melt the powder. Due to the nature of electron beams this is done in a vacuum, not under inert gas as can be used for SLM. This has a number of effects, most significantly that due to the vacuum convection is not possible, reducing the cooling rate, causing lower residual stress and creating a less strong but more ductile part. Another effect is the significant increase in cost due to the vacuum chamber itself (Dutta and Froes 2017).

EBM is not yet commercially widely available and at present only a very limited amount of materials can be produced with this method. The dimensions of parts that can be produced is very limited due to the vacuum chamber. For this reason it is not appropriate for commercial production of compressor pistons.

While LENS and WAAM have the advantages of quick production and large part size, relatively lower control over the process and low surface quality make it unsuitable for a critical machine part subjected to dynamic loading.

SLM, while a more expensive process than LENS and WAAM, has the higher control over the final product, as well as being attractive due to being a well-established method. This last is a very significant point. In order to have a commercially viable method of manufacture it must be readily available and the necessary factors and parameters for producing a given material in this method must be known.

The drawback is that the current wave of SLM machines cannot produce the largest in the range of compressor pistons, but is not an inherent problem with the process and there is no reason why this might not be remedied in the time it takes to qualify SLM for the application. And even if this is not the case, current trends in reciprocating compressor production is away from the very largest machines, which might make this a moot point in due time.

Selective Laser Melting

Selective laser melting is a powder bed based laser melting method, as the name implies. It was developed from laser sintering with the advent of high-powered lasers. Current SLM systems make use of CO2, Nd:YAG or fiber lasers usually of between 200 and 500 Watt.

A typical SLM system consists of a powder delivery system that transfers a layers of metal powder to the powder bed. The laser then scans and melts the necessary cross section for that layer in order to form the part. A schematic of this setup can be seen in Figure 4. Once this step is complete the powder bed is lowered and another layer of powder is added to be melted in turn. This all occurs in a closed chamber to avoid contamination of the powder bed, and this chamber can be filled with inert gas when needed, especially in the case of readily oxidized metals like titanium or aluminium. After a print is completed the loose powder still on the powder bed is recycled to be reused with subsequent prints.

There are different scanning strategies (i.e. the pattern by which scanning covers the surface of a layer and subsequent layers) that have significant impact on the thermal history of the part, which it turn influences the microstructure and hence the mechanical properties. Different printing parameters like the laser power, speed of scanning, hatch spacing, spot size and layer thickness similarly effects the properties of the part being printed. The quality (size and shape) of the powder particles can also have an effect (D. Gu 2015).

For the sake of consistency direction indicated by the laser will subsequently be referred to as the build direction or vertical direction, while the plane of the powder bed or build plate will be referred to as the build plane or horizontal direction.

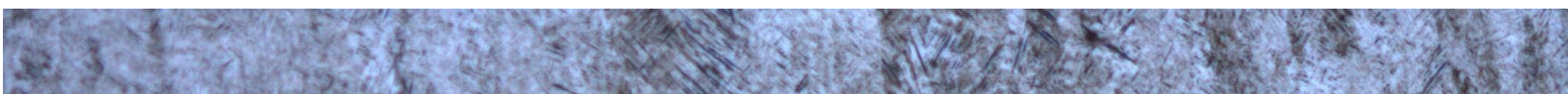

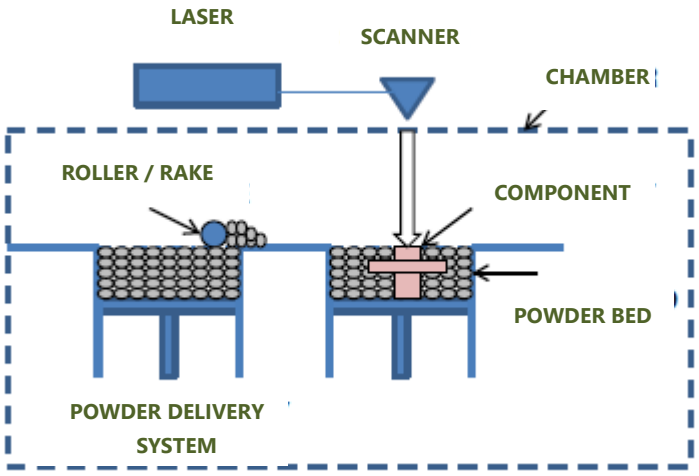

FIGURE 4: GENERIC SCHEMATIC OF SLM SYSTEM (FRAZIER 2014)

SLM gives great freedom of design, with the possibility of intricate structures like narrow internal channels, thin walls and fine features due to the small focussed laser beam and thin layers. Of all the metal additive manufacturing methods, SLM has the highest dimensional accuracy (approximately 40 µm) with a layer thickness of between 20 µm and 100 µm and as-printed surface roughness of approximately 10 µRa, depending on printing parameters (D. Gu 2015).

This method can be applied for a number of materials; essentially any metal or alloy which can be produced in powder form. However, the effects the process can have on the material must also be kept in account.

PROPERTIES OF SLM MATERIALS

There are a variety of factors that influence the mechanical properties of a SLM part, e.g. structure of the printed material and porosities therein and residual stresses due to the printing process. All of these are influenced by the printing parameters and the properties of the material on which it is based.

While there are a number of different printing parameters, like layer thickness, laser power, scanning strategy, spot size, scanning velocity, and hatch spacing, the overall effect of the parameters is often given as the by the energy density.

$E_d = P/vd$ [J/mm2] (Campanelli, et al. 2010)

where P is laser power, v is scanning velocity, and d is the laser spot diameter.

Campanelli et al. (2010) and Spierings, Wegenert and Levy (2012) showed for maraging steel and precipitating stainless steel respectively the density increases with energy density up to a certain point, before levelling off. However the details of how different kinds of porosities form are more complicated than that. Gas porosity occurs when trapped gas or moisture in the powder is released during printing, meaning that it is dependant both on powder quality and treatment. The printing parameters also have an effect - more laser power means more heat input into the part; meaning more

gas in solution to cause porosities. Lack-of-fusion defects are caused by an insufficient metallurgical bond between printed layers, making it a factor of laser power and layer thickness (Sun, Yang and Wang 2012). Furthermore porosity can be caused by instability in the melt pool due to hydrodynamic action, especially at low scanning velocity or high laser power (D. Gu 2015). Both melt pool instability and lack-of-fusion defects tend to cause a planar distribution of porosities (Brandt, et al. 2013).

Of course the ideal ratio of printing parameters is dependent on the material or alloy being printed. The solubility of various elements in the material, both in liquid and solid form, determines the possible extent of gas porosity. The ideal printing parameters to avoid lack-of-fusion defects and defects due to melt pool instability are in turn influenced by heat capacity, thermal conductivity, wettability of the solid, viscosity of the melt and the surface tension of the liquid, as well as the ratios of melting, solidification and sublimation temperatures. Another important factor is the temperature of printing, as well as the cooling rate as predicated by the temperature, shape of the part, printing parameters and material properties. Indeed, the cooling rate is significant for more reasons than just the effect on porosity, although porosity has a serious negative effect on the mechanical properties and general quality of a printed part.

There is a high temperature gradient between a small volume of melted metal and the partially fabricated part under it, which acts as a heat sink, causing rapid cooling. This in turn causes rapid solidification, and this localised volume change leads to the development of substantial residual stress (Cain, et al. 2015). This stress can be high enough to cause distortion or delamination of the part (D. Gu 2015). Additionally, the high cooling rate causes the formation of non-equilibrium microstructures to a degree which is not often found in traditionally fabricated material. The effects of this structure on the material properties is often not adequately described in literature.

In SLM, not just is the microstructure unfamiliar, so is the grain structure. The top of the initial grains are re-melted during the addition of every new layer, causing epitaxial growth which forms elongated columnar grains throughout the part. This structure is typical of SLM materials (Vilaro, Colin and Bartout 2011). These grains can be slightly angled in the direction of scanning due to conduction through the substrate causing directional cooling gradients, and so can also be influenced by the scanning strategy.

Due to all these different factors there is substantial anisotropy in the properties of SLM materials, and this can be dealt with in different ways. Stress relief heat treatment is often performed, which has the dual effect of reducing residual stresses and transforming the non-equilibrium microstructure into more conventional structure. This is only slightly complicated by the fact that it is evolving from a microstructure that is not found in conventional materials still has a not completely predictable effect on the resulting structure. A homogenisation heat treatment at higher temperature will completely remove this prior structure, as well as the columnar grains. Another very often used process is hot isostatic pressing (HIP) in which the part is exposed to high pressure at high temperature, closing most if not all porosities (D. Gu 2015).

While SLM is the most established method of metal additive manufacture, it is still a relatively new technology. As such it is not always entirely clear how all the previously mentioned factors – from material properties to various printing parameters - influence printing, and each of these factors would be worth a study as of themselves. As it is, suitable printing parameters are usually determined empirically, and not calculated by fundamental principles from the material properties.

Basis for material selection

In order to select an appropriate material the application must be considered with great care. The compressor piston is exposed to a challenging environment. It is subject to dynamic loading, corrosive gas, and, on occasion, extremes of temperature. The SLM piston will also be subject to this environment, and the chosen material will need to be able to withstand it.

Mechanical Properties

The most important property for a piston material to have is the ability to withstand the forces due to compression and other application-specific factors.

A minimum yield strength of around 200 MPa is needed to withstand the pre-tension applied to the piston, and a degree of stiffness is necessary for the piston to keep its shape and facilitate successful compression.

Resistance to shock loading, defined as toughness, is needed in order to withstand the forces inherent in starting up the compressor, as well as shock loading due to incidental ingress of fluid during operation. There are a number of methods by which toughness can be quantified, including various impact energy tests, of which Charpy V-notch is the most common, and stress intensity factor (K_{Ic}), which can be determined by a crack extension tests.

However the most significant property of a material for application for a compressor piston is resistance to fracture due to dynamic loading, i.e. fatigue strength. A reciprocating compressor should run for 10 to 20 years at a frequency of around 6 Hz. This puts the fatigue strictly in the high-cycle regime. While there are periodical stops for maintenance, removing the piston to check for cracks initiation is too expansive and time consuming to do on a regular basis. Monitoring for subcritical cracks is not feasible in this situation. So it becomes absolutely necessary to avoid crack initiation.

It should be noted that a low stiffness or strength or fatigue strength can be assuaged in some degree by increasing the wall-thickness, at the cost of an increase in weight, cost and processing time. Regions of high stress can avoided by redesign. The actual value of results of these properties are not as important, but scatter is. As long as you have precise and accurate stress and stiffness values these can be incorporated into the design.

Hardness is another property that has some bearing on the performance of a piston. The piston rings are usually fabricated from fibre filled PTFE and must be able to withstand the continuous rubbing contact. The various cast irons have relatively good wear properties due to graphite content, but for the other materials the resistance to wear must be provided by surface hardness. The various aluminium alloys often prove lacking in this regard.

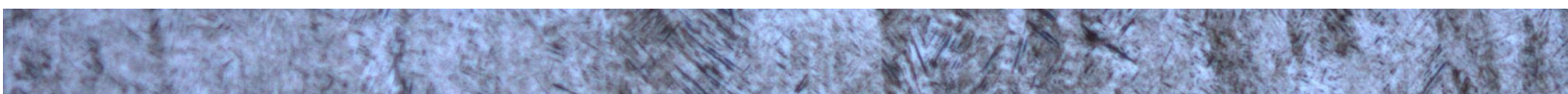

The values and properties listed in Table 1 are typically specified for purchase of the various piston materials. It is standard to report these as purchasing requirements according to EN 10204 (2004) and EN 10168 (2004).

TABLE 1: SPECIFIED MECHANICAL PROPERTIES OF PISTON MATERIALS ACCORDING TO ASTM A439 (2009), ASTM A571 (2006), ASTM B686 (2008), EN 586-2 (1994) AND EN 10250-4 (1999).

Material type	Alloy designation	Tensile Strength	Yield Strength	Elongation	Charpy V-notch Energy	Hardness
Nodular cast iron	EN-GJS-400-15	>415 MPa	>290 MPa	>10%	>14 J	130 - 200 HB
Cast aluminium	A13560	>275 MPa	>205 MPa	>3%	NA	>85 HB
Forged aluminium	6082	>310 MPa	>260 MPa	>6%	NA	>135 HB
Forged aluminium	5083	>270 MPa	>120 MPa	>12%	NA	>65 HB
Martensitic stainless steel	X3CrNiMo13-4	>650 MPa	>520 MPa	>15%	>50 J	<235 HB
Nodular Ni-Resist	A439 D3A	370 - 450 MPa	>210 MPa	>13%	>16 J	<190 HB
Nodular Ni-Resist	A571 D2M	440 - 480 MPa	>210 MPa	>25%	>24 J	<180 HB

There are a variety of other properties that are not tested for or specified, but still have a lesser or greater effect on piston performance. These properties are listed in Table 2.

Fatigue strength is probably the most important property for a part with high dynamic loading. Stress intensity factor, which is a measure of the material's resistance to crack growth, is an important factor, not for resistance against dynamic loading, but against total failure during shock loads. The relevance of stiffness and density have already been discussed in previous sections. Since light-weight pistons are favourable, not just density but specific strength needs to be considered.

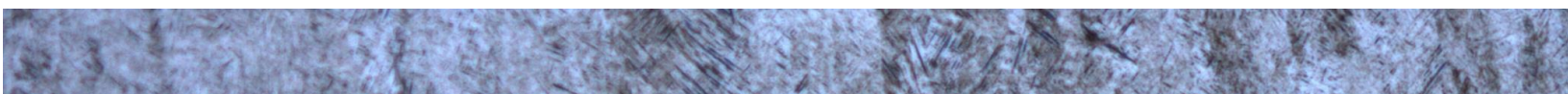

Table 2: Typical average material properties of piston materials from MatWeb LLC (2017), EN 13835 (2012), EN 1563 (2010), EN 1706 (2008), makeitfrom (2009), ASM International (1990), and Chen, Verreman and Lanteigne (2013).

Material type	Alloy designation	Density g/cm3	CTE x10^{-6} m/m°C	Young's Modulus	Fatigue Strength	K_{Ic} MPa√m
Nodular cast iron	EN-GJS-400-15	7.1	13	169 GPa	195 MPa	30
Cast aluminium	A13560	2.6	21	70 GPa	65 MPa	20
Forged aluminium	6082	2.7	23	69 GPa	95 MPa	41
Forged aluminium	5083	2.7	24	68 GPa	93 MPa	43
Martensitic stainless steel	X3CrNiMo13-4	7.8	10	200 GPa	350 MPa	245
Nodular Ni-Resist	A439 D3A	7.5	13	120 GPa	180 MPa	44
Nodular Ni-Resist	A571 D2M	7.4	19	130 GPa	180 MPa	44

Temperature can have a few different effects. In extreme cases the temperature difference between compressor start-up and full service can be up to 200°C. Typical cylinder and cylinder liner materials have a thermal expansion of around 13 x 10^{-6} m/m°C, and the piston rod of about 10 x 10^{-6} m/m°C. If the thermal expansion of the piston material differs significantly from this there can be problems with fit and seal of the piston in the cylinder liner, as well as changes to the pre-tension between the piston and piston rod. This last may be a contributing factor to the rate of failure of aluminium pistons.

An additionally problem is the effect of temperature on the mechanical properties. However the descrease in strength at high temperature and decrease in ductility and toughness and toughness is predictable and and can be taken into account in design calculations, as long as ductile-brittle is avoided.

Corrosion

Resistance against corrosion is one of the leading motivations behind compressor piston material selection. There are various compressor applications with inherent corrodents, like CO_2 in a compressor for carbon sequestration, or polysilicon compressor which has chlorosilane as process gas which will decompose to chlorides unless the gas is bone-dry. A refinery compressor can also have a variety of corrodents depending on how dirty the well is. H_2S is very common and can is some cases make up a significant proportion of the process

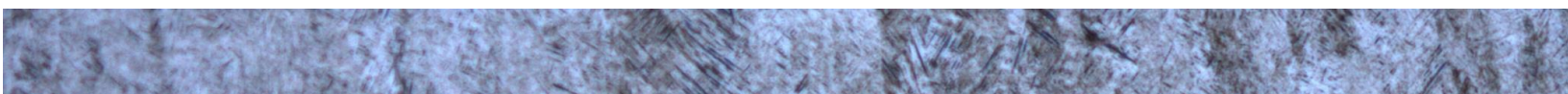

gas composition. The presence of H_2S can also mean the NACE MR 0103 or MR 0175 is applicable, further limiting the material. High strength steel is particularly vulnerable to embrittlement due to wet H_2S but in general if the rules mentioned in the NACE standards are adhered to, hydrogen embrittlement can be avoided.

Apart from hydrogen embrittlement, H_2S can also cause general surface corrosion. Some copper alloys are particularly susceptible, as is iron and steel, to a lesser degree. Corrosion by means of H_2S can be exacerbated by the presence of CO_2 which is also commonly present. Larger amounts of wet CO_2 can cause some corrosion issues with carbon steel and cast iron, but most other materials are not significantly affected.

Another common corrodent is chlorides. These can be very aggressive but fortunately usually only compose a few parts per million of the process gas. However even in this quantity it can still cause stress corrosion cracking austenitic stainless steels (ASM International 1990). At greater amounts corrosion rapidly becomes a more serious problem. While carbon and alloy steels and cast irons tend to uniform corrosion, aluminium and stainless steels show far pitting damage, which is potentially far more problematic and can cause unexpected rapid failure. Chlorides causes crevice corrosion in almost all metals, barring a few nickel alloys and precious metals.

Mercury can be present in rare cases, and then only in parts per million, although it may drop out of the process gas during compression and build up in the compressor. It only poses a problem for aluminium due to solubility.

Cost and Time

The cost of a material can vary to a great degree. In general the cost per weight of billet for aluminium alloys is five ten times higher than carbon steels, and magnesium alloys, stainless steels are copper are steadily more expensive in that order, with titanium and nickel alloys more expensive still (Beardmore 2010) (Dutta and Froes 2017). However cost per weight is not particularly helpful in comparing the costs of materials for a specific existing part. If you consider cost per volume instead, aluminium and magnesium alloys are suddenly barely more expensive than steel, and titanium alloys become more attractive compared to nickel alloys. In cases where specific strength is a design parameter titanium becomes even more interesting, although it remains an expensive material.

However the cost of a manufactured part consists of more than just the initial cost of raw material. Machining or casting are a substantial cost in and of themselves, and after rough machining or casting additional processing like heat treatment, final machining and non-destructive examination must also be added. As such for pistons the actual material cost makes out around 30 percent of part cost, depending on piston size and method of manufacture.

In comparison a SLM part the cost of raw material (in powder form) only makes out about 10 percent of the cost of the final part and a significant share of that 10 percent is processing the material into powder form. By far the largest share of the of a SLM part is the printing process itself – selecting a material that is readily printable will have a greater effect on cost reduction than choosing a cheaper material (Dutta and Froes 2017). Since material cost does not drive part cost for SLM, this opens up the opportunity for using materials that would be prohibitively expensive otherwise.

Material Choice

While it may be theoretically possible to produce almost any alloy by means of SLM, a successful print is dependent on knowing the appropriate set of printing parameters. If these are not known the part can end up with severe problems in term of porosities and bad bonding between printing layers, combined with very high residual stresses which in the worst cases can lead to the part warping or developing cracks.

An additional point is that the properties of materials produced by SLM is not necessarily the same as those produced via conventional methods of production. Purely looking at the tensile properties, the ultimate tensile strength tends to be higher, while the elongation is lower. Other properties are less well established and all may vary with printing parameters and post-production processing. This means the values can be very difficult to predict. For these reason it is necessary to look at the materials that are often applied for SLM and for which the printing parameters and factors influencing the properties of the final print are the most well-known.

The most commonly used materials for SLM are AISI 316L (austenitic stainless steel), Al10SiMg (aluminium alloy), Inconel 625 (nickel alloy), Ti6Al4V (titanium alloy) and M300 (maraging steel) (D. Gu 2015). Typical properties for these materials are listed in Table 3.

Table 3: Typical properties of commonly applied SLM materials, listed in rough order of base material cost (Renishaw 2019) (makeitfrom 2009).

Material	Tensile Strength	Yield Strength	Elongation	Hardness	Young's Modulus	Density	CTE x10^{-6}
Al10SiMg	380 MPa	240 MPa	4%	100 HV	67 GPa	2.7 g/cm^3	21 m/m°C
AISI 316L	650 MPa	520 MPa	39%	200 HV	194 GPa	8.0 g/cm^3	16 m/m°C
M300	1930 MPa	1890 MPa	5%	570 HV	210 GPa	8.1 g/cm^3	10 m/m°C
Ti6Al4V	1090 MPa	1000 MPa	15%	370 HV	128 GPa	4.4 g/cm^3	9 m/m°C
Inconel 625	1010 MPa	720 MPa	38%	330 HV	196 GPa	8.4 g/cm^3	13 m/m°C

The comparatively low strength and stiffness and high thermal expansion of Al10SiMg could pose problems in application for a compressor piston. It is also susceptible to problems with contact with known corrodents in the process gas like chlorides and mercury.

Austenitic stainless steel 316L has appropriate strength and stiffness values, and while the thermal expansion might be high, but it is not prohibitively so. In regard to hydrogen embrittlement it can be printed with suitable properties according to NACE MR 0103 and MR 0175 and has a generally good corrosion resistance. The only significant problem is the inclination to stress corrosion cracking and pitting in the presence of chlorides.

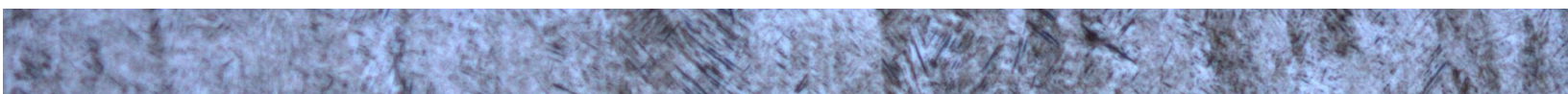

Maraging steel has high strength and is generally known for having high toughness, and has a good corrosion resistance. It is not explicitly mentioned in NACE MR 0103 and MR 0175 which is a problem in and of itself, and it is not possible to heat-treat it to a low enough hardness that it can be qualified for service according to NACE MR 0103 and MR 0175 according to the general rules for steel.

The good mechanical properties and low density of Ti6Al4V lead to very favourable specific strength and stiffness. Titanium alloys also tend to have a very good corrosion resistance. Ti6Al4V is mentioned in NACE MR 0103 and MR 0175 as being applicable for wet H_2S service with a maximum hardness of 36 RC (roughly equivalent to 354HV). Ti6Al4V as-printed via SLM is typically harder than this, but the value is reachable after heat-treatment. Additionally, both NACE MR 0103 and MR 0175 mention that for titanium alloys hardness it not known to correlate with susceptibility to hydrogen embrittlement and the maximum hardness levels specified are merely the highest hardness at which testing was performed. For this reason it could be quite feasible to take an exemption on NACE MR 0103 and MR 0175 on the matter of maximum hardness in the presence of wet H_2S.

Inconel 625 has strength and stiffness and excellent corrosion resistance. Like Ti6Al4V it is not printed directly in a state directly suitable for wet H_2S service according to NACE MR 0103 and MR 0175, but it can be heat-treated to the appropriate condition.

Of the most commonly fabricated SLM materials, Inconel 625 and Ti6Al4V are the best all-round options for pistons for reciprocating compressors. They have comparable corrosion resistance, and both metals are sufficiently refractory to be applied at high temperature, and both lack a ductile-brittle transition and can be applied at low temperature.

Ultimately the low density of titanium gives the advantage with high specific strength and stiffness, as well as the possibility of taking exception to the hardness rules of NACE MR 0103 and MR 0175. Another distinct advantage of Ti6Al4V is that of all materials used for SML, it has been the most fully researched by far (Frazier 2014), making it far more likely of finding the necessary information to evaluate it as a potential material for application, and increasing the likelihood of being practically feasible to produce a successful print.

Details on Ti6Al4V

The high strength and low density, combined with a good corrosion resistance, makes titanium a very attractive, if expensive, material. Commercial alloy Ti6Al4V is the most commonly used alloy, which can be attributed to the combination of toughness and strength, as well as the good corrosion resistance native to titanium. The most notable applications are medical, due to the high degree of biological compatibility, and aerospace, due to the combination of high strength and low density (Brooks 1990).

Pure titanium is composed of hexagonal alpha (α) phase at room temperature, transforming to body-central-cubic beta (β) phase above 882°C. However alloying elements influence phase transformation, and for this reason there exists not only α phase titanium alloys, but also mixed dual-phase α and β alloys, as well as alloys that are completely β at room temperature. Commercially pure titanium grades (which, apart from Ti6Al4V tend to be most commonly used) can be strengthened by interstitial solutions of hydrogen, nitrogen, carbon or oxygen, but these remain the weakest class of titanium alloys (Budinski and Budinski 1999). Somewhat

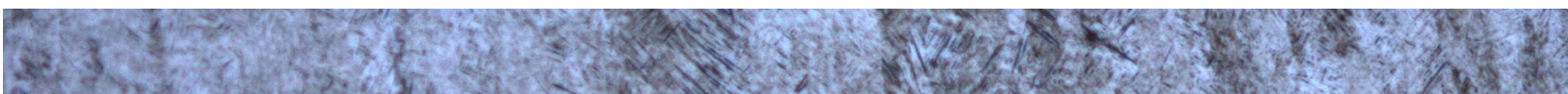

stronger are the alpha alloys, which are strengthened with by means of solid solution with additions of alpha stabilisers like aluminium and tin, or even small amounts of beta stabilisers like copper. Vanadium is a beta stabiliser (Pederson 2002), causing Ti6Al4V to be an alpha-beta alloy. Alpha-beta alloys and heat treated beta alloys (with significant additions of vanadium and molybdenum) are the strongest forms of titanium, while un-heat-treated beta alloys are more ductile with good formability (Budinski and Budinski 1999).

Ti6Al4V has beta transus at around 995°C (Murr, et al. 2009), and the percentage of alpha phase increases when cooling from β transus, but does not become full alpha even at room temperature. After very slow cooling from above the beta transus temperature the primary structure tends to be globular alpha (Figure 5). Increasing the cooling rate enhances α nucleation rate at β grain boundaries (Pederson 2002). Alpha tends to form with the basal plane of the structure parallel to the {110} plane of the β phase. Since the grains grow more quickly along this plane than perpendicular to it this forms lamellae (plates) of alpha, sometimes known as the Widmanstätten structure (Figure 6).

Figure 5: Globular Ti6Al4V (Moyka, et al. 2012)

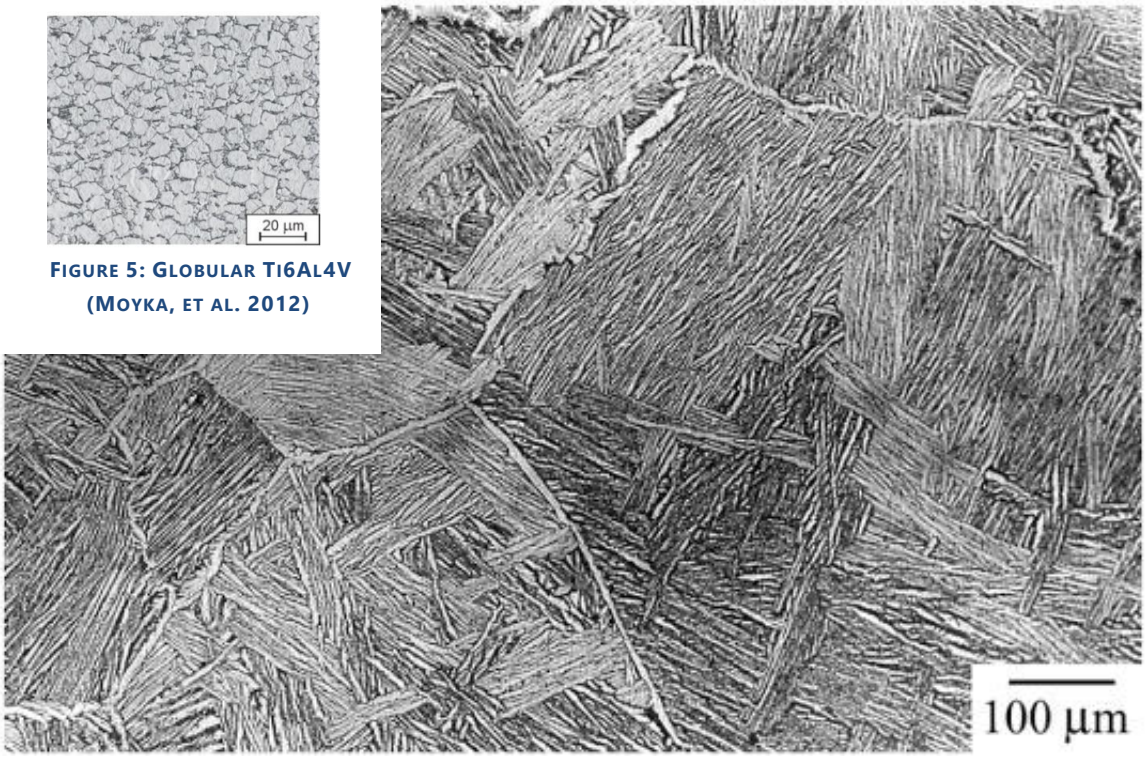

Figure 6: Lamellar Ti6Al4V with large prior beta grains visible (Joshi 2006)

However at faster cooling rates α phase does not have the opportunity to form, instead forming a fine acicular hexagonal martensite (α') which can be seen in Figure 8. This is a non-equilibrium structure, of which titanium has a few. However commercial Ti6Al4V is rarely produced as martensite. Far more typical is lamellar α+β, which by means of deformation (to break up the lamellas) and recrystallisation can also be transformed into a bimodal combined (Figure 7) or even back to fully equiaxed (globular) structure (Lütjering,

J.C. en Gysler 2002). Another option is aging of lamellar Ti6Al4V, causing strengthening by precipitation of coherent Ti_3Al particles or alpha phase (Budinski and Budinski 1999).

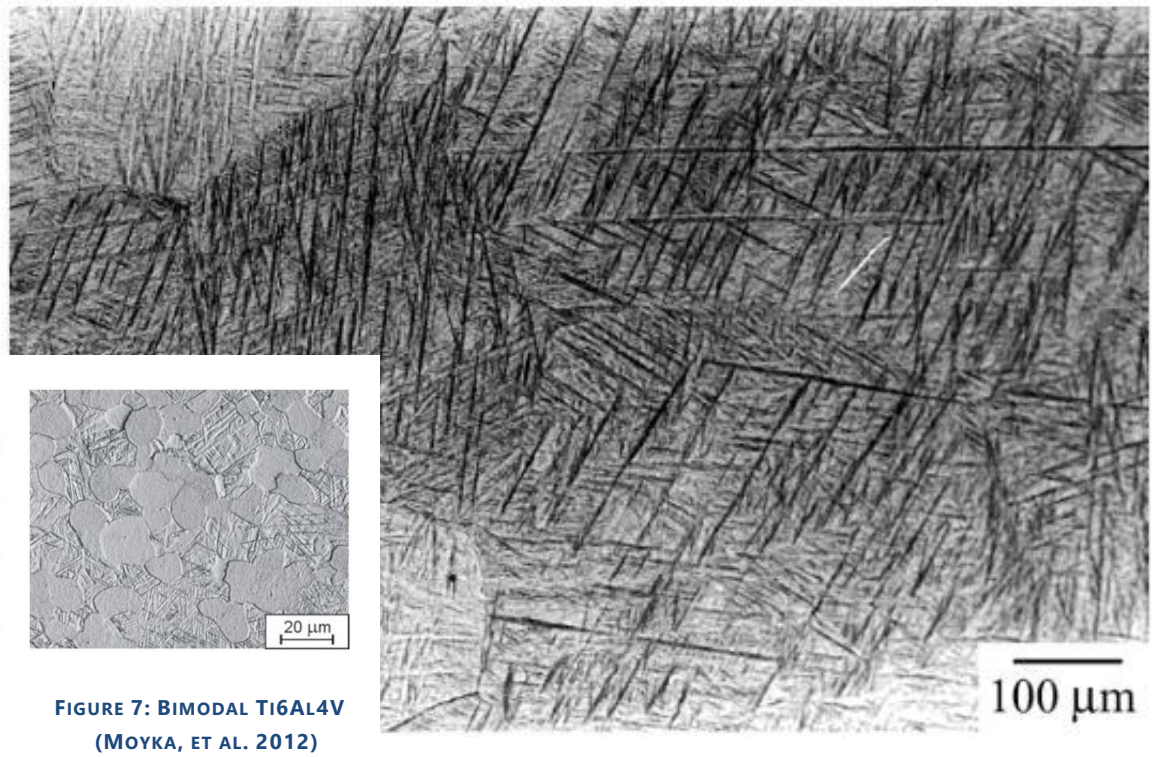

Figure 7: Bimodal Ti6Al4V (Moyka, et al. 2012)

Figure 8: Ti6Al4V Martensite with large prior beta grains visible (Joshi 2006)

The general mechanical values of Ti6Al4V vary based on the structure, but typical values are well known and shown in Table 3. However these are not the most significant for the application in question. The fatigue strength and toughness are far more relevant values. These can be seen in Table 4.

Table 4: Typical relevant properties of wrought Ti6Al4V (MatWeb LLC 2017) (Titanium Information Group 2002).

Properi	Fatigue Limit [MPa]	Stress intensity factor [MPa√m]	Charpy V-Notch [J]
Ti6Al4V	510 - 690	43 - 107	9 - 24

There is considerable spread in these values, most of it caused by the different properties of the different possible states of microstructure. It is known that a fully lamellar structure has higher fracture toughness, while bimodal Ti6Al4V tends to have a better high-cycle fatigue life (Cvijovic-Alagic, et al. 2014).

As is the case with tensile strength, the fatigue limit is favourable in comparison with conventional piston materials. Likewise the stress intensity factor is high, but the Charpy value is low in comparison. This is odd

since the Charpy value and fracture toughness are both indications of the toughness of a material, and it would be expected that they scale together. Nevertheless, when looking purely at these mechanical properties Ti6Al4V could be applied for pistons given the stated requirements. However these values are for wrought Ti6Al4V. In the case of SLM Ti6Al4V the situation could be very different.

Selected laser melted Ti6Al4V

The general microstructure and characteristics of SLM Ti6Al4V is comparable to fast-cooled wrought Ti6Al4V, with a few notable differences. The most readily noticeable are the elongated columnar grains that are characteristic of the SLM process, as can be seen in Figure 9.

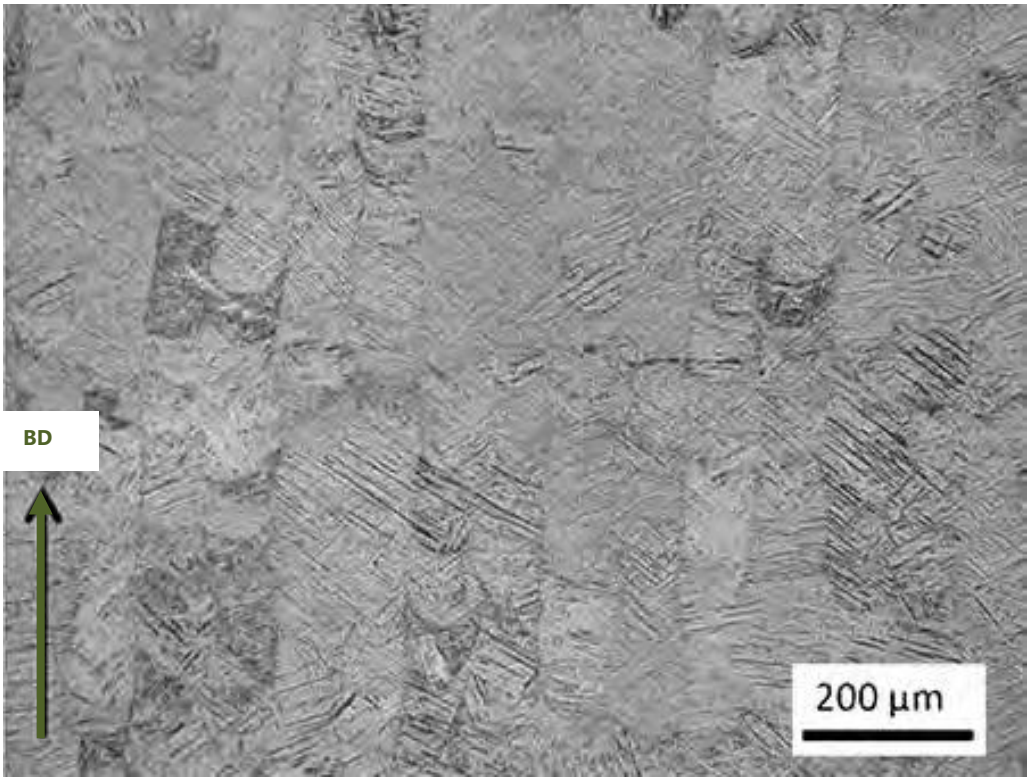

Figure 9: Columnar prior beta grains of SLM Ti6Al4V, build direction (BD) indicated (Cain, et al. 2015)

Cooling rates during printing are very high and directional, leaving the columnar grains and high residual stresses, which can be up to 200MPa surface tensile stress in the vertical direction (Cain, et al. 2015). This would largely be due to the large amount of high density defects and dislocations, twins, and the material could additionally contain some hard, brittle alpha due to tramp O_2 and N_2 (Huang, et al. 2016). These defects can have a serious impact on the mechanical behaviour so it is customary to remove the residual stresses by a stress relief heat treatment (Edwards and Ramulu 2014).

The fast cooling from melting that is inherent to SLM gives rise to non-equilibrium microstructures. As-built (so not heat-treated or HIP) Ti6Al4V is mostly composed of martensite, which is hexagonal α', and possibly some orthorhombic α'' (Vrancken, et al. 2012) (Donachie 2000). This is the mechanically hardest structure Ti6Al4V can reach, but the corresponding toughness and ductility is very low (Brooks 1990). After stress relief

the martensite will decompose to acicular α/β, or, if heat treated or HIP at close to the beta transus temperature, further to lamellar α/β (Cain, et al. 2015). As-built and heat treated Ti6Al4V can be seen in Figure 10. Apart from changing the structure, HIP will also get rid of most porosity. Heat treatment at temperatures sufficiently above the beta transus temperature will break-up the columnar prior beta grains, leaving a equiaxed structure (Huang, et al. 2016).

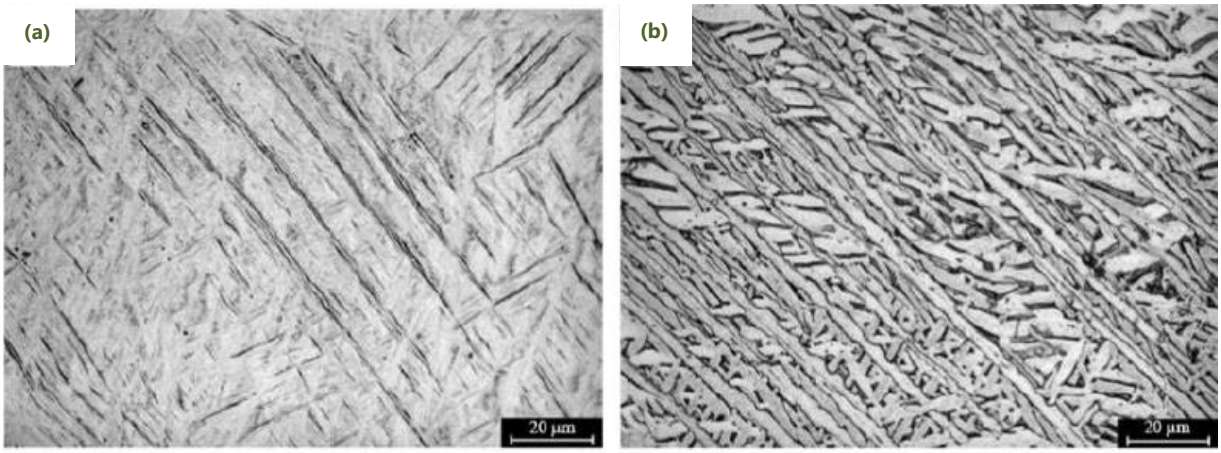

FIGURE 10: MARTENSITIC (A) AND LAMELLAR (B) SLM TI6AL4V (GU, ET AL. 2012)

The microstructure of SLM Ti6Al4V is complicated by the phase transformation and dual phase system at lower temperature. As can be seen the various factors making up the structure of SLM Ti6Al4V are quite complex. However the chief interest is the response of the relevant mechanical properties.

MECHANICAL PROPERTIES

Mechanical properties of Ti6Al4V are known to be sensitive to the microstructure, in particular the prior β grain size, α/β morphology, α grain size (thickness and length) and α cluster size, all of which are formed by prior thermal processing, which in turn is a factor of the printing parameters and subsequent treatment. Complex mechanical behaviour like high-cycle fatigue behaviour is known to be particularly sensitive to these factors, while tensile strength is a more stable property (Hosseini 2012). One issue remaining is that studies seldom publish the full set of printing parameters, making it difficult to compare and predict values, or to determine the influence of different factors.

The tensile strength of as-built Ti6Al4V between 1050 MPa and 1250 MPa, with most studies finding results well into the higher end of the range (Yan, et al. 2018). Tensile test pieces printed vertically also consistently have somewhat lower strength than piece printed horizontally (Qiu, Adkins and Attallah 2013). This remains the case for heat treated and HIP tests, the only difference that the strength becomes continuously lower with higher temperature of heat treatment, with the lowest strength noted is around 850 MPa at heat treatment over 1000°C (Yan, et al. 2018). These values are easily sufficient for application for a compressor piston.

In general strength and ductility tend to be opposing values. We can therefor expect as-built Ti6Al4V to have the lowest toughness, and this is born out in the results. However a more significant

problem is the degree of spread in the values in terms of printing direction, printing parameters and post-printing treatment. In fact, while the average stress intensity factor taken over all results from different papers[1] is a perfectly serviceable 48 MPa√m but the coefficient of variation (the ratio of the standard deviation to the mean) of these values is over 30%. Doing the same for toughness measured by Charpy impact test gives a (rather low) average of 14 J with a coefficient of variation (CV) of over 70%.[2] In comparison, when doing the same for ultimate tensile test the CV is only 9%.[3]

In the case of high-cycle fatigue the problem with spread is even worse. While both (Frazier 2014) and (Dutta and Froes 2017) report that the fatigue limit of printed Ti6Al4V is higher than that of wrought Ti6Al4V, they both quote secondary sources to do so, and these results are not born out when various studies are consulted. Unfortunately studies performed on the high-cycle fatigue performance of SLM Ti6Al4V are performed with different R values, different surface condition of the test pieces, and different types of test pieces sizes, along with variation in the factors that have been previously mentioned to influence the mechanical properties of this material. This makes it very difficult to compare the values, something that is exacerbated by the fact that there seems to be some doubt as to whether the Goodman criteria is applicable to Ti6Al4V (Peters, et al. 2000). However, just to get an indication of the spread, when converting the available values to the equivalent R=-1 alternating stress, the high-cycle fatigue limit varies between 56 MPa (Edwards and Ramulu 2014) and 620 MPa (Leuders, Thöne, et al. 2013). 620 MPa compares well with the fatigue limit of wrought Ti6Al4V, but both these values are outliers.

This degree of variation is a problem. While it is possible to ameliorate the effects of low fatigue strength by adjusting the design, you do need to know what the fatigue strength of the part is. For both the high-cycle fatigue limit and the fracture toughness, we need more information on which factors influence the values and in which ways. A couple of factors are clear. As-built parts are low in ductility and are therefore significantly lacking in both toughness and fatigue strength, since ductility is a factor in the susceptibility to fatigue crack initiation (Leuders, Vollmer, et al. 2015). Another is that values improve after heat treatment or HIP. However this is not enough information to predict the mechanical behaviour of a printed part.

The combination of residual stress, porosity, texture, and strongly directional macro- and microstructure leaves a material that shows significant anisotropy in the mechanical properties. Furthermore, the relative impact of these properties change for different sets of printing parameters

---

[1] Results of fracture toughness testing from Cain, et al. (2015), Kumar, Prakash and Ramamurty (2018), Van Hooreweder, et al. (2012), Edwards and Ramulu (2014), and Hartunian and Eshraghi (2018) which itself is a compilation of various sources.

[2] Results of Charpy V-Notch impact testing from Wu and Lai (2016) and Yasa, et al (2010).

[3] Results of tensile testing from Cain, et al. (2015), Rafi, Karthik, et al (2013), Qiu, Adkins and Attallah (2013), Kumar, Prakash and Ramamurty (2018), Simonelli, Tsea and Tuc (2014), Leuders, Thöne, et al. (2013), Hartunian and Eshraghi (2018) and Yan, et al. (2018).

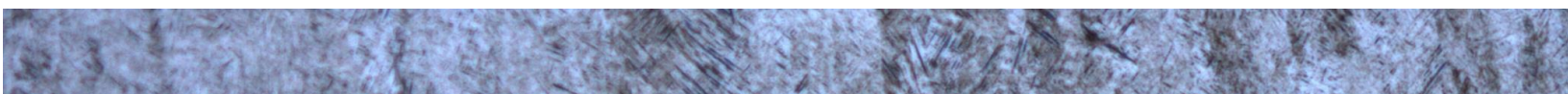

and states of heat treatment. This makes the mechanical properties of SLM Ti6Al4V difficult to predict and great care must be taken determining these properties.

Initial Conclusions

At the moment rapid manufacture is not often used for parts in heavy industry. It is considered too expensive, printed materials are commonly held to not have sufficient mechanical properties, and the dimensions of parts that can be printed are limited. However there is potential for use due to problems manufacturing compressor pistons for special applications, and the logistical drawbacks are not necessarily limiting in this case.

Selective laser melting appears to be suitable for high-performance parts in dynamic loading due to the level of control over the structure, and due to being a more well-established method than other techniques of rapid prototyping. Ti6Al4V is the appropriate material to be manufactured by SLM for compressor pistons due to high strength, toughness and corrosion resistance.

Ti6Al4V manufactured by means of selective laser melting appears to be appropriate for the range of relevant applications of compressor pistons. Additionally Ti6Al4V is a well-established material to be fabricated by means of SLM.

The goal is to investigating key mechanical properties to see if this assumption is true. While the mechanical properties on average are sufficient for the application, there is considerable spread in the critical properties of high-cycle fatigue strength and fracture toughness. We need to have a better understanding of the connexion between the printing parameters, post-printing treatment, microstructure and the resulting mechanical properties. When these links are understood we have a better chance of being able to print parts secure in the knowledge that the mechanical properties are known and consistent.

EXPERIMENTAL METHOD

The mechanical properties of Ti6Al4V in general are appropriate for application for reciprocating compressor pistons. However the same cannot conclusively be said for the properties of selective laser melted Ti6Al4V. While the tensile properties are sufficient, other properties give more varied results. Toughness and fatigue strength in particular are critical for the application of a material for compressor pistons. Meanwhile these properties are strongly dependant on the various factors involved in SLM and vary significantly between different tests. For this reason SLM Ti6Al4V was tested in different conditions (stress relief heat treated and hot-isostatic pressed) and the effect, not just on the strength, fatigue strength and toughness, but also on the microstructure and fracture surface was examined. By performing tests on test pieces printed in different orientations the interplay between microstructure and mechanical properties can also be examined due to the strong directionality of the microstructure in the printing direction.

MATERIAL PROCESSING CONDITIONS

All tests were performed on selective laser printed test pieces of Ti6Al4V. Printing was performed in two batches with identical printing parameters. They were printed in a checkerboard pattern to distribute the heat input and reduce internal stress. The scanning strategy can be seen in Figure 11.

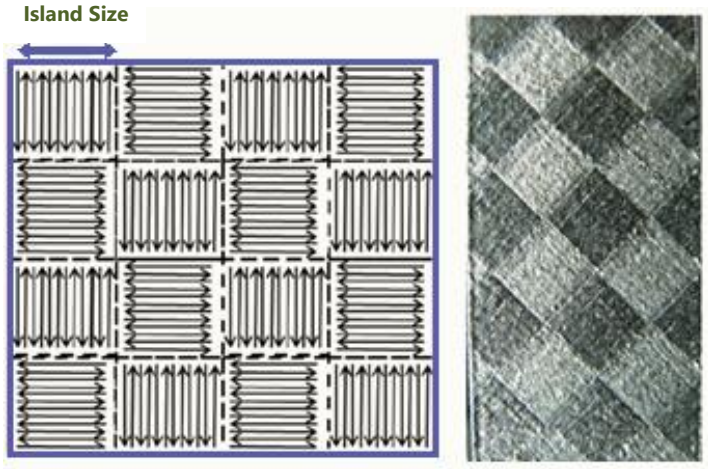

FIGURE 11: SCANNING STRATEGY AND THE RESULTING CHECKERBOARD PATTERN (QIU, ADKINS AND ATTALLAH 2013).

Hatch spacing is 0.12 mm with a layer thickness of 50µm, laser power 275W and scan velocity 975 mm/s. Island size is 5 mm. Due to the negative effect of residual stress due to printing on ductility, toughness and fatigue limit, the test pieces were stress relieved at 735°C for 2 hours in inert gas followed by rapid cooling. This will be referred to as the 'stress-relieved' (SR) condition from here on. After stress relief half the test pieces were subjected to hot-isostatic pressing at 920°C and 1000 bar for 2 hours followed by furnace cooling. These test pieces will be referred to as 'HIP'.

Although He, et al. (2018) claims that as-built (so without heat treatment or HIP) Ti6Al4V has sufficient ductility for practical application, all their test pieces were printed in the transverse direction to avoid known longitudinal residual stresses so applicability cannot said to be proven. The consensus is that the high residual

stress in as-built Ti6Al4V makes it unsuitable for practical application and as such as-built test pieces will not be tested here.

There are two sets of test pieces for both stress relieved and HIP. The transverse (or horizontally printed) test pieces where the crack growth will be into the plane of the build plate (i.e. vertical), and longitudinal (or vertically printed) where the crack growth will be parallel to the plane of the build plate (i.e. horizontal). These test pieces are shown in Figure 12.

Figure 12: As-printed orientation of transverse (left) and longitudinal (right) test pieces

During discussion of results horizontal and vertical will refer the directions compared to the test-pieces as printed, i.e. referring to the image above. When necessary the results of the various sets of test pieces; stress relieved or HIP, transverse or longitudinal, were compared by means of analysis of variance (ANOVA) to check whether the differences were statistically significant.

General

Microstructural Analysis

Optical microscopy was performed on both stress relieved and HIP test pieces.

The test pieces were mechanically polished with SiC grinding paper up to 4000 grit, followed by electropolishing in a Streurs Lectropol-5. Electropolishing was performed in a 59% methanol, 35% ethylene glycol butyl ether, 6% perchloric acid (at 65%) solution. Polishing parameters were 25 V for 40 s at a flow rate of 10. Electropolishing was followed by etching with Kroll's Reagent.

In order to track the influence of the microstructure in crack development samples were taken orthogonal to the crack direction. Test pieces were prepared by mechanical polishing with SiC grinding paper up to 4000 grit. followed 12 hours in a Vibromet. Electropolishing was not used in this case due to edge effects of polishing interfering with the crack edge. These were investigated by optical microscopy and SEM.

Electron Backscatter Diffraction

Electron backscatter diffraction (EBSD) was performed on test pieces after preparation by means of mechanical polishing with SiC grinding paper up to 4000 grit., followed 12 hours in a Vibromet. The general microstructure was examined.

Fractographic Analysis

Fracture surfaces were first captured photographically to get an overview of the entire surface. Subsequently features of interest identified in original fractography were investigated under the SEM. Additionally, SEM images were taking at varying magnifications close to the crack initiation point (in those cases where it could be identified) and at various points from initiation to the end of the fracture surface. The fracture surfaces were examined for a general impression of the structure of the material, as well as in regard to specific features in regard to toughness and fatigue fracture.

Hardness testing

Vickers hardness testing was performed with a Streurs Durascan with either 1 kgf or 0.2 kgf, depending on the test. Hardness testing was performed on the same test pieces used for microstructural analysis.

Tensile testing

Dog-bone test pieces (Figure 13) with a thickness of 2 mm were used for both fatigue and static tensile testing.

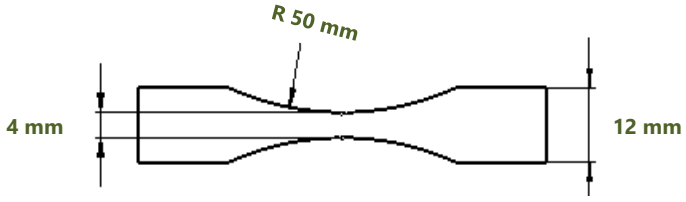

Figure 13: Dimensions of dog-bone test pieces

Each set of test pieces were printed in a slab with 2 mm allowance on the width in the radius at both sides. The radius was then machined to the final dimension and the slab was sectioned into individual test pieces by electro-discharge machining. Test pieces were subsequently polished with SiC grinding paper up to 1000 grit.

Fatigue testing

Fatigue testing was performed on a MTS 810 material testing system at 80Hz in pure tension, R=0.1. Testing was force controlled, and maximum and minimum force and displacement were measured, as well as the amount of cycles.

Standard stairway testing needs about 25 specimens for sufficient accuracy in the results (Schijve 2004). Due to the very limited amount of test pieces per set, this is not an appropriate method and step-wise testing as described by Maxwell and Nicholas (Nicholas 2002) was used instead. Testing is started at a level lower than the expected fatigue limit, and allowed to run to the standard 10^7 cycles. Then the force is increased at constant R=0.1 and this process is repeated until the test piece fails. This process is shown diagrammatically in Figure 14. The fatigue limit at failure is calculated by linear interpolation, based on the amount of cycles at the given value

before failure. This way, barring other problems, every test piece delivers the fatigue limit for that piece and a statistically sound value can be reached.

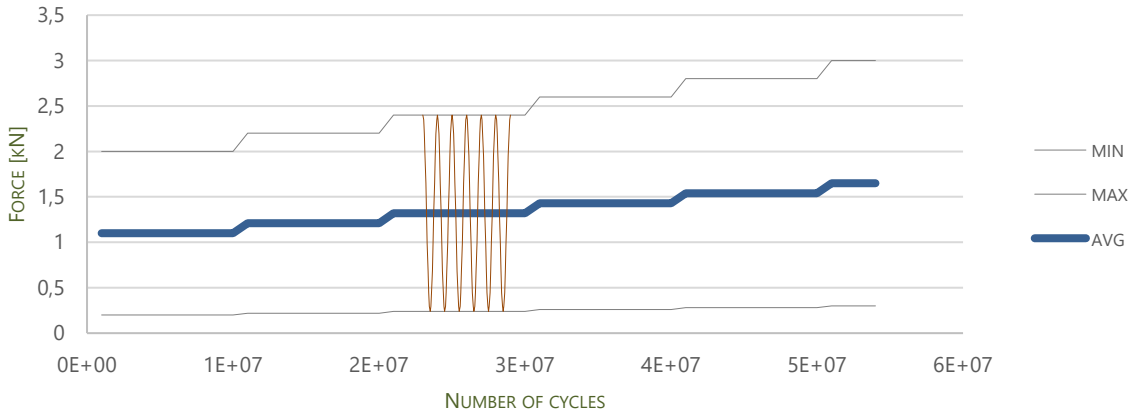

FIGURE 14: EXAMPLE OF CONSTANT R FORCE APPLIED DURING STEP-WISE TESTING.

Results for the printed test pieces will be compared to results from identical test pieces from Ti6Al4V annealed plate.

STATIC TENSILE TESTING

Tensile testing was performed on test pieces identical to the fatigue test pieces. Force, time and elongation was recorded and ultimate tensile strength calculated. Results for the printed test pieces will be compared to results from identical test pieces from Ti6Al4V annealed plate.

FRACTURE TOUGHNESS

Two different forms of fracture toughness tests were done in order to compare the results, namely Charpy V-Notch testing, and compact tension testing to find the stress intensity factor (K_{Ic}).

Charpy V-Notch testing is simple and can be completed in a matter of seconds. Commercially, toughness is typically quantified with Charpy V-notch energy. However this is not an inherent material property, but an indication of the amount of energy absorbed by a set amount of material during fracture, measured in Joule.

Compact tension testing is significantly more involved than Charpy testing, but it delivers a more useful result. Fracture toughness as quantified by the critical plane-strain stress intensity factor (K_{Ic}) is regarded as an inherent material property and is a measure of the resistance of the resistance to crack extension of the material. Testing is time consuming and results can be nullified by a number of factors, as testing needs to be performed under plain-strain conditions, otherwise the results are not relevant.

Both Charpy and fracture toughness results do give an indication of the toughness of the material and both test results should show the same trends.

Charpy V-Notch testing

Standard Charpy tests were performed according to ASTM A370.

Stress intensity factor testing

Fracture toughness testing was done according to ASTM E399 with compact tension test pieces with a width W of 25 mm and a breadth B of 10 mm on a MTS 810 material testing system.

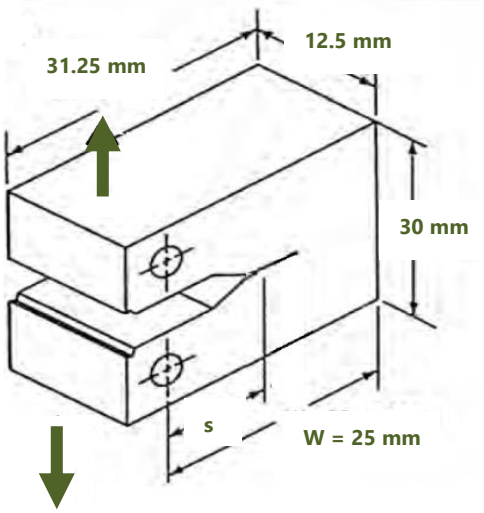

Figure 15: Compact tension test piece dimensions

The pre-fatigue crack formation was displacement controlled at 80Hz and number of cycles and maximum and minimum force and displacement were measured. During final overload testing time, displacement, and force was measured. Subsequently the fracture toughness K_{Ic} was determined according to ASTM E399 as follows:

The force at the 5% secant line (P_Q) was read off the resulting graph, and the conditional stress intensity factor K_Q was be calculated .

$$K_Q = \frac{P_Q}{B\sqrt{W}} \cdot f\left(\frac{a}{W}\right)$$

where B is the specimen breadth, W is the specimen width, a is the crack length and f(a/W) is:

$$\frac{\left(2+\frac{a}{W}\right)\left[0.886+4.64\frac{a}{W}-13.32\left(\frac{a}{W}\right)^2+14.72\left(\frac{a}{W}\right)^3-5.6\left(\frac{a}{W}\right)^4\right]}{\left(1-\frac{a}{W}\right)^{1.5}}$$

There are a number of conditions the tests need to fulfil for the K_Q result to be a valid the K_{Ic} value. These are:

1) The length of the pre-fatigue crack a must fall between 0.45 and 0.55 of the specimen width (see Figure 16).

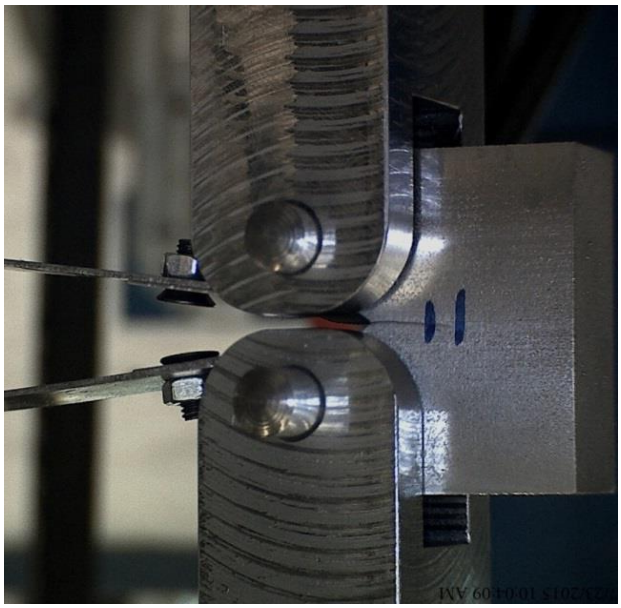

FIGURE 16: COMPACT TENSION TEST SET-UP. VERTICAL LINES SHOW 45% AND 55% SPECIMEN WIDTH.

2) Length of the pre-fatigue crack measured at different points may not vary more than 15% from the average.

3) The size of the fatigue crack on each face of the specimen shall not be less than 0.025 times the width or 1.3 mm, whichever is larger.

4) The fatigue crack and extension shall be parallel to the plane of the starter notch within **10° (**excluding shear lips).

5) Specimen must not fail by brittle cleavage fracture.

6) There shall be no evidence of multiple cracking.

7) The ratio of the maximum applied force over the force at the 5% secant line may not be more than 1.1.

8) The ligament size may not be less than $2.5(K_Q/\sigma_{YS})^2$.

9) The maximum stress intensity factor during pre-fatigue may not be larger than 80% of the calculated K_Q.

10) During the terminal phase of pre-fatigue cracking the stress intensity factor may not be larger than 60% of the calculated K_Q.

11) The loading rate shall be such that the increase in stress-intensity factor is between 0.55m and 2.75 MPa√m/s.

If the test and calculated conditional stress intensity factor fulfils all of these requirements the test can be said to have taken place in plane-strain in a material that does not fail in cleavage nor with appreciable amounts of plasticity. This means that the assumptions underlying the test method and calculation are valid and the resulting value can be accepted as the critical plain strain fracture toughness of the material.

Overall test Matrix

Test pieces are numbered consecutively. There are four fatigue and one identical tensile test pieces, three Charpy impact test pieces, and three stress intensity factor tests in each set. The test pieces are identified in Table 5.

Table 5: Summery and numbering of test pieces

	Transverse	**Longitudinal**
	Fatigue and Tensile	
Stress relieved	FT1 – FT5	FL1 – FL5
HIP	HFT1 – HFT5	HFL1 – HFL5
	Charpy	
Stress relieved	CT1 – CT3	CL1 – CL3
HIP	HCT1 – HCT3	HCL1 – HCL3
	Stress Intensity Factor	
Stress relieved	KT1 – KT3	KL1 – KL3
HIP	HKT1 – HKT3	HKL1 – HKL3

Although an attempt was made to fit as many test pieces as possible on the printing plate, eventually printing was performed in two batches. All transverse Charpy test pieces were in the first batch, as well as the HIP transverse fatigue test pieces, all HIP stress intensity factor test pieces, as well as KL1 and KT1. Remaining test pieces were printed in a second batch.

Additionally fatigue and tensile test pieces were taken from Ti6Al4V plate in order to compare the results. These are PT1 – PT3 in the transverse direction and PL1 -PL3 in the longitudinal direction.

Results

The following shows results for SLM Ti6Al4V transverse and longitudinal test pieces in stress relieved and HIPed condition, as well as conventional Ti6Al4V plate when applicable. The results shown are the microstructure present (shown both in optical microscopy and EBSD), as well as notable features visible in fractography.

Subsequently the results of mechanical testing of tensile strength, hardness and Charpy V-Notch impact testing are given, followed by results of high-cycle fatigue testing and fracture toughness. The influence of the different parameters will be discussed in more detail in later sections.

General

In the following section the results of microstructural examination – both by optical microscopy and EBSD – is presented. Following that are features of the fracture surface as shown in scanning electron microscopy. Lastly the results of hardness testing is presented.

Microstructure - Optical Microscopy

First off for the sake of comparison the structure of the T6Al4V plate used for tensile and fatigue testing is shown in Figure 17 with a magnification of x5, and Figure 18 with a magnification of x50. The micrographs show a globular structure consistent with annealed plate.

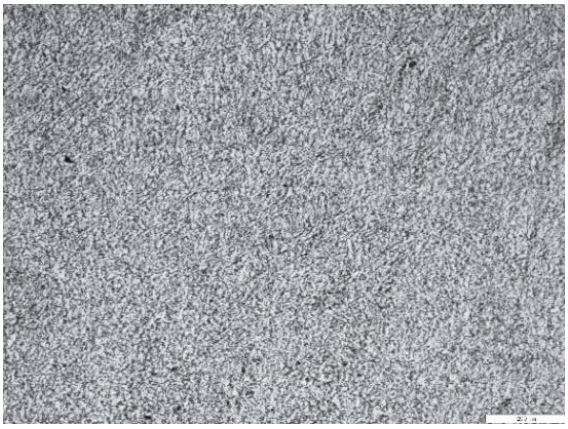

Figure 17: Ti6Al4V plate scale 200 µm in PT2

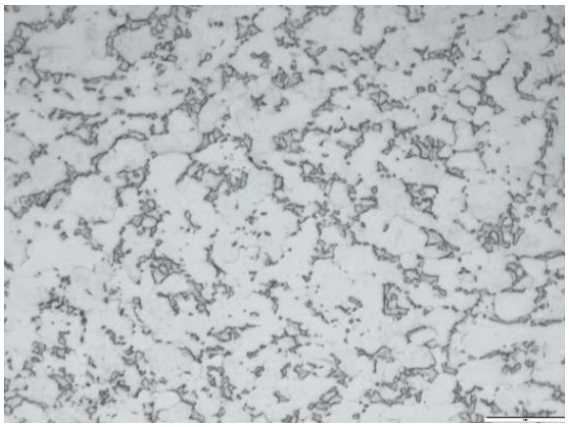

Figure 18: Ti6Al4V plate 20 µm in PT2

The images of the stress relieved structure shown are from test piece KT3, and the images of HIP structure shown is from test piece HKL3. Looking down on the horizontal plane the grain structure is relatively even, with a prior beta grain size of approximately 120 µm diameter, which can be seen at x5 magnification in Figure 19, and x50 in Figure 20. This roughly corresponds with the hatch spacing, as speculated by Thijs, et al. (2010).

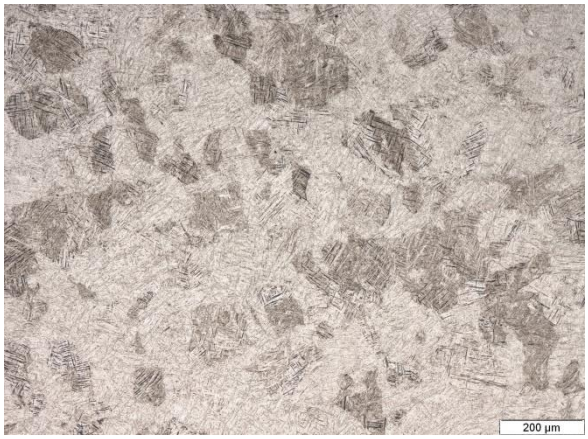

Figure 19: Stress relieved structure (transverse) scale 200 µm in KT3

Figure 20: Stress relieved structure (transverse) scale 50 µm in KT3

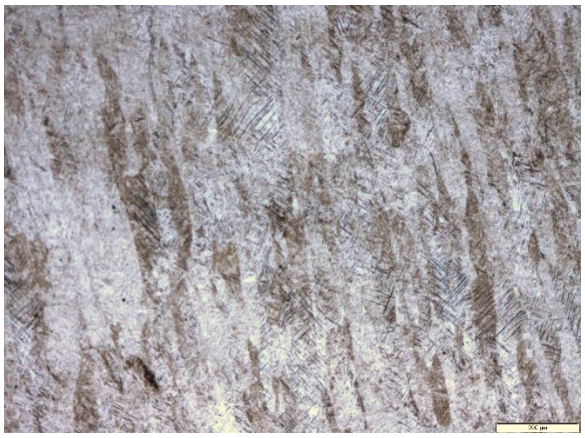

Figure 21: Stress relieved structure (longitudinal) scale 200 µm in KT3

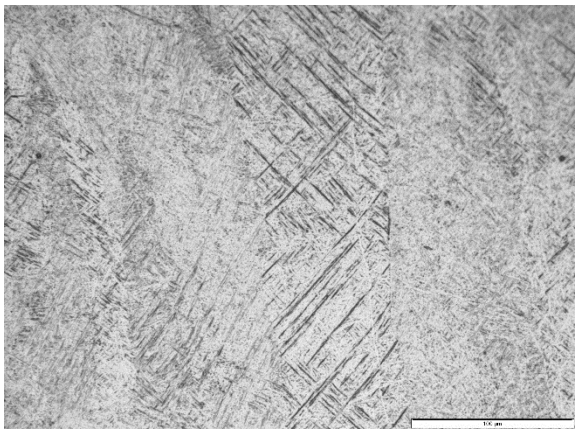

Figure 22: Stress relieved structure (longitudinal) scale 50 µm in KT3

Examining the test pieces from the side shows elongated, slightly angled vertical grains at x5 magnification in Figure 21 and x50 magnification in Figure 22. The acicular structure in the grains show a strong inclination to 45° angles with the horizontal, as can clearly be seen in Figure 22.

The HIP test pieces also show some indication of the same elongated grains at x5 magnification in Figure 23 and x50 magnification in Figure 24, but this feature is less pronounced. The structure is lamellar with some globular and grain boundary α, as can be seen at the arrows in Figure 24.

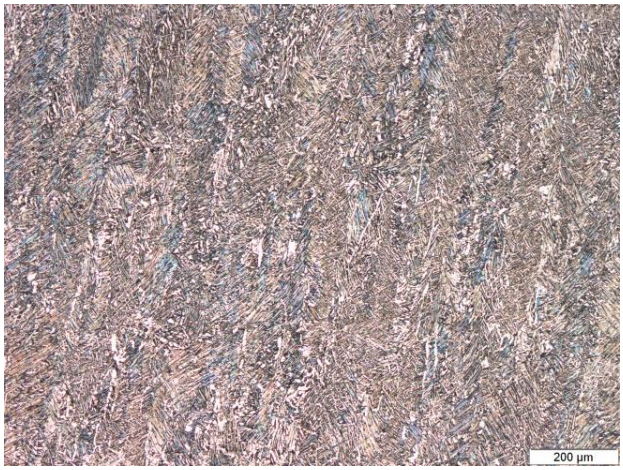

Figure 23: Structure after HIP (longitudinal) scale 200 µm in HFL3

Figure 24: Structure after HIP (longitudinal) scale 50 µm in HFL3

Microstructure – Electron backscatter diffraction

The results of EBSD shows the microstructure at a x200 magnification. The microstructure of a stress relieved sample can be seen in Figure 52. The beta phase is presented in blue. Figure 52 shows the same tendency to 45° angles as can be seen in Figure 22. Figure 53 shows the microstructure of the HIP sample. The amount of beta phase is significantly higher.

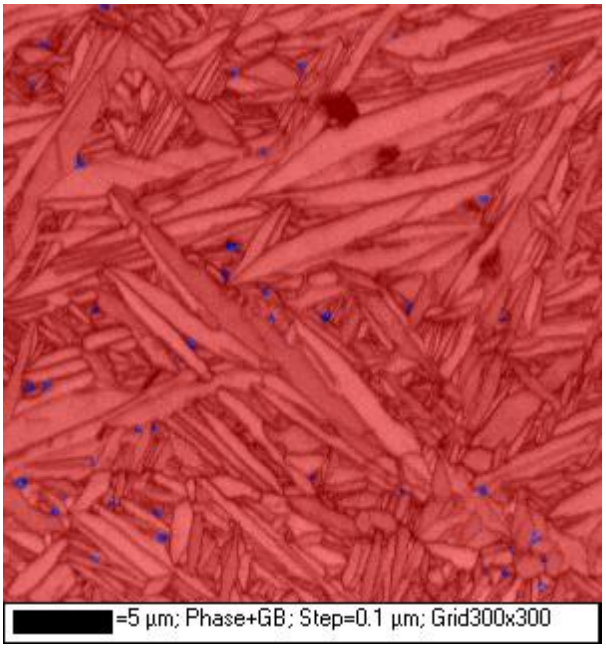

Figure 25: Phase EBSD of stress relieved test piece, beta phase shown in blue – scale 5 µm in FT1

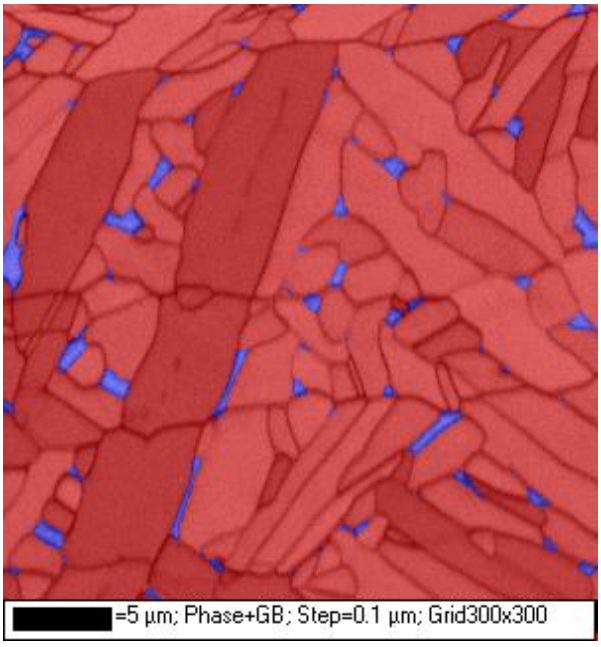

Figure 26: Phase EBSD of HIP test piece, beta phase shown in blue – scale 5 µm in HFT2

Porosity in fracture surfaces

Porosity is a very clear feature in the non-HIP test pieces. Most of these present as rounded when observed in longitudinal fracture surfaces, as seen in Figure 27, and flat gashes in transverse test piece surfaces, as seen in Figure 28, and are over 100 µm in length. This matches the description of lack-of-fusion (LOF) defects given by Sun, Yang and Wang (2012).

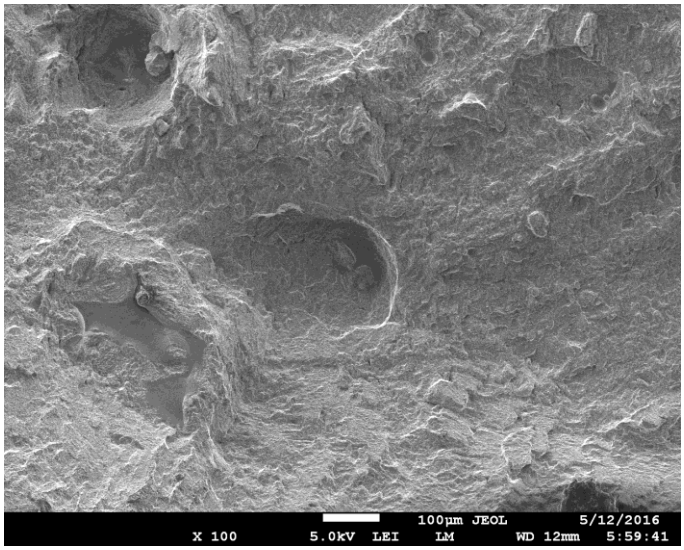

Figure 27: Lack-of-fusion porosity seen from the top in FL3

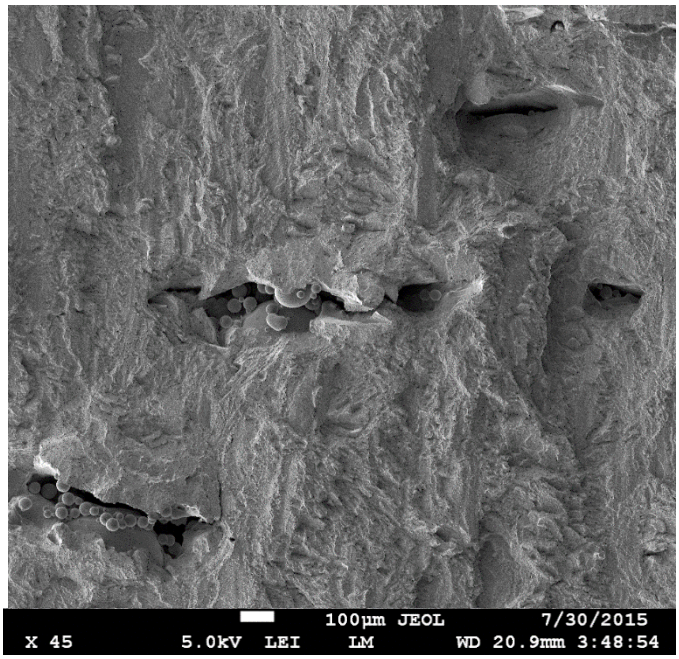

Figure 28: Lack-of-fusion porosity in seen from the side KT1

Apart from LOF defects there are porosities that match the scale of 10 µm – 50 µm given for gas porosity by Vilaro, Colin and Barout (2011). Some of these can be seen in Figure 29.

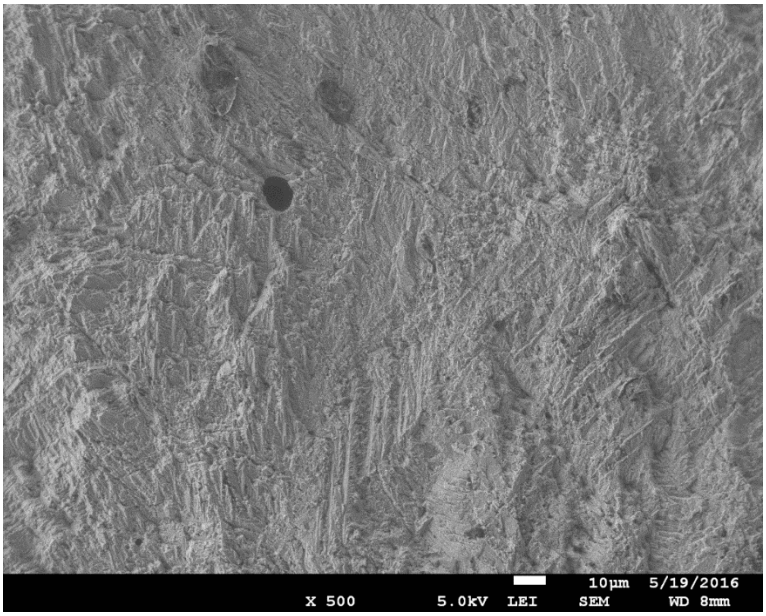

FIGURE 29: GAS POROSITY IN FT1

There are also some larger porosities (Figure 30, note the difference in scale from Figure 29) that may or may not be gas porosity based on the size. These seem to match up both in size and appearance with of porosity seen by Qui, Adkins and Attallah (2013), but these are described as being mostly found on surfaces of transverse test pieces, but here they seem to be equally prevalent on longitudinal fracture surfaces.

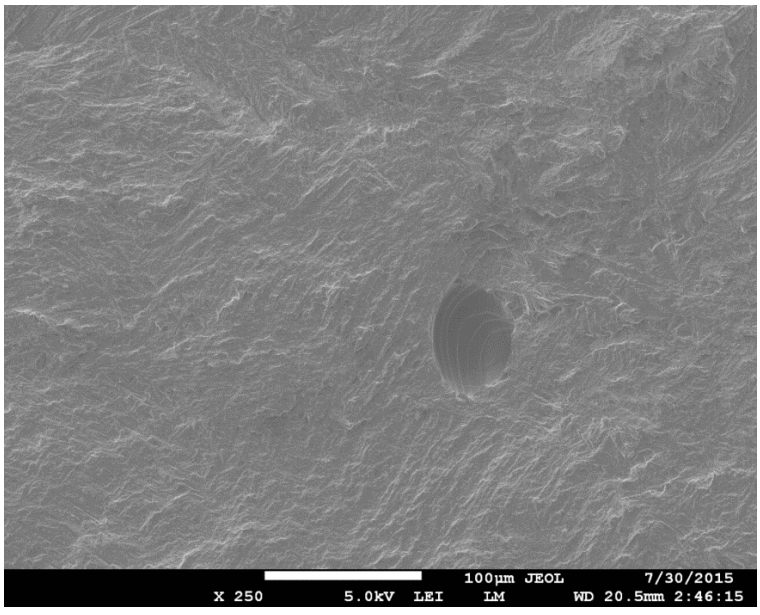

FIGURE 30: POROSITY IN KT2. POROSITIES OF THESE DIMENSIONS ARE ALSO SEEN IN LONGITUDINAL TEST PIECES.

Hardness

All hardness values given in Table 6 are average of at least five measurements. These were measured on test piece KT3 and HKL3

Table 6: Average hardness and standard deviation of stress relieved and HIP test pieces.

	SR		HIP	
	T	L	T	L
Hardness [HV]	377 ± 9	386 ± 9	351 ± 7	350 ± 7

Hardness of the HIP test pieces is lower than stress relieved. Difference between the two direction in HIP test pieces is negligible, but for stress relieved longitudinal is harder on average than transverse.

Two factor ANOVA gives $p<0.05$ for the difference between stress relieved and HIP ($f(1)=69.5$, $p=6x10^{-8}$), but the difference between the two directions could not be statistically confirmed ($f(1)=0.72$, $p=0.4$).

Results of tensile testing

In the following section the results of testing for ultimate tensile strength and fatigue strength is shown.

Ultimate Tensile Strength

A test piece was taken from each set of fatigue test pieces for static tensile testing. The results of these tests are in Table 7.

Table 7: Ultimate Tensile Strength, measuring accuracy of 20MPa

	Plate		SR		HIP	
	T	L	T	L	T	L
UTS [MPa]	1160	1180	1190	1110	1070	1050

The tensile strength of the stress relieved test pieces appear to be somewhat higher than that of the HIP test pieces. However two factor analysis of variance (ANOVA) gives $p>0.05$ for both the difference between stress relieved vs HIP ($f(1)=0.004$, $p=0.96$), and longitudinal vs transverse ($f(1)=0.197$, $p=0.73$), so the difference between the two directions and conditions could not be statistically confirmed based on these results.

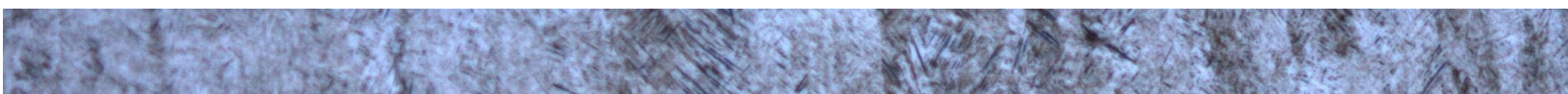

Fatigue Strength

There was a significant amount of spread in the results in Figure 31 for each batch of high-cycle fatigue test pieces, as well as a number of failed tests.

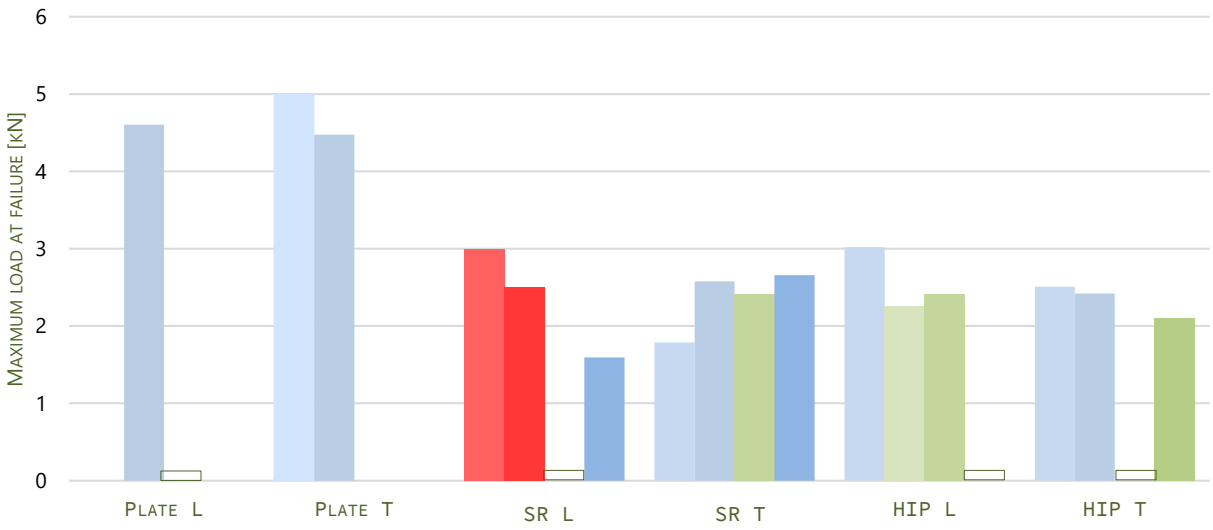

Figure 31: Maximum load at failure of plate, stress relieved, and HIP fatigue test pieces.

Measurements in red indicate failure before high-cycle fatigue was reached. These are by definition higher than a successful test would be. Measurements in green are cases in which the test piece failed at the edge of the test piece holder (presumably due to fretting) instead of in the radius. These values represent a lower limit to the possible high-cycle fatigue strength, since presumably the sample would have failed at a later point of no fretting was present. Null value results were tests in which no result was delivered due to effects like test piece holder failure or improper parameters of the testing machine. The measuring error is 0.04 kN.

The data from test pieces that failed at the edge of the test piece holder were not used for further processing to reach the calculated fatigue limit as the goal is to find a fatigue limit for the material proper, as the HCF of Ti6Al4V is known to be sensitive to surface effects (ASM International 1996) and the intension is to measure the fatigue strength of the material itself and not the influence of surface effects. Table 8 gives the average R=0.1 fatigue limit for every set, as well as the standard error per set, with the assumption that the standard deviation is the same in both directions for a given condition.

Table 8: Average fatigue limit (error is the larger of the measuring error and the standard error)

	Plate		SR		HIP	
Alternating stress R=0.1	**T**	**L**	**T**	**L**	**T**	**L**
Fatigue [MPa]	268 ± 6	263 ± 4	126 ± 17	83 ± 30	174 ± 7	176 ± 5

The HIP test pieces show a statistically relevant higher value than the stress relieved (two factor ANOVA $f(1)=32.5$, $p=0.0005$). Although it seems that stress relieved transverse has a higher fatigue limit than longitudinal, there is too much scatter within the results to come to any firm conclusion about the difference between transverse and longitudinal tests ($f(1)=2.9$, $p=0.13$).

Fractography

The fracture surfaces of the SLM test pieces are shown in Figure 34 to Figure 39, and the test piece from plate in Figure 32 and Figure 33. Some of the SLM test pieces did not show any clear features on a macro scale on the fracture surface, but most can successfully be compared with plate fracture surface. The features are not as clear in the images of SLM fracture surfaces and are shown with a green line for clarity.

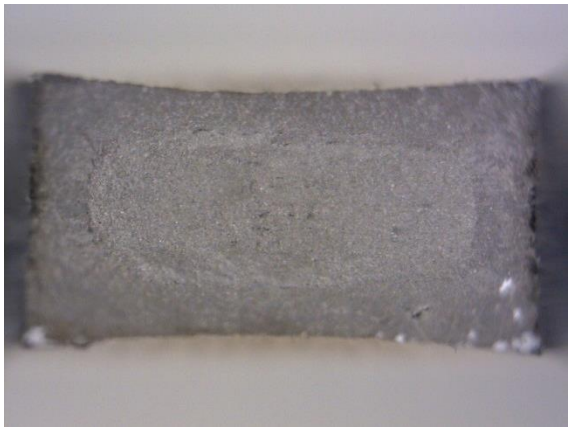

Figure 32: Tensile testing of standard Ti6Al4V plate in PL1

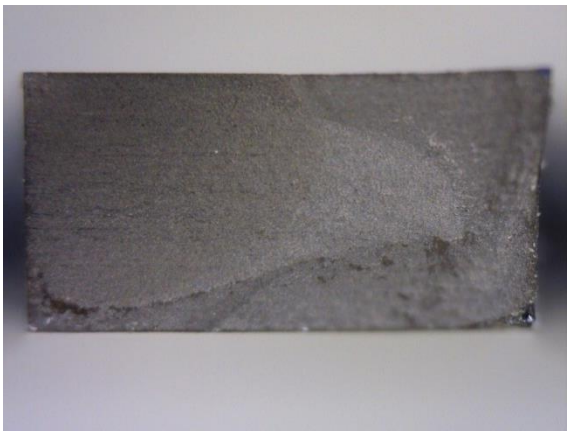

Figure 33: Fatigue testing of standard Ti6Al4V plate in PL2

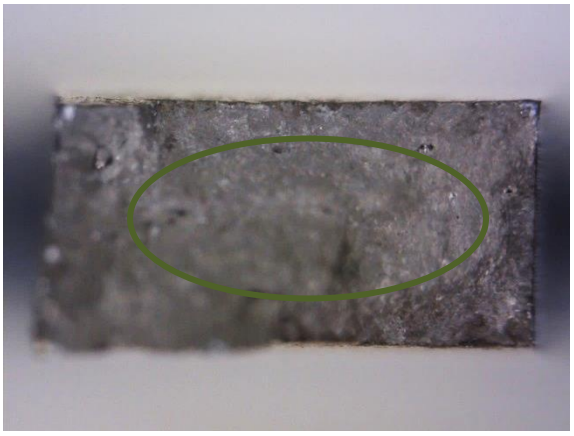

Figure 34: Tensile testing stress relieved test piece (FT1) Macro same features as Figure 32.

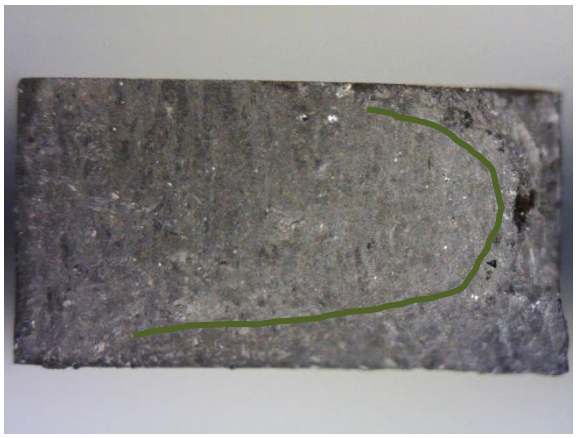

Figure 35: Fatigue testing stress relieved test piece (FT5) Macro same features as Figure 33.

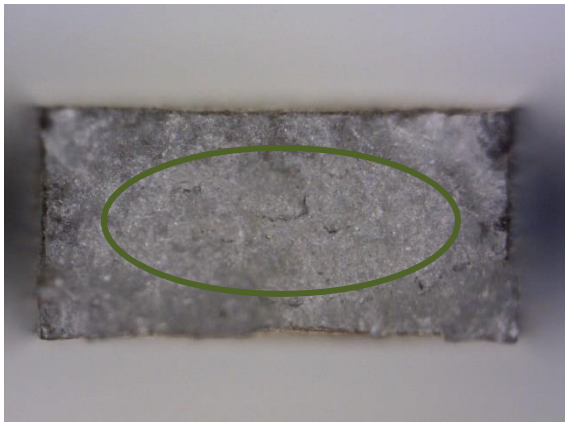

Figure 36: Tensile testing HIP test piece (HFL1) Macro same features as Figure 32.

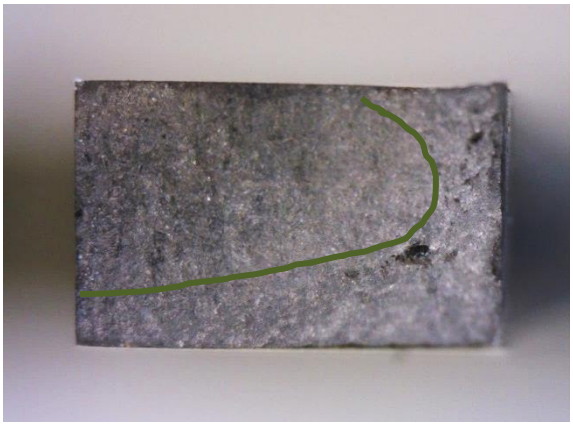

Figure 37: Fatigue testing HIP test piece (HFT3) Macro same features as Figure 33.

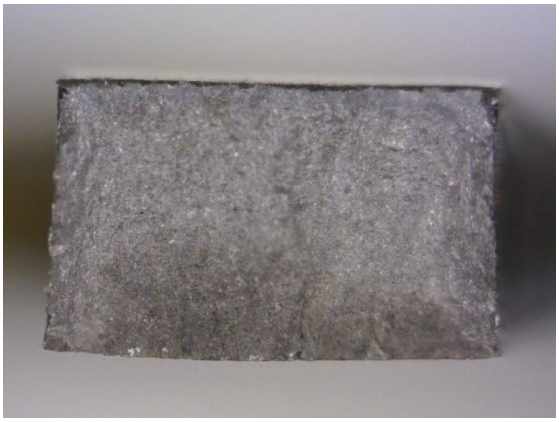

Figure 38: Fracture surface very uneven - no fatigue and overload can be distinguished. (HFT4)

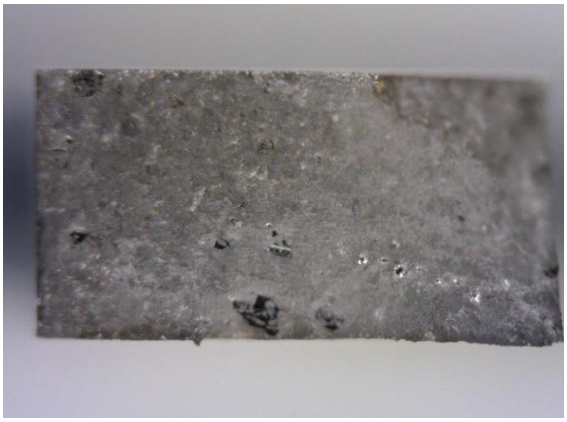

Figure 39: SR Longitudinal test piece with defects (FL3). Macro same features as Figure 33

The fracture surface of test pieces for static tensile testing show the standard cup and cone fracture, most readily visible in Figure 32, although in some cases the shear lip of the plate test pieces tended to tilt 45˚, becoming closer to a ductile shear tear. Although the SLM test pieces do not show any macro scale signs of ductile shear, the fracture surfaces of the static tensile tests tended to that same 45˚ angle.

In most cases the SLM fatigue test pieces show the same features as the plate – must of the surface is flat fatigue fracture appearing to start near the edge or corner of the test piece (all the images of fatigue test pieces oriented so origin is in the top left corner), with final ductile overload. Defects were often visible, and a few test pieces (like Figure 38) had very rough fracture surfaces were none of the expected macro features could be seen.

When viewed in the SEM a couple of trends become visible. Striation can be seen in the fatigue test pieces. The coarseness of the striations increases notably with distance from the apparent initiation

point (compare Figure 40 and Figure 41). This would be because testing was force-controlled, meaning that as the crack progressed and the effective stress per cycle was higher.

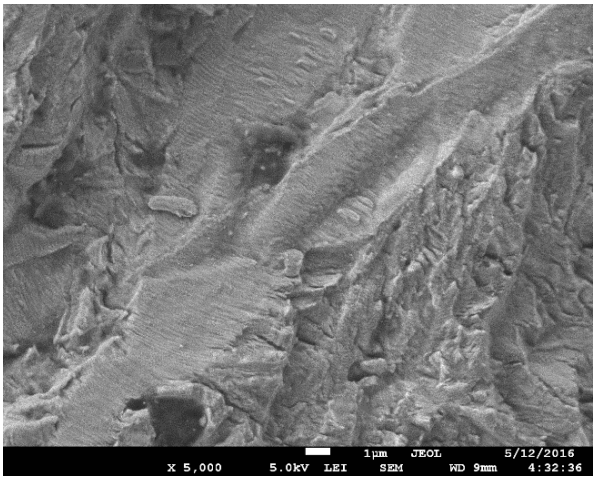

FIGURE 40: FINE STRIATIONS IN FL3 (FROM BOTTOM LEFT TO TOP RIGHT) NEAR INITIATION POINT.

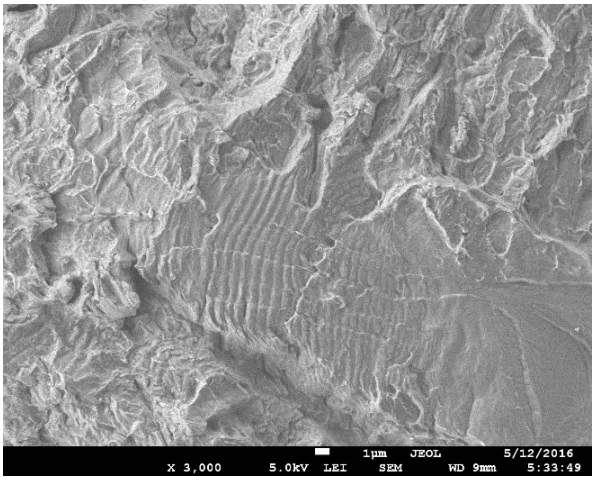

FIGURE 41: COARSE STRIATIONS IN FL3 (FROM BOTTOM RIGHT TO TOP LEFT) FAR FROM INITIATION POINT.

Occasional signs of secondary cracking were visible in all test pieces, see Figure 42 for a clear example.

Although some sections show clear fatigue striations and some sections show clear dimpling in overload, no clear transition between fatigue and overload could be seen in SEM fractography, in contrast to the naked eye (for example in Figure 35) where the transition between fatigue and overload is visible.

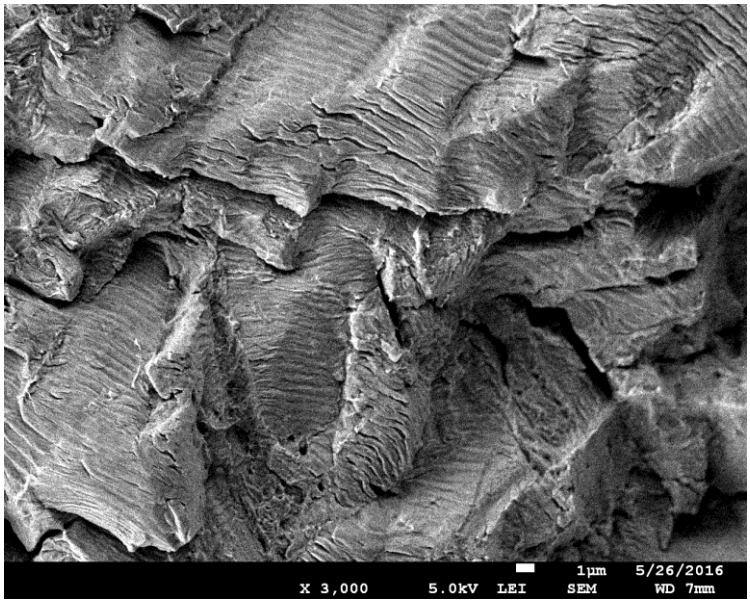

FIGURE 42: STRIATIONS AND SECONDARY CRACKING IN HIP TEST PIECE (HFT2)

Results of Fracture Toughness Testing

In the following section the results of Charpy V-Notch and fracture toughness testing is presented.

Charpy V-Notch

The results of standard Charpy V-Notch impact tests results can be seen in Table 9.

Table 9: Charpy impact values – average of three values each

	SR		HIP	
	T	L	T	L
Charpy V-Notch Energy [J]	10 ± 1	16 ± 1	21 ± 1	22 ± 1

There is a notable difference between the build-directions and between stress relieved and HIP. Longitudinal test pieces are tougher than transverse, and HIP test pieces are tougher still Two factor analysis of variance confirms both these inferences with difference between stress relieved and HIP $f(1)=185.8$, $p=8x10^{-7}$, and longitudinal and transverse $f(1)=31.5$, $p=0.0005$.

Stress Intensity Factor

The conditional fracture toughness K_Q is calculated from the test piece dimensions, pre-fatigue crack length and force at the 5% secant line. The crack length and maximum force can be seen in Figure 43.

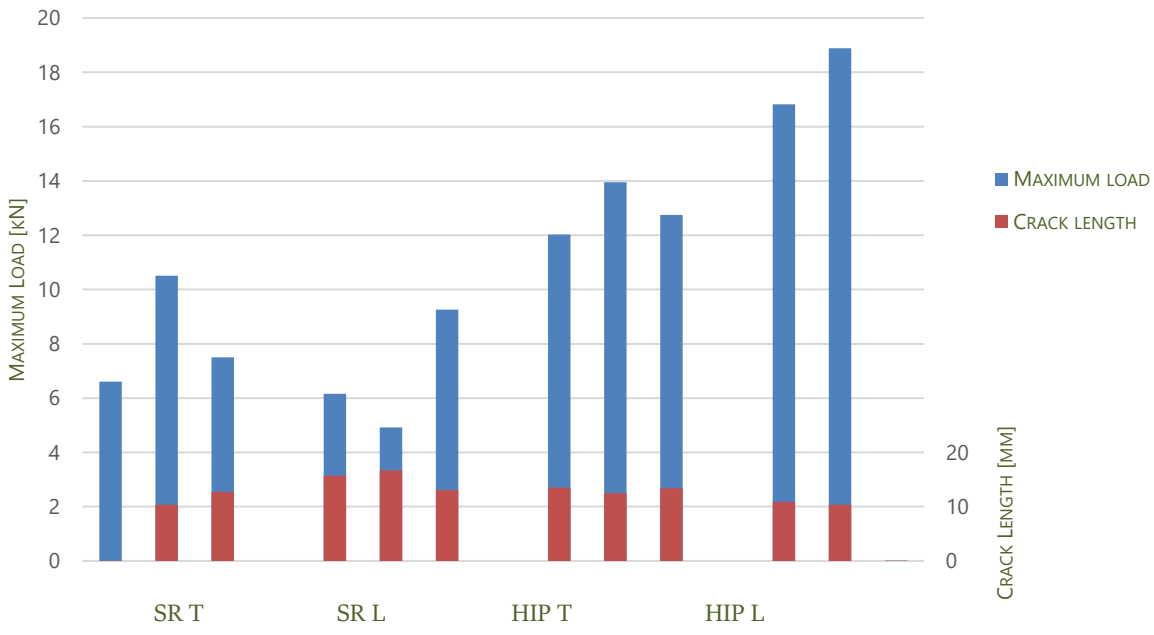

Figure 43: Maximum load and initial crack length of fracture toughness test pieces

The two null value tests are a case in which the pre-fatigue crack length was not measurable, and one case of test piece holder slipping in the rig.

There proves to no be much spread in the conditional fracture toughness within each batch. Checking the validity of the results and discarding as necessary gives the average values as given in Table 10.

TABLE 10: FRACTURE TOUGHNESS AND STANDARD DEVIATION OF STRESS RELIEVED AND HIP TEST PIECES.

	SR		HIP	
	T	L	T	L
Fracture Toughness [MPa√m]	44.8 ± 0.2	48.5 ± 0.4	74.0 ± 0.3	73.2 ± 0.3

The HIP values are markedly higher than the stress relieved, which is statistically confirmed with two-factor ANOVA ($f(1)=143$, $p=0.05$). Average longitudinal value is higher than transverse but the difference between longitudinal and transverse cannot be statistically confirmed.

FRACTOGRAPHY

Figure 44 to Figure 47 contains images of fracture surfaces of compact tension test pieces. In all four images can be seen, from left to right, notch, pre-fatigue crack growth, and then overload fracture.

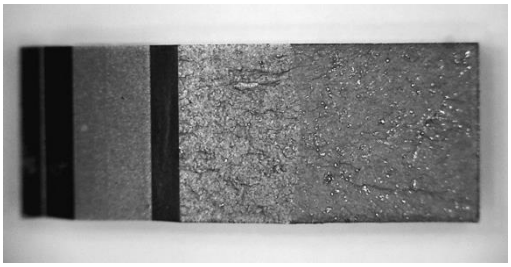

FIGURE 44: LONGITUDINAL CT TEST PIECE (KL3), STRESS RELIEVED

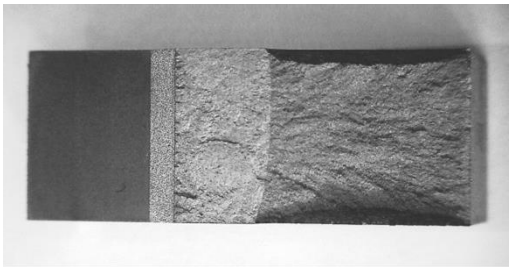

FIGURE 45: LONGITUDINAL CT TEST PIECE (HKL1), HIP

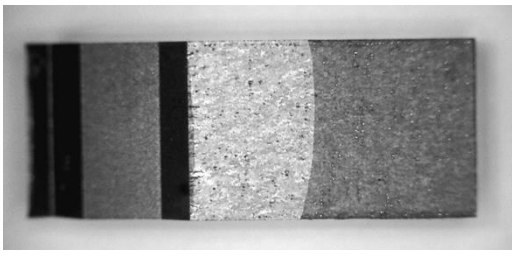

FIGURE 46: TRANSVERSE CT TEST PIECE (KT3), STRESS RELIEVED

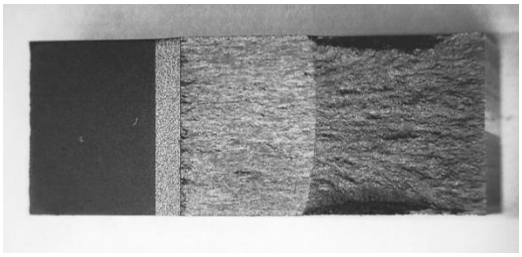

FIGURE 47: TRANSVERSE CT TEST PIECE (HKT3), HIP

The fracture surface stress relieved test pieces the fracture surface is predominantly flat. On the longitudinal test pieces this is quite rough, in both the pre-fatigued and overload sections. The fracture surface on the transverse test pieces is more even, and in the case of the stress relieved test pieces the pre-fatigue section is almost reflectively smooth.

The HIP surfaces are not completely flat but shear lips slant 45˚ in the overload section. The fracture surface is still smoother in the case of the transverse test pieces than the longitudinal test pieces, but the difference is less pronounced.

The transition between pre-fatigue and overload is clearly visible, not just in macro fractography, but also in the SEM, as can be seen in Figure 48.

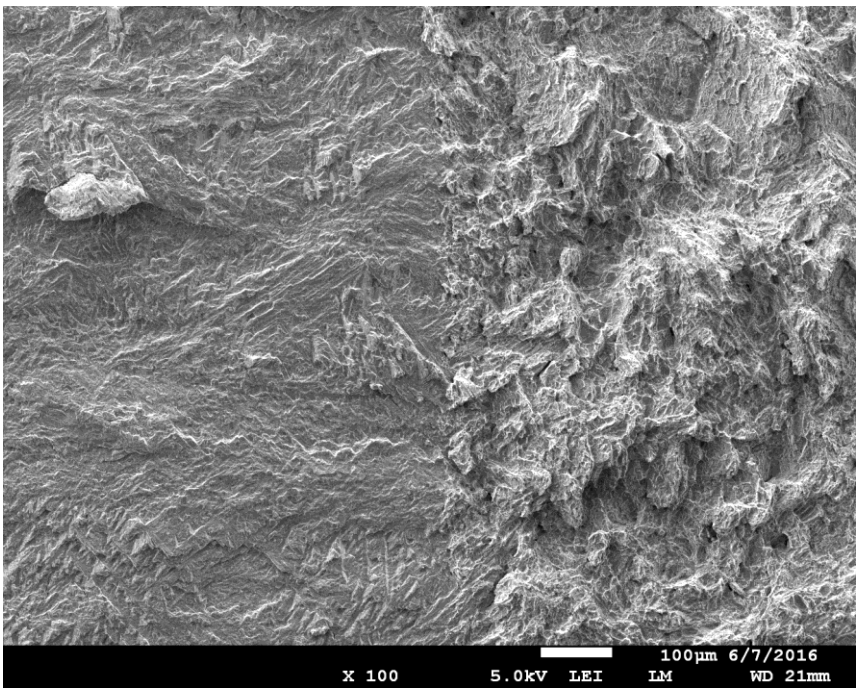

FIGURE 48: TRANSITION BETWEEN PRE-FATIGUE AND OVERLOAD, LEFT TO RIGHT. (HKT3)

This is more difficult to find in the stress relieved longitudinal test pieces, but is easily seen for the others up to higher magnifications.

Just like in the fatigue test pieces, striations can be seen in the sections of the surface fractured by fatigue, see Figure 49. The spacing varies somewhat from position to position, although not to the degree of the HCF test pieces as seen previously. This is probably because the cyclic load was displacement controlled, meaning the effective force did not change meaningfully as the crack progressed.

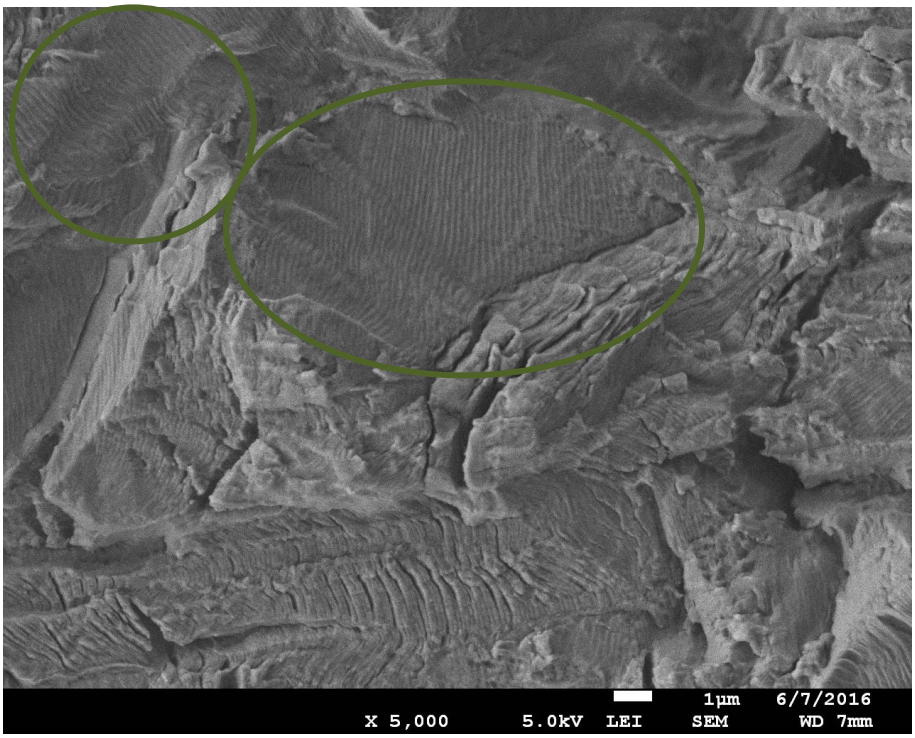

FIGURE 49: FINE FATIGUE STRIATION (LCF) IN PRE-FATIGUE REGION OF THE HIP CT TEST PIECES (HKL1).

Discussion

There are a couple of general trends that seem to follow from the experimental results. Longitudinal test pieces perform better than transverse in terms of toughness. It appears that the trend for high-cycle fatigue is the other way around, with transverse performing better, but that is not a statistically sound result. HIP test pieces perform better in both fatigue and toughness and the anisotropy in the results becomes negligible. There is remarkably little spread in the toughness values, and significant spread in fatigue results, but both become more consistent after HIP.

While being able to recognise trends is helpful it does not give much information in terms of knowing what the mechanical behaviour of a printed part will be. Consider that the effects of the specific SLM machine, printing parameters, post-processing treatment and factors inherent to the shape of the part, like solidification and temperature profile due to conduction all have different influences. For this reason is it necessary to know not just the values of test pieces for a given print, but the factors that influence these values, in order to form an expectation of the behaviour of a finished part. The most notable factor that needs considering is the structure of the material.

Macro- and Microstructure

The most notable feature of the structure are the elongated grains (see Figure 50) with a diameter of about 120 µm, slightly angled in the direction of laser movement (Thijs, et al. 2010). In order to properly discuss the properties found during testing a closer look at the microstructure and other features is necessary, as the fatigue limit and toughness respond quite differently to different factors in the structure.

Figure 50: Elongated grains in stress relieved structure (longitudinal) x200 in test piece KT3

The differences in orientation and heat treatment are quite visible in the structure of the material, and it is to be expected that this will subsequently affect the properties as well. In the SLM process Ti6Al4V forms in long, columnar grains of the BCC β phase. Cubic structures like the high temperature β phase in Ti6Al4V grow the fastest in the <100> direction, giving a strong <100> texture in the direction of cooling (roughly vertical) in the elongated grains (Brandt, et al. 2013). During cooling β phase transforms to fine acicular (lathe) martensite (α' and α''). Generally the basal plane, which is the most densely packed direction of the α' hexagonal structure, grows along the most densely packed direction of the BCC structure {110} (He, et al. 2018), forming the Burger's orientation relationship of $\langle 1\,1\,1\rangle\beta /\!/ \langle 1\,1\,2\,0\rangle\alpha'$ (Yang, Yu and Yin, et al. 2016). What this means in practice is that martensite needles form at 45° angles to the prior β grain, and consequently the α that forms after heat treatment has the same orientation as can be clearly seen in Figure 50 and Figure 51. While this is a very directional structure, due to the number possible α' variants within the β structure this only results in a weak texture (Simonelli, Tsea and Tuck 2014). Also it seems that printing with higher energy density triggers the formation of α' along less closely packed planes, further reducing the texture (Yang, Yu en Wang, et al. 2017).

Heat treatment transforms martensite into α with some β phase, leaving some residual martensite depending on the temperature of heat treatment and the cooling rate. During heat treatment at temperatures over roughly 800C° the structure starts turning from acicular to lamellar, with lamellas thickening and formation of lamellar α colonies at higher temperatures (for example in the blue circles in Figure 51) (Zhao, et al. 2016).

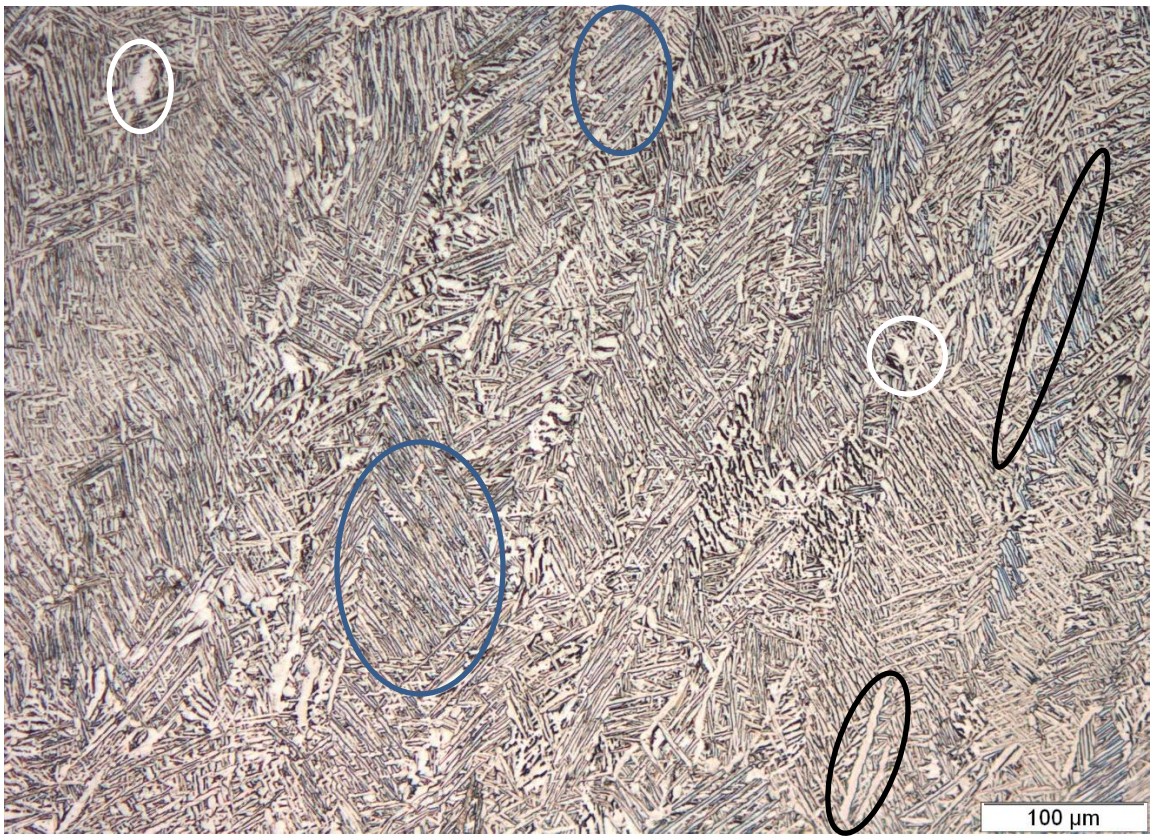

Figure 51: HIP structure with alpha colonies (in blue), globular alpha (in white) and some grain boundary alpha in (black) in test piece HFL3.

Simultaneously with the formation of lamellar α colonies, some grain boundary α (in black circles in Figure 51) can also be formed. At even higher temperatures (although still below the β-transus) some globular α is also formed, as can be seen in the white circles in Figure 51. While there are many changes with heat treatment under the transus temperature, not much coarsening of the columnar prior beta grain structure occurs unless the β transus temperature is reached (Brooks 1990).

There are a couple of observations that can be made of the microstructure by means of EBSD analysis. Martensite is typically reported to have lathe thickness of <1 µm. This matches well with the result of acicular α thickness of 0.5 – 1.0 µm in Figure 52. The lamella thickness of 3 µm – 5 µm in Figure 53 also compares well to the compilation of lamella thicknesses of 2 µm – 6 µm after treatment between 900 °C and 1000 °C reported by Zhang, et al (2018). Zhang, et al (2018) also confirm the higher β content after heat treatment at higher temperature that can be seen when comparing Figure 52 and Figure 53.

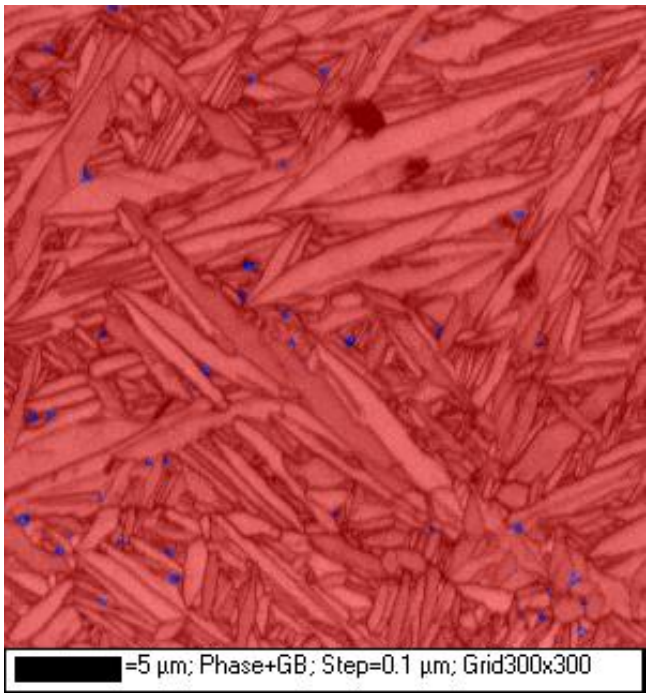

Figure 52: Phase EBSD of stress relieved test piece, beta phase shown in blue in FT1

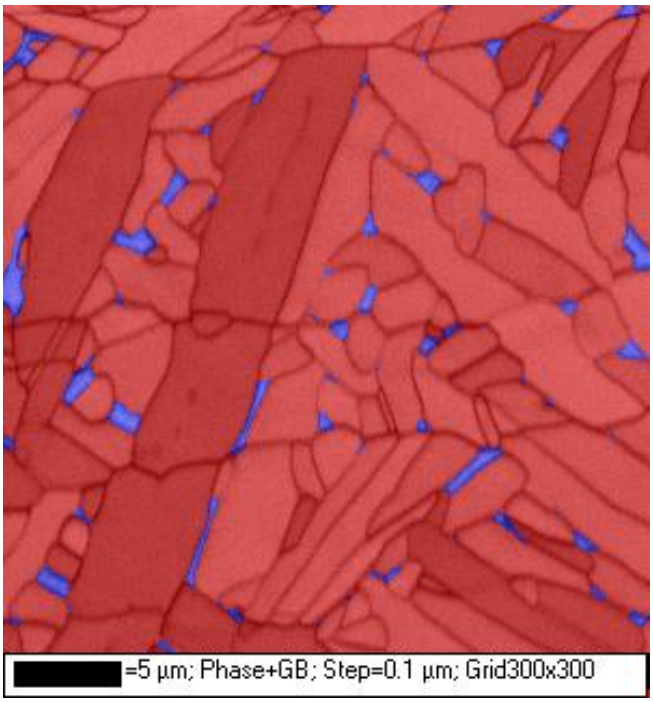

Figure 53: Phase EBSD of HIP test piece, beta phase shown in blue in FT2

Of course the microstructure influences some of the features seen on the fracture surface of various test pieces. Parallel lines can be observed on flat sections of fracture surfaces, as can be seen in Figure 54. These are too coarse to be fatigue striations and tend to have approximately the same spacing irrespective of how far they are from the point of crack ignition. These lines seem to be most readily visible on the fracture surface of stress relieved transverse test pieces. They are only rarely visible on some on the other sets of samples as these tend to have less continuous flat sections.

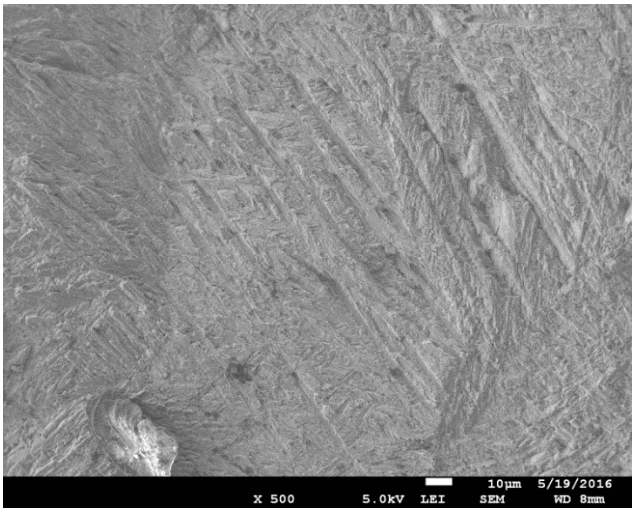

Figure 54: Parallel lines on FT2 fracture surface. Spacing remains similar over all test pieces

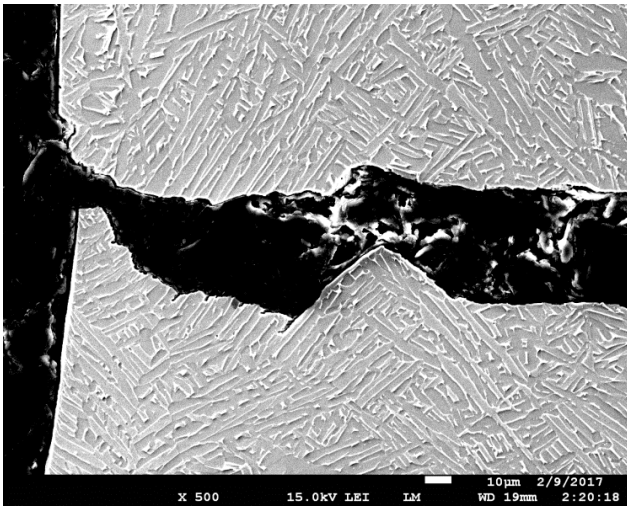

Figure 55: Spacing of structure visible on side view of fatigue crack of HFL2

It is likely that these are the result of some feature of the underlying structure, and the lines spacing seems to match of with angled α lathe spacing – see Figure 54 compared to Figure 55. However this is conjecture and the cause of the parallel lines cannot said to be conclusively stated.

Another feature in fractography that is influenced by the structure are dimples. In all test pieces – Charpy, fatigue, static tensile and fracture toughness, the overload fracture surface shows dimples due to coalescence of microvoids typical to ductile fracture in metals. An example of these can be seen in Figure 56.

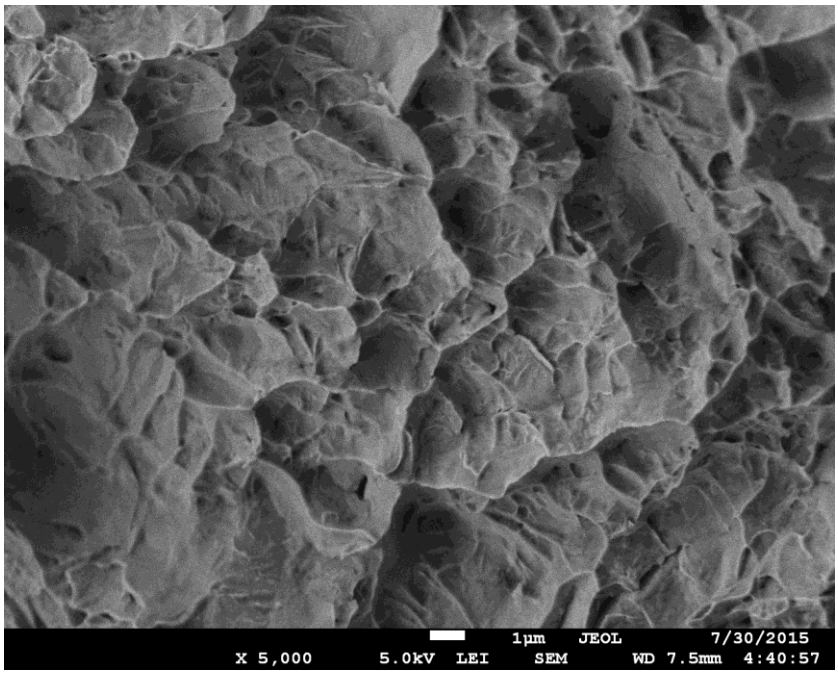

Figure 56: Dimples in overload fracture (KT1)

The size of dimples are influenced by ductility of the material and grains size, with both having a positive effect on dimple size (Joshi 2006). Yang, Yu and Wand, et al. (2017) report seeing this in SLM Ti6Al4V (i.e. coarser, more ductile HIP having larger dimples), but this could not be confirmed to be the case here.

There are aligned indications in the fracture cross-sections, specifically in at the fatigue test pieces' overload sections crack parallel to the shear lip. This can be seen indicated in green for SR and HIP, longitudinal and transverse in Figure 57 to Figure 60. The locations suggest these aligned indications may well be microvoids that have not had the chance to coalesce into dimples and gross fracture.

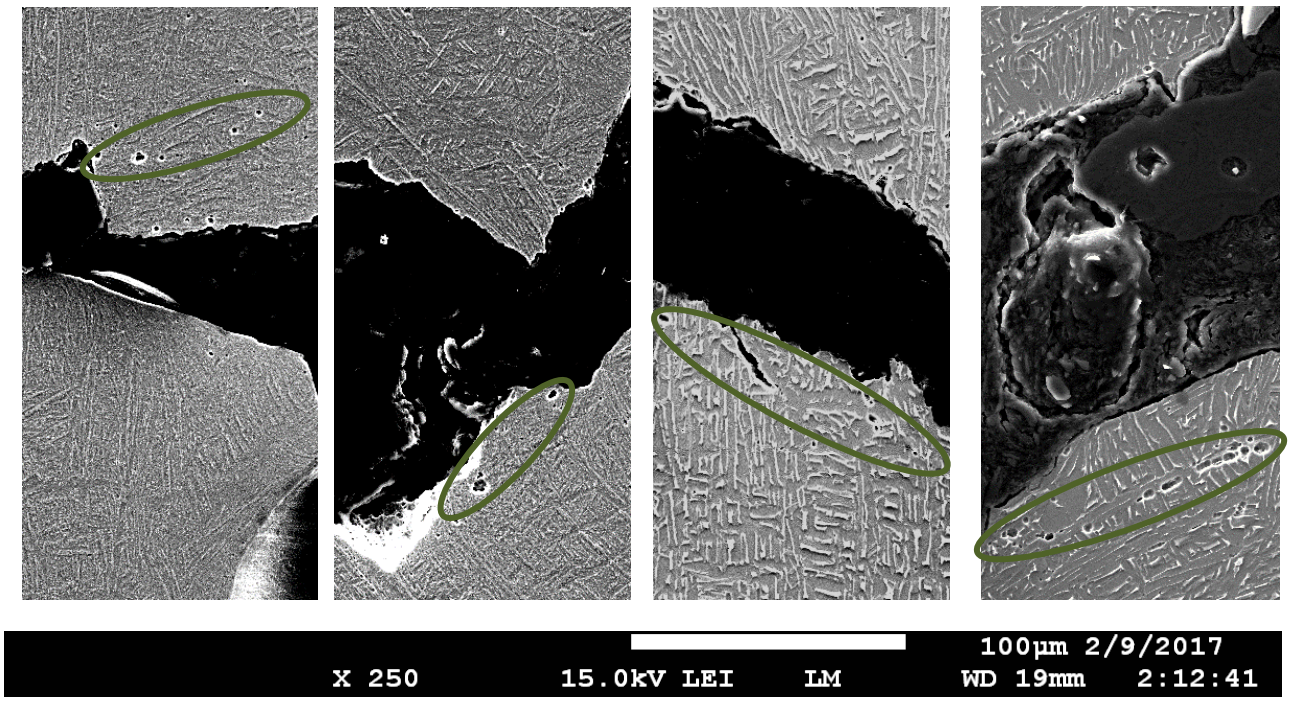

Figure 57: End of overload fracture of transverse SR test piece FT2

Figure 58: End of overload fracture of longitudinal SR test piece FL5

Figure 59: End of overload fracture of transverse HIP test piece HFT3

Figure 60: End of overload fracture of longitudinal HIP test piece HFL2

It is known that dimples initiate easily at the α/β interface at the prior beta grain boundary (Zhao, et al. 2016) because deformation spreads easily in a continuous α cluster but is hindered by the boundary, causing stress concentration and making it easier for voids to nucleate (Yan, et al. 2018). In the case of transverse test pieces the grain boundaries line up with the direction of crack propagation, making it easier for multiple dimples to form and the fracture to grow, lowering ductility and toughness. In longitudinal test pieces there are only a few points of α/β boundary exposed so theoretically fewer dimples can nucleate and must grow to larger size for the fracture to be able to propagate (Yan, et al. 2018). While in practice the lower ductility and toughness and flatter fracture surface of the transverse test pieces is borne out in these and other results, there were no easily notable differences in dimple size, nor do the microvoids (if that is what they are) seem to form specifically at α/β grain boundaries in Figure 57 to Figure 60.

Now that we have a some more insight into the structure and features that can be observed we can discuss how this and other factors may influence the mechanical properties.

Trends in Toughness

There are few fracture toughness values available from literature for comparison. However the test results that are available are remarkable consistent with the results found here. There are two notable trends in the results of both the Charpy V-notch test and compact tension testing. The stress relieved longitudinal test pieces show a significantly higher toughness value than the transverse test pieces. The second notable trend is that in both sets of tests the toughness after HIP was notably higher, with little to no anisotropy remaining. These test pieces also show the beginning of a tendency to 45° shear lip formation which the stress relieved pieces did not have, indicating greater plasticity.

There are a number of factors that can influence toughness and anisotropy, e.g. residual stress, defects and microstructure. These will be discussed in more detail in the following sections.

Grain size

There is some indication of a positive correlation between grain size and impact toughness for most materials (Li and Li 1988). In the case of Ti6Al4V it is known that high density grain boundaries of fine structures like martensite slows the propagation of short cracks, but has the opposite effect once the crack is longer than approximately 1 mm (Van Hooreweder, et al. 2012). Toughness is primarily an issue of crack extension, not initiation (Prasad Rao, Angamuthu and Bala Srinivasan 2008) and as such is more affected by long crack behaviour. This would suggest that the correlation between grain size and toughness holds for Ti6Al4V.

For acicular structures like the martensitic and lamellar microstructure specifically, the width of α plates or lathes are significant in determining the toughness, although other parameters of the structure, like the prior β grain size and the α volume fraction also contribute (Cvijovic-Alagic, et al. 2014). Since lamella thickness is mainly a function of temperature of heat treatment (Zhang, et al. 2018) this would lead to the expectation that the HIPed pieces (treated at 920°C) would have a higher toughness than stress relieved (treated at 735°C), which is borne out in this and other studies.

Unfortunately this does not explain why there is difference in results for transverse and longitudinal, but little anisotropy for HIP.

Residuals stress

The strongest factor for anisotropy, at least for as-built pieces, is residual stress. It could be that the stress relief heat treatment was not sufficient to completely remove these stresses, while the higher temperature HIP was. Residual stresses are usually reported as being primarily in the build direction and as such would reduce the toughness of longitudinal tests compared to transverse. However according to Cain, et al. (2015) the residual stress in the build direction is tensile at the surface but compressive in the bulk of the material. This complicates matters. While tensile stress will reduce mechanical properties across the board, compressive stress will tend to crack closure, reducing crack growth and increasing toughness. And toughness is primarily a bulk, not surface, property, so it will seem that the positive effect of compressive stress will dominate, but it remains to be seen what the effects are in practice.

Wu, Lai and Chen (2016) performed Charpy tests on as-built Ti6Al4V and found that the results for longitudinal tests (5 J) were far lower than for transverse (10 J). This seems to show that the net effect of residual stress on longitudinal toughness is negative. Additionally this factor does not continue into stress relieved pieces. In this study, as well as Kruth, et al. (n.d.) and Yasa, et al. (2010), a transverse impact toughness of 10J was found for stress relieved pieces (the same as transverse impact toughness for as-built found by Wu, Lai and Chen (2016). The notable difference was that for stress relieved test pieces in all cases the longitudinal values were higher than transverse, as opposed to the lower value for as-built longitudinal of Wu, Lai and Chen (2016). In fact heat treatment at 730C for 2 hours has been shown to be sufficient to completely remove residual stress (Vilaro, Colin and Bartout 2011) and treating at higher temperature gives no improvement in this respect (Leuders, Thöne, et al. 2013). This makes it clear that residual stress is not the cause of the anisotropy in stress relieved pieces, nor is the absence thereof the reason why there is no anisotropy for HIPed pieces.

Porosity

Another factor that could be causing this difference in anisotropy is porosity. The presence of defects and porosities in the stress relieved test pieces could conceivably cause an anisotropy, and the absence of these porosities due to HIP would explain the lack of anisotropy in HIPed pieces. It is an often referenced to conclusion by Yasa, et al. (2010) that porosities are the cause of anisotropy in the toughness values of SLM Ti6Al4V. This conclusion is tenuous, however, and is presented without supporting data or arguments, apart from that both porosity and anisotropy was noted and therefor the one most have caused the other.

Due to the difference in solubility in liquid compared to solid Ti6Al4V, trapped gas can cause porosities of 10-50µm throughout the material (Vilaro, Colin and Bartout 2011). However these do not seem to vary with the different orientations and are randomly distributed (Simonelli, Tsea and Tuck 2014) and so cannot be said to cause anisotropy. Problems with printing parameters can cause lack-of-fusion (LOF) defects. These are very common in SLM parts. They are usually 100-150µm and elliptical when seen from the build direction, linear in the build-plate direction (Wu and Lai 2016). This could clearly cause anisotropy, but LOF defects are aligned with the crack growth direction in longitudinal test pieces. As such the directionality does not explain the higher values of the longitudinal samples as they would cause the opposite. So while the reduction in porosity in the HIP samples might contribute to the higher toughness values in general, porosity as such does not explain the anisotropy observed in the stress relieved test pieces.

Mesostructure

The directionality of the prior beta grains are a plausible explanation for the anisotropy of the stress relieved test pieces. The elongated prior grain boundaries can be seen as points of crack arrest or deflection, causing a more torturous crack path. This is known to increase toughness (Prasad Rao, Angamuthu and Bala Srinivasan 2008). The fracture path of longitudinal test pieces cross more prior grain boundaries and consequently has higher toughness.

We have previously mentioned the ease of dimple formation at prior beta grain boundaries which are flat in the transverse direction, decreasing ductility and toughness. Further indication of a more torturous crack path for the longitudinal test pieces can be seen when comparing the fracture surface of the stress relieved test pieces, in which the longitudinal (Figure 61) is substantially rougher than transverse (Figure 62).

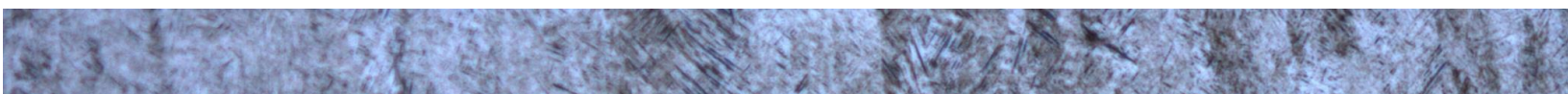

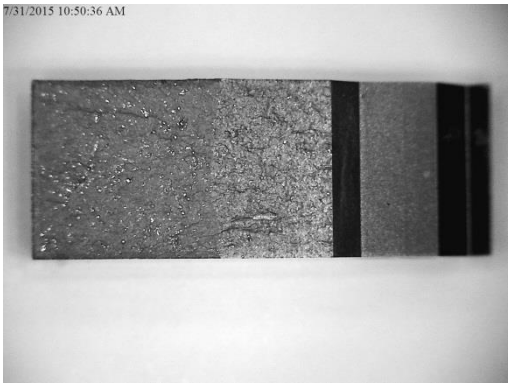

Figure 61: Longitudinal CT test piece (KL3), stress relieved

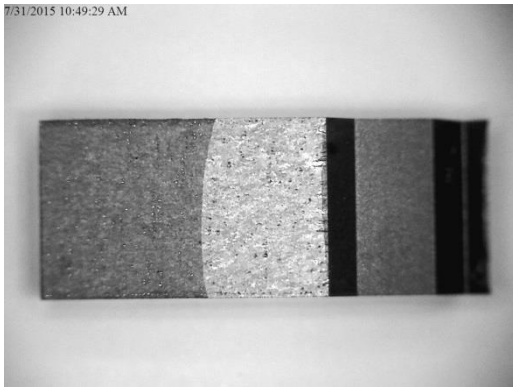

Figure 62: Transverse CT test piece (KT3), stress relieved

A study by Kumar, Prakesh and Ramamurty (2018) certainly supports the idea that the columnar structure itself influences the properties, although that was not their conclusion. They made two sets of K_{Ic} tests with the same printing parameters, but in the second test they used a rotation in scanning strategy between scanning layers, breaking up the columnar grains. While the transverse K_{Ic} tests gave approximately the same result both times, the longitudinal result without columnar grains was lower. This would seem to give an indication of the effect of the elongated grains.

Unfortunately there is little specific concrete information on the effect of the columnar grains on fracture mechanism of SLM Ti6Al4V (Simonelli, Tsea and Tuck 2014) so we cannot take for granted that this is the cause of the anisotropy.

A possible indication against the idea about the influence of prior beta grain boundaries is from the previously mentioned study by Kumar, Prakesh and Ramamurty (2018). They performed a second set of tests at a different set of printing parameters, with and without the scanning rotation intended to break up the long columnar grains, and in the set with scanning rotation both transverse and longitudinal toughness were higher. This is a very different result than expected. However due to the low energy density of the printing parameters there were not really any long columnar grains present to start off with, although the structure was markedly directional in both orientations. While the rotation in scanning strategy did cause the structure to become more equiaxed (increasing the toughness) it did not remove the columnar grains since these were not present to any significant degree to begin with.

As such it does seem reasonable that the columnar grains cause the higher fracture toughness in the longitudinal direction, but it does not explain why this does not seem to be the case for the HIP test pieces.

Microstructure

Since the previously discussed factors do not fully explain all the trends in the toughness results, it becomes necessary to take a closer look at the microstructure.

The further subject of microstructure of SLM in general is quite complicated as the kinetics of the very fine martensite (α') that forms during printing respond differently to heat treatment from conventional bulk Ti6Al4V

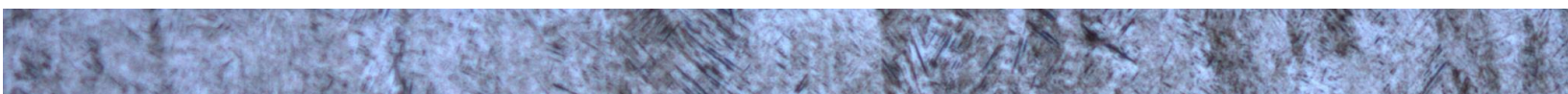

(Vrancken, et al. 2012). This is complicated by the fact that α and α' have the same structure (hexagonal) and a similar lattice parameter (c/a for 1.58 for α', against 1.59-1.60 for α (Kumar, Prakash and Ramamurty 2018)) which makes the difference difficult to analyse. There is also remarkable little to be found about the formation of α', and even less about α'' martensite, to study for comparison.

As previously mentioned, heat treatment as performed on the test pieces causes the martensite of the as-built material to decompose into α and β phase. However during rapid cooling (defined as at least 3 °C/s for Ti6Al4V (Sieniawski, et al. 2013)) after heat treatment, a small amount of new α' can form from β (Vilaro, Colin and Bartout 2011). HIP, whether sub-transus or super-transus, is followed by slow furnace-cooling, and as such would not give new α' a chance to form.

This gives rise to the idea that another possible difference between stress relieved and HIP pieces is the presence of a small amount of martensite, as stress relief heat treatment tends to be followed by air-cooling. It is difficult to find exact cooling rates for comparison, but air cooling of half-inch steel bars is at about 5 °C/s (Chandler 2007) so cooling of smaller test pieces would presumably be faster, putting is in the range where martensite could be formed. Some indication confirming this idea is a paper (Cain, et al. 2015) in which stress relief was done on SLM Ti6Al4V, but was followed by slow furnace-cooling, as is more usually the case with HIP. Cain, et al. (2015) performed compact tension tests on test pieces stress relieved at 890 °C for two hours followed by furnace cooling. The result of these tests is a fracture toughness of 49 MPa√m, with no meaningful difference between the longitudinal and transverse directions.

So depending on the temperature of heat treatment, some α' might be formed upon rapid cooling after heat treatment, along with the normal α and β. Martensite is known to have high strength and poor ductility and toughness, so the presence of α' will reduce the toughness, presumably to the point where the prior β grain boundaries are the only factor giving any boost to the toughness. But pure lamellar α+β phase is known for having high toughness and multiple factors – α cluster size, lamellar thickness, grain boundary β – could overshadow the effect of prior β grain boundary.

This is conjecture, and is somewhat contradicted by Vranken, et al. (2012) who found that cooling rate does not have a significant impact on the mechanical properties after sub-transus heat treatments, with more influence for treatments at higher temperatures approaching transus. However they only performed tensile tests, and fracture toughness is known to be influenced by more factors than pure tensile testing.

So far the indication does seem to be that it could be martensite present in traditional stress relieved pieces contributing to anisotropy, and one of the reasons HIP is more isotropic has to do with the lack of martensite.

Cain, et al. (2015) performed fracture toughness tests on test pieces heat treated at 650°C followed by slow cooling, with the results also showing isotropy in the longitudinal and transverse directions, seemingly confirming the conclusion that slow cooling after heat treatment leads to isotropy. This result is somewhat questionable because the temperature of heat treatment is neither high enough to facilitate full transformation of all α' to α+β in the first place, nor completely eliminate the residual stresses. So while there may have been slow cooling after heat treatment this example cannot be said to count as evidence since there were other factors

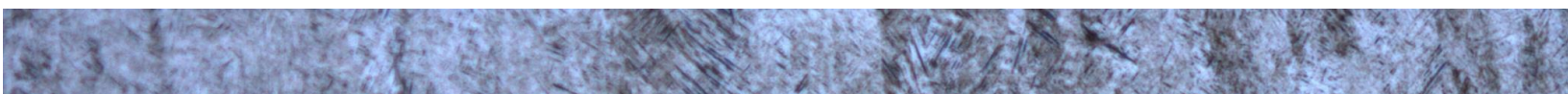

present and most likely it is a coincidence that the effects of residual stress and residual martensite negate each other in this case.

The only factor remaining putting some doubt into the idea of martensite lowering the toughness and thereby causing anisotropy is the behaviour of the short transverse direction, as described in Figure 63.

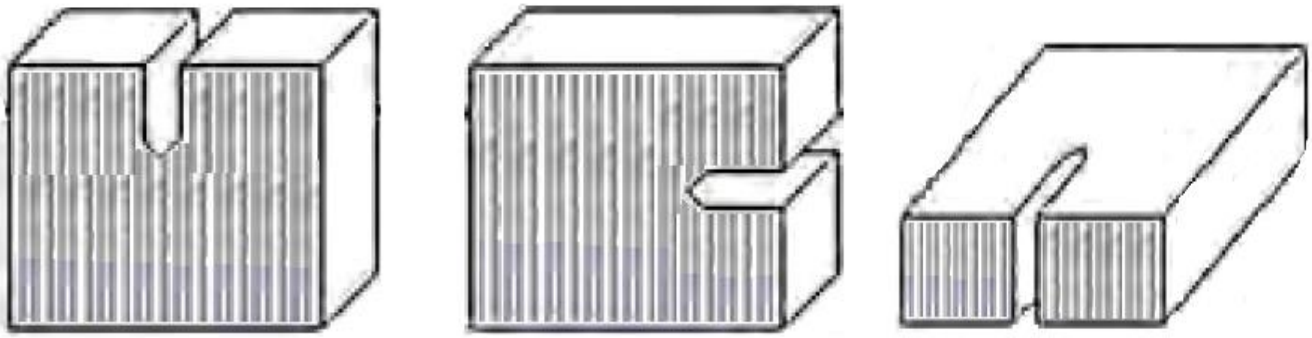

Figure 63: Elongated grains in transverse, Longitudinal and 'short-transverse' compact tension test pieces

Cain, et al. (2015) did not just test the longitudinal and transverse directions (in which both had the same fracture toughness as mentioned above) but also the short-transverse direction. For heat treatment at 890 °C followed by slow cooling the short-transverse direction showed a fracture toughness of 41 MPa√m, compared to the 49 MPa√m of the other two directions. They give no reason for this apart from that it might be related to microstructure, but it does go against the idea that no martensite means no anisotropy.

This is merely one result, though. Hartunian and Eshragi (2018) is one of the few other cases in which fracture toughness of furnace-cooled stress relief (performed at 850 °C) was examined. They found 62 MPa√m for longitudinal, 58 MPa√m for transverse and 56 MPa√m for short-transverse. However they also report severe issues with printing parameters (low energy density) causing voids, cracks and un-melted regions of powder which could all cause anisotropy. Another issue is that they report their toughness values as K_Q (the conditional stress intensity factor), not K_{Ic}, implying that the test results were not checked for validity. As such it is not clear how to interpret the exact results achieved here.

As such it seems safe to assume that the theory that the columnar prior beta grains only cause toughness anisotropy in the presence of martensite is sound, single test result in short-transverse direction from Cain, et al. (2015) notwithstanding.

A point to keep in mind is that during high temperature heat treatment with a too low cooling rate α phase can form preferentially at the prior beta grain boundary (Vrancken, et al. 2012) which is known to cause premature failure in the transverse direction (Prasad Rao, Angamuthu and Bala Srinivasan 2008). Since there is some grain boundary α in the HIP samples (see for example Figure 51) so this might have had an effect here, but since the toughness results for the HIP pieces are isotropic (as they usually are in literature) that does not seem to be the case. At any rate, while slow cooling might be advantageous in reducing anisotropy, care must be taken that the cooling rate is not too low.

Trends in Fatigue

Before discussing fatigue in more detail, tensile strength must be considered, since fatigue and tensile strength are known to scale together.

The values obtained for tensile strength compare well to those found in literature. The tensile strength of HIP pieces appeared to be somewhat lower than stress relieved pieces tests but this trend could not be concluded to be statistically sound. The situation is different for the results of the hardness tests, where the HIP values are definitively lower than stress relieve. However no statistically significant difference between the longitudinal and transverse values could be confirmed, although transverse appears to be lower.

It is known that for many metals that the hardness scales to tensile strength (ASTM International 2007), and the hardness tests confirm lower values for HIP pieces. This correlation is not often used for titanium alloys because the results are not as unambiguous as they are for steel (Leder, et al. 2017), but the general correlation still applies (Kahveci and Welsch 1991). Because of the hardness results we can then tentatively confirm that the tensile strength is also lower for the HIP pieces.

Now we can return to the connection between tensile strength and fatigue. Due to the Hall-Petch relation, which is known to hold for lamellar Ti6Al4V (Zhao, et al. 2016) yield strength is inversely related to the square root of lamella thickness. The effect on fatigue limit is more questionable. According to ASM International Fatigue and Fracture Handbook (1996) there is no correlation found between tensile strength and fatigue limit for Ti6Al4V, although the values are known to scale for other materials. However Hosseini (2012) found that the fatigue limit of Ti6Al4V is significantly higher with a higher tensile strength, which is achieved by reducing grain size. This is due to the lamellas acting as a barrier to dislocation movement: finer lamellas reduce slip length (Baufeld, Van der Biest and Gault 2010), impeding fatigue crack initiation (Rafi, Starr and Stucker 2013). This would all imply that the coarser HIP structure, having a lower tensile strength, would have a lower fatigue limit than fine, stress relieved Ti6Al4V, but the opposite is the case. Clearly grain size is not the most significant factor influencing fatigue limit. We've seen that HIP pieces have more β phase, and that the α/β boundary can be an initiation point for fracture but a more detailed look at the factors influencing the fatigue limit is necessary before coming to any conclusions.

Results of fatigue testing

Fatigue behaviour is sensitive to a number of factors to a degree that static tension is not. The interaction between microstructure and fracture path has a strong influence on crack initiation, both of which are susceptible to factors specific to SLM, like porosity, build orientation and post-processing treatment (Cain, et al. 2015). While this means there are a significant amount of factors that must met taken into account, it is also the case that these factors have different levels of influence (Chan 2009) and, a few of them can dominate the outcome.

When discussing fatigue results it is important to note that high-cycle fatigue is very different from low-cycle fatigue. Up to 90% of the life of high-cycle fatigue is taken up by crack nucleation (ASM International 1996) whereas the life of low-cycle fatigue is mostly a factor a crack extension (Pederson 2002). For this reason literature on low-cycle fatigue will not be taken into account during this discussion.

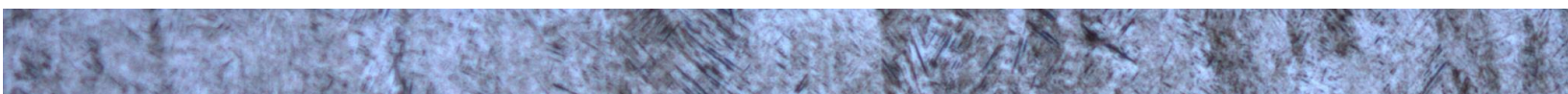

In regard to discussing the results of the high-cycle fatigue tests there a couple of trends that need to be considered. Firstly, the fatigue limit for HIP pieces is notably higher, and there seems to be less spread in the test results. This is fairly typical for SLM test results. Additionally the results for HIP pieces are isotropic, while the longitudinal fatigue limit appears to be lower the transverse for stress relieved test pieces, although this might be an artefact of high spread combined with a small sample size. While Edwards and Ramulu (2014) also found the high-cycle fatigue limit of non-HIP pieces to be lower in the longitudinal direction, this is a single result and therefor is not sufficient evidence that this would always be the case, especially since there are some factors that initially seem to indicate the opposite. The direction of the elongated grains means that more grain boundaries (i.e. defects for fatigue initiation) are available at the surface for transverse test pieces, which would make it more likely for a crack to initiate earlier. Also the tension is parallel to the prior β grain boundaries, which are weaker as we have previously determined, and so would be more susceptible to mode I opening failure. Another point is that the elongated grains mean that there are effectively smaller grains in the longitudinal direction which should give higher fatigue limit.

There are however other factors that play a very significant role. Slip planes for fatigue crack nucleation and stage I crack growth tends to be at 45° to the applied force. As we have previously seen, in the SR longitudinal test pieces α lathes strongly tend to 45° with the building direction due to epitaxial growth and phase transformation from β to α'. This means that there are a significant amount of favourably oriented grains for crack initiation to follow, and an investigation of the initiation point of a longitudinal test piece (Figure 64) shows that this is just what happens. This effect would sharply reduce the fatigue limit in the longitudinal direction by facilitating initiation.

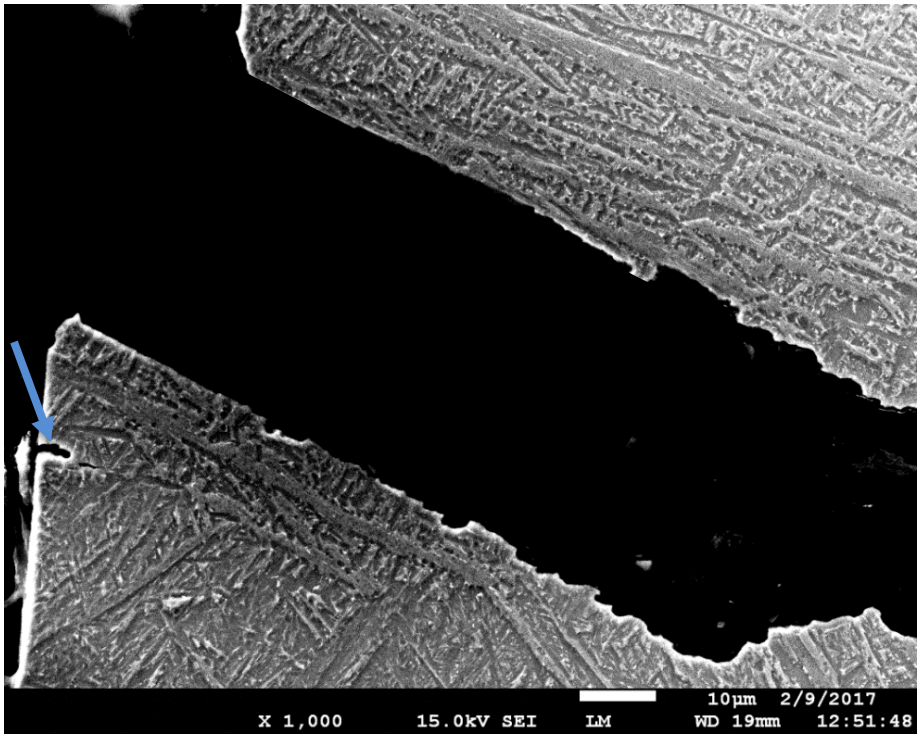

Figure 64: Initiation in FL5 following microstructure. secondary cracking below main crack.

Apart from the microstructure, which clearly plays a significant role in crack initiation, we have to look at the impact of porosities. In general Ti6Al4V is known to have a low notch sensitivity in fatigue due to the hexagonal α phase having a low amount of slip systems/directions and there would have to be a favourably oriented grain at the tip of the notch for it to have a significant effect (Razavi, Ferro and Berto 2017). However since the longitudinal SR test pieces strongly tend to favourably oriented grains this increases notch sensitivity. This would also increase the sensitivity to (near) surface defects.

The stress relieved test pieces contain numerous porosities, most significantly LOF porosities which are sharp and can easily be opened in mode I tension for the longitudinal test pieces, see for example the LOF defect in Figure 65. In these cases the dependence of the fatigue limit on crack nucleation is reduced, since there is effectively already a crack present.

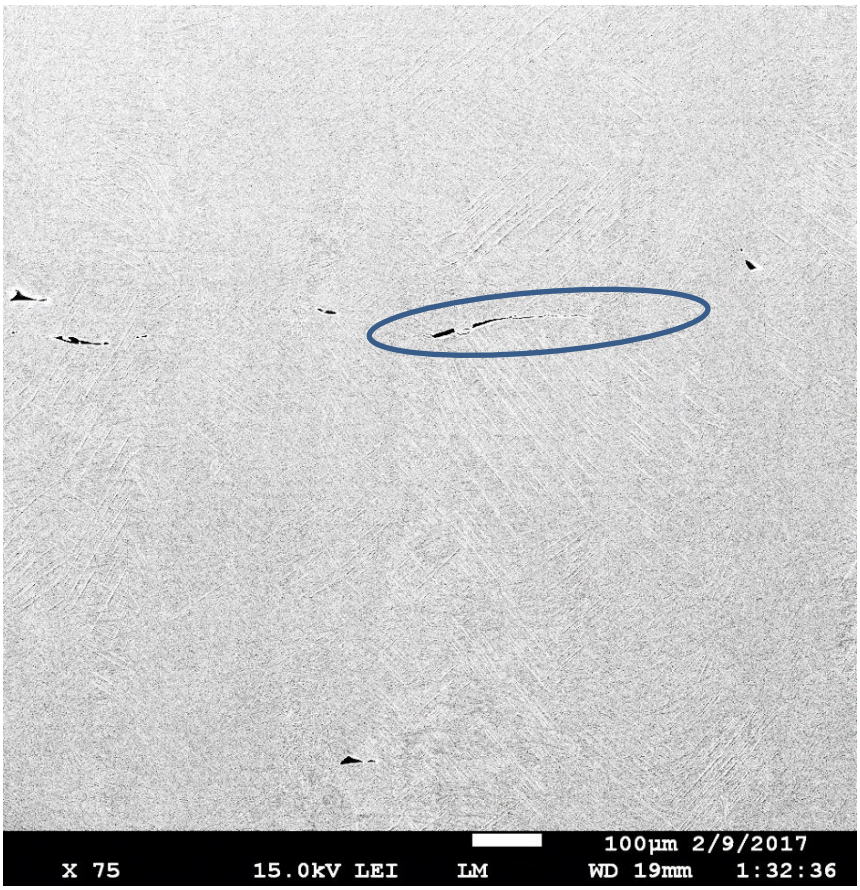

Figure 65: Lack of fusion defects and secondary crack initiation in FL5

Although fatigue crack initiation usually occurs at the surface, the stress concentration due to the LOF porosities is enough to cause crack formation at internal porosities.

Of course there are other forms of porosities apart from LOF defects. When a gas porosity or similar is at or near the surface this can also facilitate crack initiation. Notably, according to Leuders, Thöne, et al. (2013) porosities sufficiently far from the surface will not have this effect, not even cluster of porosities. They do not

mention LOF defects, though, which as could be seen in Figure 65 can clearly can initiate fracture even far from the surface. At any rate the effect of near surface porosities can explain the scatter we see in the SR fatigue limit. Gas porosity and the like is randomly distributed through the material at various distances from the surface (see Figure 66). When there is a porosity near enough to the surface this may facilitate cause crack initiation, lowering the fatigue limit.

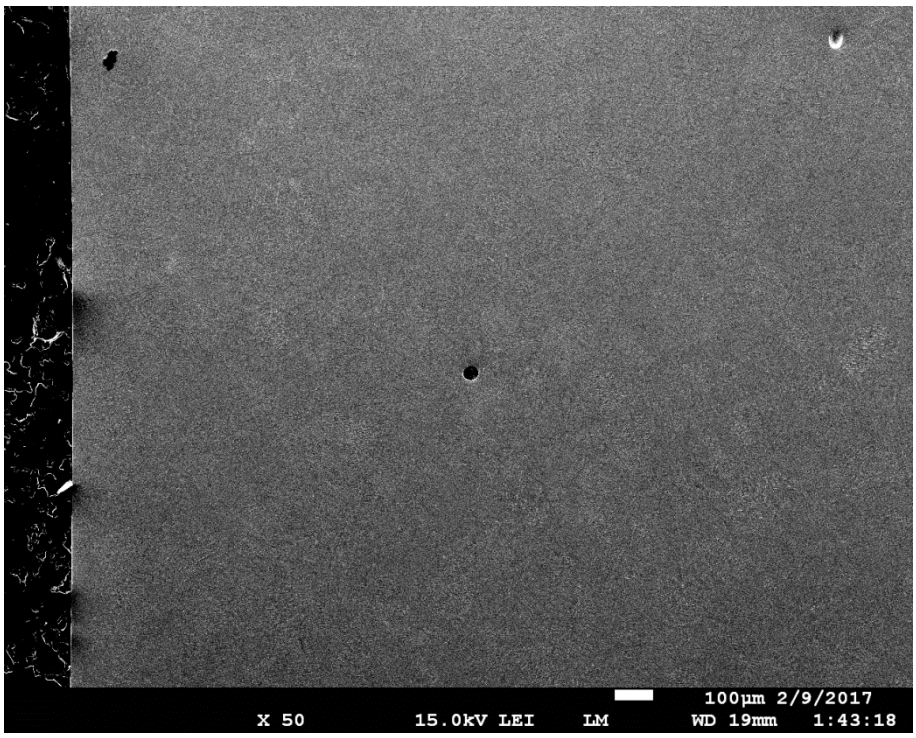

FIGURE 66: GAS POROSITIES IN FT2

The behaviour of the various kind of porosities and reaction of fatigue limit to the microstructure seems to confirm that the fatigue limit is lower in the longitudinal direction, as well as giving some evidence for why the SR fatigue limit in general is lower, and why these show a significant degree of scatter. However when investigating these factors, it was found that while there are porosities present in transverse test pieces, there seem to be more than twice as many porosities readily found in the longitudinal test pieces, mostly in the radius, and most of these are LOF defects. This would of course also have a marked effect on lowering the longitude fatigue limit. Further investigation also shows that there is a concentration of porosities at the top (the last printed) section of test pieces – in toughness test pieces as well as fatigue. This would not have influenced the tested values as the position of crack initiation was forced, but in a part built by SLM such a concentration of porosities will have a significant effect.

While the above discussion covers factors influencing the difference in trends of values between the sets of tests, factors that may influence the base values also need to be considered.

Practical Application

While we now know the major factors influencing the trends in fracture toughness and high-cycle fatigue limit, this does not tell us anything about whether or not these values make SLM Ti6Al4V suitable to use for reciprocating compressor pistons as initially suggested. In order to do that we need to take a look at the specific design requirements.

Fracture toughness is an important property for piston operation, but it is not explicitly used in the design calculations. However it is used as a basis for the approval criteria of non-destructive examination of various compressor parts. On the most critically loaded sections of pistons, no feature presenting as a surface crack is allowed and must be ground out, but subsurface defects can be approved up to a certain depth. In fact, any possible defect found by means of non-destructive examination like ultrasonic or magnetic testing less than 1.6 mm in size is disregarded as an indication and need not even be approved or noted, and as such could always be present in a finished piston. Within standard piston design a defect depth of 1.6mm is essentially taken as a sub-critical crack for the stress intensity factor of currently used piston materials. The stress intensity factor of SLM Ti6Al4V matches, or is superior to, the stress intensity factor of currently used piston materials (see Table 2). Additionally within a given set of parameters both the Charpy V-notch energy and the fracture toughness has proven to be consistent, with little spread. In terms of toughness, there are no issues with the application of SLM Ti6Al4V for compressor pistons.

Evaluating the suitability of Ti6Al4V in terms of fatigue is more complicated. Let's start with how fatigue in general is assessed for application in compressor piston design calculations. The given fatigue limit is adjusted for surface roughness, wall thickness of the part, and stress concentration. This is then the P(50) fatigue limit for the given part, i.e. the value at which 50% of parts will eventually fail. However Howden Thomassen Compressors uses a 0.02% acceptable failure rate (i.e. 3.54 standard deviations below the average value), making for a sizable reduction in the allowable fatigue stress, depending on the standard deviation of the fatigue limit. This is then compared to the actual stresses as calculated, using the Goodman relation to adjust for the mean stress that occurs due to a combination of static and dynamic loading. The actual details of the design calculations are proprietary information and cannot be shared here, but the end result can be compared to the given values. Just as a sidenote – due to the comparatively low strength, fatigue limit, and stiffness of the applied aluminium alloys, there is a slightly adapted design and calculation specific for aluminium pistons. However, because aluminium pistons are rarely still applied, in part due to the failure rate, this design and calculation will not be further considered here.

Goodman Equation

The Goodman equation is sometimes applied to SLM materials (Witkin and Albright 2016) and there does not seem to be any indication that it is less suited to SLM than it is for conventional materials. The use of Goodman for Ti6Al4V specifically is more controversial. It is often said to be insufficiently conservative for the fatigue behaviour of Ti6Al4V, as it can be mean stress sensitive, particularly in high cycle fatigue (ASM International 1996). The Goodman equation has been shown to be appropriate for use with lamellar Ti6Al4V (Chan 2009) (Witkin and Albright 2016), but not for an equiaxed (Chan 2009) or bimodal (Peters, et al. 2000) structure. Sometimes alternative equations are suggested for specific structures, as done by Chan (2009), but these tend to involve facets of the microstructure into the equation which may be known in the lab but would not be available

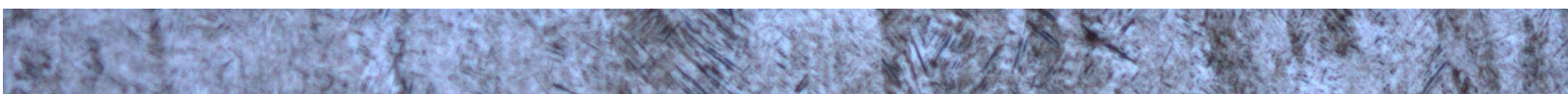

information for an one-off industrial application. Moreover, no mention is made of fine acicular structure or martensite as is found in as-built and stress relieved SLM Ti6Al4V as this is not a structure that occurs in conventional Ti6Al4V.

It has already been found that the fatigue behaviour of SLM Ti6Al4V is anisotropic to a far greater degree than the tensile strength, so it may well be that the influence of mean stress varies with the orientation of the stress. The mean stress sensitivity of Ti6Al4V is also known to be influenced by the angle between texture and loading direction (ASM International 1996) but since there is little to no texture in SLM Ti6Al4V due to the phase transformation during cooling this would probably have less of an effect.

HIP Ti6Al4V has a lamellar structure so the Goodman equation will likely be applicable in this case, barring unknown effects due to differences in orientation. The only reference for non-HIP Ti6Al4V is the use of the Smith-Watson-Topper (SWT) model for to fit HCF data for longitudinal stress relieved SLM Ti6Al4V (Benedetti, Fontanari, et al. 2018). In the SWT model the fatigue limit at R=-1 is calculated by taking the square root of the product of the alternating stress and maximum stress as follows:

$$\sigma_{R=-1} = \sqrt{\sigma_{alt}\sigma_{max}}$$

according to Dowling, N.E (2004).

There is no further mention of the applicability for different orientations, but for lack of more information the SWT model will be used for stress relieved Ti6Al4V here.

Size effect

The fatigue values we have obtained are valid for the size of the test pieces they were performed on, but there are however a number of reasons why these values may be different for full-size parts. Materials contain a statistical spread of defects and flaws. Everything else being equal, material with a greater thickness will have a greater chance of having a critical flaw at a given section. As such the strength of a material is known to be lower for larger through-sections. Additionally there are practical reasons why materials with strength caused by heat treatment dependant on a critical cooling rate – like the formation of martensite in Ti6Al4V – will have a lower strength for larger parts. The greater the thickness of the section, the more slowly the part will be able to cool, with greater cooling rates at the surface than at the centre of the section. A lower cooling rate means a lower hardness, down to a point at which the cooling is no longer sufficient for martensite to form. Furthermore, the test pieces for fatigue and tensile testing were small enough that fracture is at or near plane stress, while a larger part this will not necessarily be the case. This might not influence crack initiation, but will have an effect on crack growth.

A complicating factor is that HCF crack initiation usually occurs on the surface of the material, and while a larger part will have a larger circumference, the increase in circumference does not scale directly with the increase in thickness.

While there are a number of reasons to suspect that the fatigue resistance of a large part may be lower than that of a test piece, unfortunately there is little to be found in terms of concrete information on what that

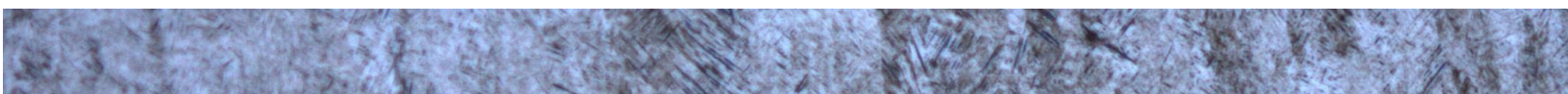

difference may be, whether for Ti6Al4V or for SLM materials specifically. SLM in particular poses a problem of its own, since while there will be some scaling to mechanical properties due to the relative size of the microstructure compared to the size of the component, we also have that the microstructure is significantly anisotropic, meaning that the scaling of the properties might be anisotropic as well. While there is some indication that the size effect for stress relieved SLM Ti6Al4 is not particularly strong (Chellu 2022) there is not much hard data to work from. For this reason the standard factors used for conventional piston materials will be used for the piston fatigue calculation.

Surface effects

In the standard calculation for conventional piston materials the surface coefficient by which the fatigue strength is adjusted is simply a factor of roughness, increasing as the roughness (measured in R_a) increases. There is some information available for the effect of surface treatment and roughness on the fatigue limit of conventional Ti6Al4V (ASM International n.d.). However in actual fact the effect of roughness is far more complicated, especially since the surface state of a material is far more complex than simply the average roughness as quantified by R_a. Additionally there is some indication that for a given level of porosity decreasing the roughness has no effect on the fatigue limit since the effect of the porosities overpower any surface effect (Cheylus 2017). In these cases removing general surface roughness associated with SLM can expose subsurface porosities (Benedetti, Fontanari, et al. 2018) so for this reason there can be no guarantee that reducing surface roughness increases fatigue life. However most sources tend to agree that improving the surface will tend to increase the fatigue limit (Chastand, et al. 2016), even though the effect is greater for HIP material (Masuo, et al. 2018). Vayssette, et al. (2017) report an increase in the fatigue limit of HIP Ti6Al4V of 2.5 times by polishing the surface, compared to the as-built surface, which is what will be used here. For non-HIP Ti6Al4V the situation is more complicated since polishing the surface may have no effect, up to the case of (Chastand, et al. 2016) where polishing delivered an increase in the fatigue limit of 2.3 times. The most conservative case will be used in the calculations to follow. It must be noted that both these factors are far greater than what is usually taken for a roughness effect of structural materials.

Fatigue Stress Calculation

The information gathered in previous sections can be used to make an approximation of the piston calculation for allowable fatigue stress, for which a maximum allowable pressure differential can be calculated.

Typically the highest alternating stress in a piston is at the piston rings or at the radius of the ribs, see Figure 67. For these cases the load is near or at the same orientation as for the longitudinal test pieces.

In conventionally manufactured pistons the piston ring groove is formed by machining, giving a smooth surface that is advantageous both for fatigue properties and for prevention of wear of the piston ring. Conversely the surface of the ribs is usually left as-is, although in some cases it would be polished to avoid casting defects. For the sake of the calculation both as-built surface and machined surface will be considered.

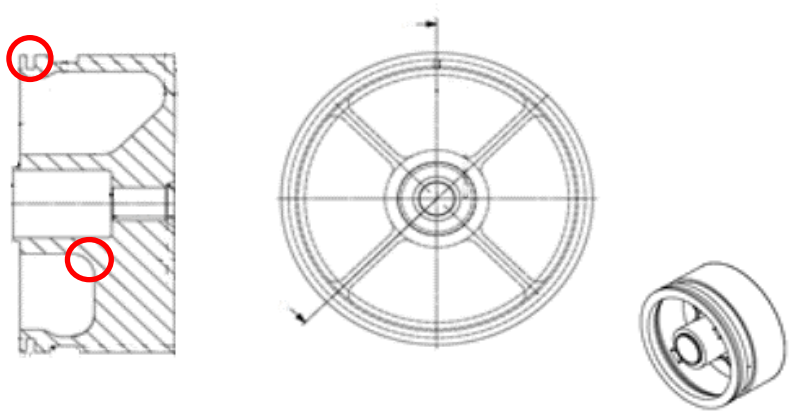

FIGURE 67: TYPICAL PISTON HALF WITH TYPICAL POSITIONS OF HIGH ALTERNATING STRESS INDICATED IN RED.

It is possible to adjust the dimensions of the piston in order to reduce the stress at a given position, but for the sake of the calculation typical dimensions will be used.

The details of the calculation is proprietary information, but the steps taken and results thereof can be seen in Table 11.

TABLE 11: RESULTS OF PISTON CALCULATION

	Stress relieved		HIP	
	L	T	L	T
Input – fatigue calculation				
Tested alternating fatigue limit R=0.1	83 MPa	126 MPa	176 MPa	174 MPa
Calculated fatigue limit R=-1 (Goodman and SWT)	124 MPa	188 MPa	221 MPa	217 MPa
Standard correction factor for section thickness ~50 mm	0.8	0.8	0.8	0.8
Correction factor for surface roughness	1/2.3	1/2.3	1/2.5	1/2.5
Calculated result – fatigue calculation				
Allowable alternating stress P(50)	49 MPa	74 MPa	81 MPa	79 MPa
Allowable alternating stress for 0.02% failure rate	13 MPa	56 MPa	73 MPa	72 MPa
Allowable alternating stress at R=0 acc. Goodman and SWT	9 MPa	39 MPa	68 MPa	67 MPa

Calculated result – standard piston calculation				
Allowable pressure differential for typical dimensions	6 bar	24 bar	43 bar	42 bar
Allowable pressure differential for machined surface	12 bar	50 bar	86 bar	85 bar

Reciprocating compressors are suitable for a range of pressure ratios – as low as 1.1 when approaching high pressures around 180 bar, and usually no higher than 3 for lower pressures. A pressure differential of 40 to 80 bar should therefore be able to cover all applications, but a pressure differential of 6 bar will rarely be sufficient.

This effectively means that the fatigue limit of non-HIP Ti6Al4V as found in this study is too low for much practical application. Part of the problem is the high scatter in values due to porosity, which gives low value for safe usage. One could simply apply HIP material, but if possible it would be better to be able to skip an expensive logistical step, both for the sake of cost and to shorten delivery times.

POSSIBLE IMPROVEMENTS

The reason for the low applicability of non-HIP Ti6l4V in this case is the high-stress sections of the structure are ideally oriented for crack initiation, and the high degree of porosity that lowers the fatigue strength and increases the scatter. These are both topics that can be addressed.

The simplest way to change the microstructure is by heat treatment. By means of high temperature heat treatment the lamellar structure can be transformed to bimodal or globular Ti6Al4V. Brand, et al. (2013) achieved a bimodal structure by heat treating at 970 °C and water quenching, followed by a longer soak at 700°C and air cooling. The bimodal structure is particularly advantageous since it is known to have a good fatigue strength (Ghonem 2010) and many of the calculation factors for application in the previous section are known for bimodal Ti6Al4V. However lamellar Ti6Al4V is known to have a higher fracture toughness than bimodal, so it would become necessary to check that these values do not drop below useful limits.

The structure can also be influenced by changing the printing process. Rotating the scanning direction between layers breaks up the columnar grains (Kumar, Prakash and Ramamurty 2018), leaving an equiaxed structure that is no longer oriented for fatigue crack initiation in the longitudinal direction. Presumably this would increase high cycle fatigue limit, although this has not yet been proven.

Likewise there are a number of ways to influence the amount and type of porosities that form during printing. The simplest way is to simply have a re-melting run after every layer has been completed. A relatively high scanning speed (200 m.s-1) and low laser power (85 W) has been shown to have the best results (Kruth, et al. n.d.).

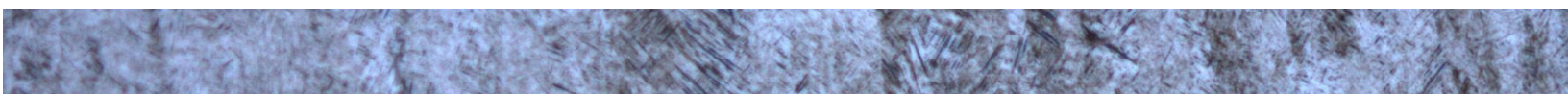

Many published studies without re-melting contain non-HIP Ti6Al4V without porosities (e.g. Rafi, Starr and Stocker (2013) and Cain, et al. (2015)), so it is possible. However in these cases the printing parameters used are not fully reported, so the ideal parameters would still have to be determined.

According to Vilaro, Colin and Bartout (2011), the number of defects can be reduced by reducing the scanning speed and layer thickness and increasing the laser power, which specifically reduces disc-shaped LOF defects (Wu and Lai 2016). This will also slow printing and make the end-product more expensive (Kruth, et al. n.d.). Additionally a too low scanning speed (starting around 150 mm/s according to Kruth, et al. (n.d.) or too high laser power can cause instability of the melt pool, which leads to irregular defects in the build-plane (Thijs, et al. 2010). Conversely, in order to reduce the amount of gas porosities it is necessary to reduce the solubility and amount of gas in the liquid, which means thinner layers and low laser power (Vilaro, Colin and Bartout 2011). This means that there is some ideal balance between the different printing parameters, since reducing the different kinds of defects means adjusting the printing parameters in contrasting directions.

In the test pieces for this study, more defects were found around the top of the test pieces, and within the narrow radius of the tensile test pieces. This is in contrast with Simonelli, Tsea and Tuck (2014) who did not find any variation in the defect concentration in orientation or distance from the build plate. However it is known that the relatively low thermal conductivity of Ti6Al4V means that the energy input from the laser disperses more slowly with increasing distance from the build plate for high, relatively thin-walled parts (Carroll, Palmera and Beesea 2015). This will influence the formation of defects since the lower cooling rate means slower solidification and in effect less heat input will be necessary for the same size melt pool. Printing parameters are typically kept constant during a print so in a narrower section, or at greater distance from the build plane, the change in heat dissipation causes an effective increase in heat input. This giving a larger chance of melt pool instability defects.

Of course the change in cooling rate does not only affect the likelihood of the formation of defects. At a greater distance from the build-plane the reduction in cooling rates cause the microstructure to become coarser by an increase in lathe width (Carroll, Palmera and Beesea 2015). However some sources report no difference in structure with distance from the build plane (Brandt, et al. 2013) so presumably if this effect occurs will depend on the part dimensions and chosen printing parameters.

As previously discussed, this coarser structure will increase fracture toughness but decrease the high-cycle fatigue limit. This is unfavourable since the fatigue limit has proven to be the limiting factor for this application, especially when considering the likely orientation of the piston on the build plate. It would be simplest to print a piston-half with the face downward and ribs and opening towards the top. This would mean that the most critical areas in the part are closer to the top (see Figure 67) where a coarser structure would cause a lower fatigue limit. If you fabricate the part the other way around you could end up needed internal supports that would have to be removed after. This might turn out to be an acceptable compromise.

In short, care must be taken when designing a part to be suitable for SLM, particularly when high-cycle fatigue is of importance. Avoid narrow, tall sections and significant changes to section thickness.

Additionally the proper printing parameters should be selected not just with the material in mind, but also the shape of the part.

There are a number of alternative approaches to the problems posed by selective laser melting. Shot-peening is often used to increase the high-cycle fatigue limit of rough cast parts by inducing surface compressive stress. It stands to reason that this will also be applicable to SLM parts and this is supported by some research (Benedetti, Torresani, et al. 2017). However there are also some indications that shot-peening is not particularly effective in increasing the fatigue strength of SLM parts (Wycisk, et al. 2013), especially in cases where the fatigue strength is limited by internal porosities, since these are not affected by shot-peening (Benedetti, Fontanari, et al. 2018).

Alternatively some of the problems can be adjusted at the source. Some newer SLM machines use a heated base plate or heated printing chamber to control cooling rates, or have a vacuum chamber instead of inert gas that will likewise lower cooling rates and prevent gas porosity (Pederson 2002). These processes do need a more expensive SLM machine, and for every new process the necessary printing parameters and issues around them need to be identified. Inroads are being made in predicting material properties based on input parameters (Smith, et al. 2015), or modelling the printing process itself (Fan and Liou 2012) (Zhu, et al. 2021). In future this could help reduce the amount of testing needed to obtain appropriate printing parameters for a given process, design, and material, and obtain the mechanical properties that will result from these parameters.

Conclusions

Rapid manufacture is not often used for parts in heavy industry. However due to the problems manufacturing compressor pistons for special applications it may be the most appropriate solution. Based on readily available data it would seem them Ti6Al4V produced by selective laser melting is suitable for piston for compressor cylinders.

The results of tests performed for this study show that SLM Ti6Al4V is in fact appropriate for use for reciprocating compressor pistons. Both the fatigue limit and fracture toughness of HIP SLM Ti6Al4V, as well as other mechanical properties like the strength and hardness, make it suitable for use for reciprocating compressor pistons applications. This is in terms of the actual values, the spread, and relative isotropy of the values. However making a reliable fatigue calculation requires the use of a number of correction factors, most of which are not readily available for SLM Ti6Al4V. Extensive testing would be required to obtain accurate values for these correction factors.

Non-HIP SLM Ti6Al4V as printed for these tests is not suitable for compressor pistons. While the fracture toughness of non-HIP material is sufficiently high, the high cycle fatigue strength is too low for most applications. This is due to scatter due to the amount of porosities, as well as the microstructure of the longitudinal pieces being ideally oriented for fatigue crack initiation. It is possible to print Ti6Al4V without porosities or the detrimental microstructure, but the appropriate printing parameters for the part and material would have to be found.

While porosities and microstructure cause lower values in longitudinal fatigue limit, the trends in fracture toughness are different. It seems that the boundaries of the elongated columnar grains act as an arrestor for crack growth in the horizontal direction, increasing the toughness of longitudinal test pieces compared to transverse. After HIP and slow cooling all martensite is removed and greater lamellar thickness increases the toughness to the degree that overrides any grain boundary effect, removing anisotropy in toughness values.

Considering the multitude of factors that influence the mechanical properties of SLM Ti6Al4V, it is important to have the appropriate printing parameters for the part in question. While Ti6Al4V is one of the best documented SLM materials and in general SLM suppliers do have appropriate printing parameters, the requirements can change with part dimensions to the degree that modelling or prototype testing may be necessary to fully control the end result. However this is fine-tuning. SLM Ti6Al4V can be used for reciprocating compressor pistons. Any improvements will allow for greater control of the part and mechanical properties, and less conservative calculations, but are not critically necessary.

Recommendations

There are a couple of factors that for which more information will be helpful in order to be able to perform more accurate fatigue calculations. These are the effect of mean stress, wall thickness, and surface condition on the fatigue strength of selective laser melted Ti6Al4V. These should to be known specifically for the microstructure and printing condition that is being applied, as well is whether the factor is influenced by orientation or other factors.

If necessary there is the potential to increase the fatigue limit of stress relieved Ti6Al4V, either by reducing the amount of porosities by changing the printing parameters, or by changing the microstructure by means of heat treatment or different printing parameters. These solutions would have to be tested before application would be possible.

In order to have a good handle on the effect of different changes to the printing process we must also know that factor that influence the various properties. While the effect of residual stress, porosity, general microstructure and columnar grains are relatively clear, the effect of martensite formation during fast cooling on anisotropy could not be conclusively shown. In order to be sure of the influence of this factor this should be investigated further.

Works Cited

ASM International. n.d. *Atlas of Fatigue Curves.* ASM International.

—. 1996. *Fatigue and Fracture.* Ohio: ASM International.

—. 1990. *Handbook of Corrosion Data.* Metals Park: ASM International.

—. 2004. *Metallography and Microstructure.* Ohio: ASM International.

—. 1990. *Properties and Selection: Non-Ferrous Alloys and Special Purpose Materials.* Ohio: ASM International.

ASTM International. 2009. "ASTM A439 - Standard Specification for Austenitic Ductile Iron Castings." ASTM International.

—. 2006. "ASTM A571 - Standard Specification for Austenitic Ductile Iron Castings for Pressure-Containing Parts Suitable for Low-Temperature Service." ASTM International.

—. 2008. "ASTM B686 - Standard Specification for Aluminium Alloy Castings, High Strength." ASTM International.

—. 2007. "ASTM E140 - Standard Hardness Conversion Tables for Metals." Pennsylvania: ASTM International.

—. 2012. "ASTM F2792 - Standard Terminology for Additive Manufacturing Technologies." ASTM International. ASTM International.

Baufeld, B., O. Van der Biest, and R.S. Gault. 2010. "Additive manufacturing of Ti–6Al–4V components by shaped metal deposition: Microstructure and mechanical properties." *Materials and Design.*

Beardmore, R. 2010. *RoyMechX.* Nov. Accessed June 13, 2019. http://www.roymech.co.uk/Useful_Tables/Matter/Costs.html.

Benedetti, M., E. Torresani, M. Leoni, V. Bandini, M. Fontanari, C. Penderzolli, and C. Potrich. 2017. "The effect of post-sintering treatments on the fatigue and biological behavior of Ti-6Al-4V ELI parts made by selective laser melting." *Journal of the Mechanical Behavior of Biomedical Materials* 295-306.

Benedetti, M., V. Fontanari, > Bandini, F. Zanini, and S. Carmignato. 2018. "Low- and high-cycle fatigue resistance of Ti-6Al-4V ELI additively manufactured via selective laser melting: Mean stress and defect sensitivity." *International Journal of Fatigue* 96-109.

Biscardini, G., R. Morrison, D. Branson, and A. Del Maestro. 2019. "Oil and Gas Trends 2018-19." *Strategy and PwcC global.* Accessed March 4, 2019. https://www.strategyand.pwc.com/trend/2018-oil-gas.

Brandt, M., S. Sun, M. Leary, S. Feih, J. Elambasseril, and Q. Liu. 2013. "High-Value SLM Aerospace Components: From Design to Manufacture." *Advanced Materials Research* 135-147.

Brooks, C.R. 1990. *Heat Treatment, Structure and Properties of Nonferrous Alloys.* ASM.

—. 1990. *Heat Treatment, Structure and Properties of Nonferrous Alloys.* ASM.

Budinski, K., and M. Budinski. 1999. *Engineering Materials: Properties and Selection.* New Jersey: Prentice-Hall.

Cain, V., L. Thijs, J. Van Humbeeck, B. Van Hooreweder, and R. Knutsen. 2015. "Crack propagation and fracture toughness of Ti6Al4V alloy produced by selective laser printing." *Additive Manufacture.*

Campanelli, S.L., N. Contuzzi, A. Angelastro, and A.D. Ludvico. 2010. "Capabilities and Performances of the Selective Laser Melting Process." In *New Trends in Technologies: Devices, Computer, Communication and Industrial Systems*, by Meng Joo Er. Sciyo.

Carroll, B.E., T.A. Palmera, and A.M Beesea. 2015. "Anisotropic tensile behavior of Ti–6Al–4V components fabricated with directed energy deposition additive manufacturing." *Acta Materialia* 309–320.

Chan, Kwai S. 2009. "Roles of microstructure in fatigue crack initiation." *International Journal of Fatigue* 1428–1447.

Chan, Kwai S., Marie Koike, Robert L. Mason, and Toru Okabe. 2012. "Fatigue Life of TitaniumAlloys Fabricated by Additive Manufacturing Techniques for Dental Implants." *Metallurgical and Materials Transactions A.*

Chandler, ed. 2007. *Heat Treater's Guide.* Cleveland: ASM International.

Chastand, V., A. Tezenas, Y. Cadoret, P. Quaegebeur, W. Maia, and E. Charkaluk. 2016. "Fatigue characterization of Titanium Ti6Al4V samples produced by Additive Manufacturing." *Procedia Structural Integrity* 3168-3176.

Chellu, S. 2022. *Fatigue of additively manufactured Ti-6Al-4V using sub-sized samples.* Masters Thesis, Delft: TU Delft.

Chen, J., Y. Verreman, and J. Lanteigne. 2013. "On fracture toughness JIC testing of martensitic stainless steels." *13th International Conference on Fracture* . Beijing.

Cheylus, T. 2017. "Fatigue Crack Initiation Behaviour of Additive Manufactured Ti-6Al-4V." Masters Thesis, Delft.

Christ, H. J., O. Duber, W. Floer, U. Krupp, C. P. Fritzen, B. Kunkler, and A. Schick. n.d. "Microstructural effects on short fatigue crack propagation and their modelling." In *Micromechanisms in Fracture and Fatigue.*

CIA. 2019. "Country Comparison - Oil Consumption." *The World Factbook.* 28 February. Accessed March 4, 2019. https://www.cia.gov/library/publications/resources/the-world-factbook/.

Cvijovic-Alagic, I., N. Gubeljak, M. Rakin, Z. Cvijovic, and K. Geric. 2014. "Microstructural morphology effects on fracture resistance and crack tip strain distribution in Ti–6Al–4V alloy for orthopedic implants." *Materials and Design* 870–880.

Donachie, M.J. 2000. *Titanium: A Technical Guide, 2nd Edition.* ASM International.

Dowling, N. E. 2004. "Mean Stress Effects in Stress-Life and Strain-Life Fatigue." (Society of Automotive Engineers, Inc.).

Dutta, B., and F.H Froes. 2017. "The Additive Manufacturing (AM) of titanium alloys." *Metal Powder Report* 96-106.

Edwards, P., and M. Ramulu. 2014. "Fatigue performance evaluation of selective laser melting Ti6Al4V." *Materials Science & Engineering A* 327-337.

European Comittee for Standardization. 2004. "EN 10168 - Steel products - Inspection documents - List of information and desciption." European Comittee for Standardization.

—. 2004. "EN 10204 - Metallic products - Types of inspection documents." European Comittee for Standardization.

—. 1999. "EN 10250-4 - Open die steel forgings for general engineering purposes - Part 4: Stainless steels." European Comittee for Standardization, Nov.

—. 2012. "EN 13835 - Founding - Austenitic cast irons." European Comittee for Standardization, January.

—. 2010. "EN 1563 - Founding - Spheroidal graphite cast iron." European Comittee for Standardization.

—. 1994. "EN 586-2 - Aluminium and aluminium alloys - Forgings - Part 2: Mechanical Properties and additional property requirements." European Comittee for Standardization, Nov.

European Comittee of Standardization. 2008. "EN 1706 - Aluminium and aluminium alloys - Castings - Chemical composition and mechanical properties." European Comittee of Standardization, August.

Fan, Z., and F. Liou. 2012. "Numerical Modeling of Additive Manufacturing (AM) Processes of Titanium ALloy." In *Titanium Alloys – Towards Achieving Enhanced Properties for Diversified Applications*, by A.K.M Nurul Amin, 3-28. intechopen.

Fatemi, A., and L. Yang. 1998. "Cumulative fatigue damage and life prediction theories: a survey of the state of the art for homogeneous materials." *International Journal of Fatigue* 9-34.

Frazier, William. 2014. "Metal Additive Manufacturing: A Review." *Journal of Materials Engineering and Performance* 1917-1928.

Ghonem, Hamouda. 2010. "Microstructure and fatigue crack growth mechanisms in high temperature titanium alloys." *International Journal of Fatigue* 1448-1460.

Gibson, I., G. Goenka, R. Narasimhan, and N. Bhat. n.d. "Design Rules for Additive Manufacture." 705-716.

Gu, D. 2015. *Laser Additive Manufacturing of High Performance Materials.* Berlin: Springer.

Gu, D.D., W. Meiners, K. Wissenbach, and R. Poprawe. 2012. "Laser additive manufacturing of metallic components: materials, processes and mechanisms." *International Materials Reviews.*

Hartunian, P., and M. Eshraghi. 2018. "Effect of Build Orientation on the Microstructure and Mechanical Properties of Selective Laser-Melted Ti-6Al-4V Alloy." *Journal of Manufacturing and Materials Processing.*

He, B., W. Wu, L. Zhang, L. Lu, Q. Yang, Q. Long, and K. Chang. 2018. "Microstructural characteristic and mechanical property of Ti6Al4V alloy fabricated by selective laser melting." *Vacuum* 79-83.

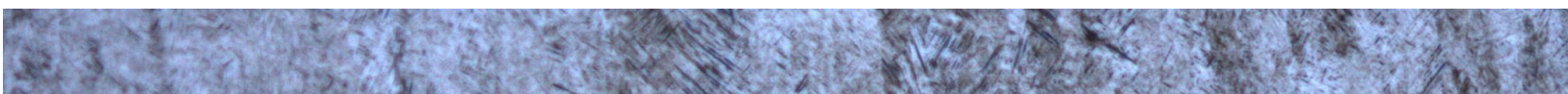

Hosseini, Shabnam. 2012. “Fatigue of Ti-6Al-4V.” In *Biomedical Engineering - Technical Applications in Medicine*, by R. Hudak, M. Penhaker and J. Majernik. InTech.

Huang, Q., N. Hu, X. Yang, R. Zhang, and Q. Feng. 2016. “Microstructure and inclusion of Ti-6Al-4V fabricated by selective laser melting.” *Front. Mater. Sci.*

International Council on Combustion Engines. 2009. “Guidance for evaluation of Fatigue Tests.”

Joshi, V.A. 2006. *Titanium Alloys: An Atlas of Structures and Fracture Features.* Boca Raton: Taylor & Francis.

Kahveci, A. I., and G. E. Welsch. 1991. “Hardness versus strength correlation for oxygen-strengthened Ti6Al4V alloy.” *Scripta Metallurgica* 1957-1962.

Kruth, J.P., M. Badrossamay, E. Yasa, J. Deckers, L. Thijs, and J. Humbeeck. n.d. “Part and material properties in selecive laser melting of materials.” *16th International Symposium on Electromachining.*

Kumar, P., O. Prakash, and U. Ramamurty. 2018. “Micro-and meso-structures and their influence on mechanical properties of selectively laser melted Ti-6Al-4V.” *Acta Materialia* 246-260.

Leder, M., A.V. Volkov, A. Grebenschikov, N. Volkova, and K. Rusakov. 2017. “The Relationship Of Hardness And Strength In High-Strength Titanium Alloys.” *AeroMat 2017.* Charleston.

Leuders, S., M. Thöne, A. Riemer, T. Niendorf, T. Tröster, H. A. Richard, and H. J. Maier. 2013. “On the mechanical behaciour of titanium alloy Ti6Al4V manufactured by selective laser melting: Fatigue resistance and crack growth performance.” *International Journal of Fatigue* 300-307.

Leuders, S., M. Vollmer, F. Brenne, T. Tröster, and T. Niendorf. 2015. “Fatigue strength prediction for titanium alloy Ti6Al4V Manufactured by Selective Laser Melting.” *Metallurgical and Materials Transactions A.* ASM International.

Li, W., and J. Li. 1988. “The effect of grain size on fracture toughness.” *Philosophical Magazine A* 1245-1261.

Lütjering, G., Williams J.C., and A. Gysler. 2002. “Microstructure and Mechanical Properties of Titanium Alloys.” In *Microstructure and Properties of Materials*, by J.C.M. Li, 1-77. World Scientific.

2009. *makeitfrom.* Accessed June 11, 2019. https://www.makeitfrom.com/.

Masuo, H., Yuzo, Morokoshi, S. Tanaka, H. Yagura, T. Uchida, Y. Yamamoto, and Y Marukami. 2018. “Influence of defects, surface roughness and HIP on the fatigue strength of Ti6Al4V manufactured by additive manufacturing.” *International Journal of Fatigue* 163-179.

MatWeb LLC. 2017. *MatWeb*. Accessed March 15, 2017. http://www.matweb.com/search/AdvancedSearch.aspx.

Moyka, M., K. Kubiak, J. Sieniawski, and W. Ziaja. 2012. “Hot Plasticity of Alpha Beta Alloys.” In *Titanium Alloys - Towards Achieving Enhanced Properties for Diversified Applications*, by A.K.M Nurul Amin. IntechOpen.

Mughrabi, Heal. 2012. “Microstructural fatigue mechanicsms: Cyclic slip irreversibility, crack initiation, non-linear elastic damage analysis.” (Elsevier).

Murr, L.E., S.A. Quinones, S.M. Gaytan, M.I. Lopez, A. Rodela, E.Y. Martinez, D.H. Hernandez, E. Martinez, F. Medina, and R.B. Wicker. 2009. “Microstructure and mechanical behavior of Ti–6Al–4V produced by rapid-layer manufacturing, for biomedical applications.” *Journal of the Mechanical Behaviour of Biomedical Materials* 20-32.

Nicholas, T. 2002. “Step Loading for very high cycle fatigue.” *Fatigue Fract Engng Mater Struct* 861-869.

Pederson, R. 2002. “Microstructure and Phase Transformation of Ti6Al4V.” Luleå, May.

Perez, T.E. 2013. “Corrosion in the Oil and Gas Industry: An Increasing Challenge for Materials.” *Journal of The Minerals, Metals & Materials Society* 1033-1042.

Peters, J. O., G. Lütjering, R. K. Nalla, I. Altenberger, and R. O. Ritchie. 2002. “High-cycle fatigue of beta titanium alloys.” *Fatigue.*

Peters, J.O., O. Roder, B.L. Boyce, A.W. Thompson, and R.O. Ritchie. 2000. “Role of Foreign-Object Damage on Thresholds for High-Cycle Fatigue in Ti-6Al-4V.” *Metallurgical and Mateirals Transsactions A.*

Prasad Rao, K., K. Angamuthu, and P. Bala Srinivasan. 2008. “Fracture toughness of electron beam welded Ti6Al4V.” *Journal of materials processing technology* 185–192.

Qiu, C., N.J.E. Adkins, and M.M. Attallah. 2013. “Microstructure and tensile properties of selectively laser-melted and of HIPed laser-melted Ti–6Al–4V.” *Materials Science & Engineering A* 230-239.

Rafi, H.K., N.V. Karthik, H. Gong, T.L. Starr, and B.E. Stucker. 2013. "Microstructure and Mechanical Properties of Ti6Al4V Parts Fabricated by Selective Laser Melting and Electron Beam Melting." *Journal of Materials Engineering and Performance* 3872-3883.

Rafi, H.K., T.L. Starr, and B.E. Stucker. 2013. "A comparison of the tensile, fatigue, and fracture behavior of Ti–6Al–4V and 15-5 PH stainless steel parts made by selective laser melting." *International Journal of Manufacturing Technology* 1299–1309.

Razavi, S., P. Ferro, and F. Berto. 2017. "Fatigue Assessment of Ti–6Al–4V Circular Notched Specimens Produced by Selective Laser Melting." *Metals*.

Renishaw. 2019. *www.renishaw.com*. Accessed June 14, 2019. https://www.renishaw.com/en/data-sheets-additive-manufacturing--17862.

Sangrid, M. 2012. „The physics of fatigue crack initiation." (Elsevier) 58-72.

Schijve, J. 2004. *Fatigue of Structures and Materials*. Dordrecht: Kluwer Academic Publishers.

Sieniawski, J., W. Ziaja, K. Kubiak, and M. Motyka. 2013. "Microstructure and Mechanical Properties of High Strength Two-Phase Titanium Alloys." In *Titanium Alloys - Advances in Properties Control*, by J. Sieniawski, 69-80. IntechOpen.

Simonelli, M., Y.Y. Tsea, and C. Tuck. 2014. "Effect of the build orientation on the mechanical properties and fracture modes of SLM Ti–6Al–4V." *MaterialsScience&Engineering* 1-11.

Smith, J., W. Xiong, W. Yan, S. Lin, P. Cheng, O. Kafka, G. Wagner, J. Cao, and W. Liu. 2015. "Linking process, structure, property, and performace for metal-based additive manufacturing; computational approaches with experimental support." *Comput Mech*. Springer.

Spierings, A.B., K. Wegenert, and G. Levy. 2012. "Designing Material Properties Locally with Additive Manufacturing technology SLM." *SFF* 447-455.

2019. *Statistica*. Accessed March 5, 2019. https://www.statista.com/statistics/262858/change-in-opec-crude-oil-prices-since-1960/.

Sun, J., Y. Yang, and D. Wang. 2012. "Parametric optimization of selective laser melting for forming Ti6Al4V samples by Taguchi method." *Optics&LaserTechnology* 118-124.

Thijs, Lore, Frederik Verhaeghe, Tom Craeghs, Jan Van Humbeeck, and Jean-Pierre Kruth. 2010. "A study of the microstructural evolution during selective laser melting of Ti6Al4V." *Acta Materialia* 3303-3312.

Titanium Information Group. 2002. *Azo Materials*. 30 July. Accessed June 19, 2019. https://www.azom.com/properties.aspx?ArticleID=1547.

Van Hooreweder, B., D. Moens, R. Boonen, J. Kruth, and P. Sas. 2012. "Analysis of Fracture Toughness and Crack Propagation of Ti6Al4V Produced by Selective Laser Melting." *Advanced Engineering Materials*.

Vayssette, B.: Saintier, N., C. Brugger, M. Elmay, and E. Pessard. 2017. "Surface Roughness of Ti6Al4V parts obtained by SLM and EBM: Effect on the High Cycle Fatigue life." *7th International Conference on Fatigue Design*. Senlis, France: Elsevier. 89-97.

Vilaro, T., C. Colin, and J.D. Bartout. 2011. "As-Fabricated and Heat-Treated Microstructures of the Ti-6Al-V alloy processed by selective laser melting." *Metallurgical and Materials Transactions A*. ASM International.

Vrancken, Bey, Lore Thijs, Jean-Pierre Kruth, and Jan Van Humbeeck. 2012. "Heat treatment of Ti6Al4V produced by Selective Laser Melting: Microstructure and mechanical properties." *Journal of Alloys and Compounds* 177-185.

Vukovich, W. 2015. "Refinery Power Outages-Caues, Costs & Solutions." *AIChE Spring Meeting and Global Congress on Process Safety*. Austin: Hydrocarbon Publishing Co. https://www.aiche.org/academy/videos/conference-presentations/refinery-power-outages-caues-costs-solutions.

Witkin, David B., and Thomas V. Patel, Dhruv N. Albright. 2016. "Empirical Approach to Understanding the Fatigue Behaviour of Metals Made Using Additive Manufacturing." *Metallurgical and Materials Transactions A*.

Wong, K.W., and A. Hernandez. 2012. "A Review of AdditiveManufacturing." *ISRN Mechanical Engineering*.

Wu, M., and P. Lai. 2016. “The positive effect of hot isostatic pressing on improving the anisotropies of bending and impact properties in selective laser melted Ti-6Al-4V alloy.” *Materials Science & Engineering* 429–438.

Wu, M., P. Lai, and J. Chen. 2016. “Anisotropy in the impact toughness of selective laser melted Ti-6Al-4V alloy .” *Materials Science & Engineering.*

Wycisk, Eric, Claus Emmelmann, Shafaqat Siddique, and Frank Walther. 2013. “High Cycle Fatigue Performance of Ti6Al4V Processed by Selective Laser Melting.” *Advanced Mateirals Research* 134-139.

Yan, X., S. Yin, C. Chen, C. Huang, R. Bolot, R. Lupoi, M. Kuang, W. Ma, C. Coddet, and M. Liu. 2018. “Effect of heat treatment on the phase transformation and mechanical properties of Ti6Al4V fabricated by selective laser melting.” *Journal of Alloys and Compounds* 1056-1071.

Yang, J., H. Yu, J. Yin, M. Gao, Z. Wang, and X. Zeng. 2016. “Formation and control of martensite in Ti-6Al-4V alloy produced by selective laser melting.” *Materials and Design* 308-318.

Yang, J., H. Yu, Z. Wang, and X. Zeng. 2017. “Effect of crystallographic orientation on mechanical anisotropy of selective laser melted Ti-6Al-4V alloy.” *Materials Characterization* 137-145.

Yasa, Evren, Jan Deckers, Jean-Pierre Kruth, Marleen Rombouts, and Jan Luyten. 2010. “Charpy impact testing of metallic selective laser melting parts.” *Virtual and Physical Prototyping* 89-98.

Zhang, X., G. Fang, S. Leeflang, A. Böttger, A. Zadpoor, and J. Zhou. 2018. “Effect of subtransus heat treatment on the microstructure and mechanical properties of additively manufactured Ti-6Al-4V alloy.” *Journal of Alloys and Compounds* 1562-1575.

Zhao, X., S. Li, M. Zhang, Y. Liu, T.B. Sercombe, S. Wang, Y. Hao, R. Yang, and L.E. Murr. 2016. “Comparison of themicrostructures andmechanical properties of Ti–6Al–4V fabricated by selective laser melting and electron beam melting.” *Materials and Design* 21-31.

Zheng, Xiulin. 2001. “On some basic problems of fatigue research in engineering.” *International Journal of Fatigue* 751-766.

Zhu, Jia-Ning, Evgenii Borisov, Xiaohui Liang, Eduard Farber, and M.J.M.: Popovich, V.A. Hermans. 2021. “Predictive analytical modelling and experimental validation of processing maps in additive manufacturing of nitinol alloys.” *Additive Manufacturing.*

Appendix A

Stress intensity factor calculation and test of validity

In the section below fracture toughness K_{Ic} is calculated according to ASTM E399. The specific values for KL3 are taken as an example.

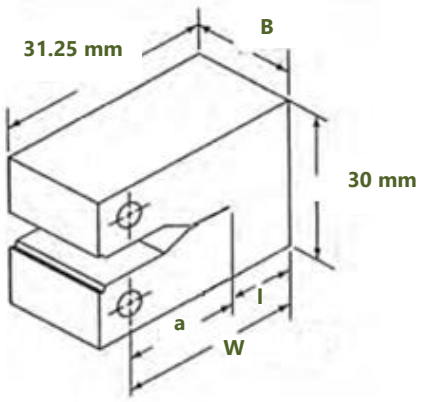

W_{KL8} = 25.1 mm

B_{KL8} = 11.8 mm

Figure 68: Compact tension test piece

Before testing a fatigue crack is induced into the sample, which is indicated in Figure 68.

The fatigue crack length must be measured at three positions. For ease this is measured from the back of the test piece giving ligament lengths of l_1 = 12.3 mm, l_2 = 12.4 mm, and l_3 = 11.6 mm, with an average of 12.1 mm. This in turn gives crack lengths of a_1 = 12.9 mm a_2 = 12.7 mm, and a_3 = 13.5 mm, with an average of 13.0 mm. This crack must meet a number of requirements for the end-result of the test to be a valid result.

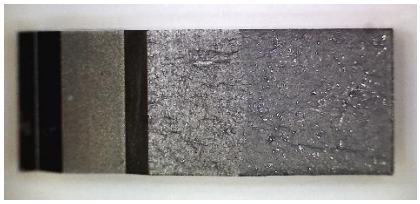

Figure 69: Fracture surface on KL3

1) The length of the pre-fatigue crack a must fall between 45 % and 55 % of the specimen width (W = 25.1mm), and it is in fact 52 %.

2) The variation in the length of the pre-fatigue crack may not be more than 15% from the average, and the greatest variation is between the average and a_3, which varies by 3.8 %.

3) The size of the fatigue crack on each face of the specimen shall not be less than 0.025 times the width (so 0.6 mm) or 1.3 mm, whichever is larger, and at 13.0 mm it falls easily within the requirement.

4) The fatigue crack and extension shall be parallel to the plane of the starter notch within 10° (excluding shear lips). The measured difference can be seen in Figure 70 and is approximately 0.8°.

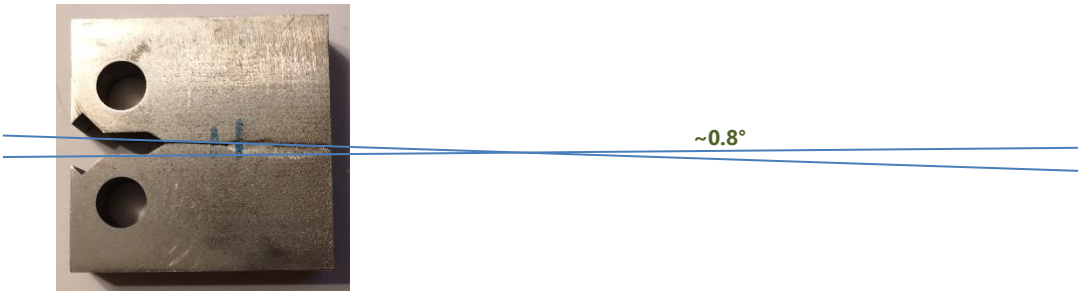

Figure 70: Angle of fracture surface to starter notch in KL3

Apart from the requirement for the prefatigued crack, there are also requirements for fracture in general.

5) The specimen must not fail by brittle cleavage fracture, and as can be seen in Figure 71 the fracture surface consists of dimples, indicating ductile fracture and not brittle cleavage fracture. No signs of cleavage were observed on the fracture surface.

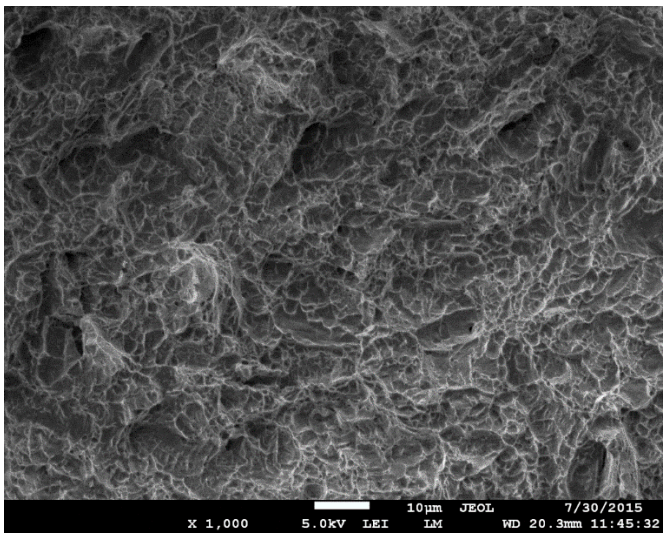

Figure 71: SEM image of fracture surface of KL3.

6) There should be no evidence of multiple cracking, and as can be seen in Figure 69 and Figure 70 this is the case.

In order to evaluate the rest of the criteria we need to look at the test results. The graph of tensile load against crack-tip opening displacement can be seen below in Figure 72. Here the maximum force P_{max} is 9.26 kN, and the force at the 5 % secant line P_q (green in the graph below) is 9.04 kN.

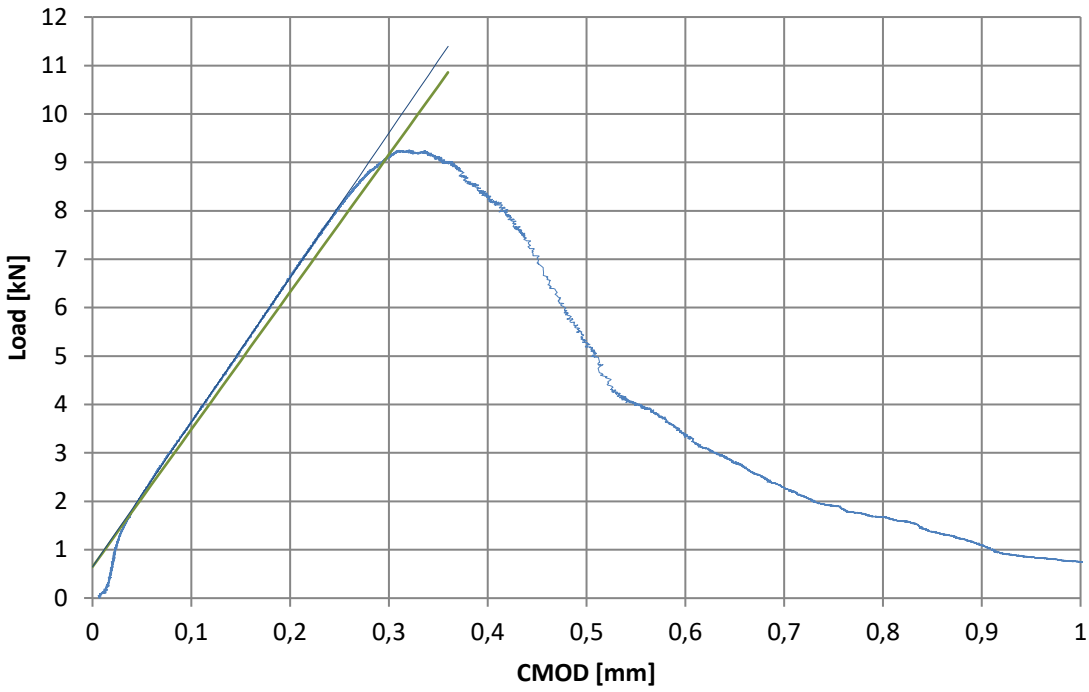

FIGURE 72: GRAPH OF CRACK TIP OPENING DISPLACEMENT AGAINST LOAD FOR KL3. THE 5% SECANT LINE IS IN GREEN.

Based on this we can calculate the conditional stress intensity factor K_Q as follows:

$$K_Q = \frac{P_Q}{B\sqrt{W}} \cdot f\left(\frac{a}{W}\right)$$

$$f\left(\frac{a}{W}\right) = \frac{\left(2+\frac{a}{W}\right)\left[0.886 + 4.64\frac{a}{W} - 13.32\left(\frac{a}{W}\right)^2 + 14.72\left(\frac{a}{W}\right)^3 - 5.6\left(\frac{a}{W}\right)^4\right]}{\left(1-\frac{a}{W}\right)^{1.5}}$$

$$K_Q = \frac{9040}{0.0118\sqrt{0.0251}} \cdot \frac{\left(2+\frac{0.0130}{0.0251}\right)\left[0.886 + 4.64\frac{0.0130}{0.0251} - 13.32\left(\frac{0.0130}{0.0251}\right)^2 + 14.72\left(\frac{0.0130}{0.0251}\right)^3 - 5.6\left(\frac{0.0130}{0.0251}\right)^4\right]}{\left(1-\frac{0.0130}{0.0251}\right)^{1.5}}$$

$$K_Q = \frac{9040}{0.0118\sqrt{0.0251}} \cdot \frac{(2.519)[1.358]}{0.334}$$

$$K_Q = \frac{9040}{0.0118\sqrt{0.0251}} \cdot 10.250$$

$$K_Q = 48.69 \text{ MPa}\sqrt{m}$$

Based on this we can take a closer look at the remaining criteria.

7) The ratio of the maximum applied force over the force at the 5% secant line may not be more than 1.1, and in this case it is 1.02.

8) The ligament size may not be less than $2.5(K_Q/\sigma_{YS})^2$. The yield strength in the longitudinal direction of stress relieved samples was measured at 677 MPa, which gives a minimum ligament size of 12.9 mm. The ligament size for this sample was 12.1 mm and as such this value for K_Q is not a valid value and was not used in the final results.

9) The maximum stress intensity factor during pre-fatigue may not have been larger than 80% of the calculated K_Q. The maximum applied force during pre-fatigue was 5.0 kN. The stress intensity increases with an increase in crack length for the same force, so the final crack length during pre-fatigue will be taken. This gives a stress intensity of 27.48 MPa$\sqrt{m}$, which is only 56 % of the calculated K_Q value.

10) During the terminal phase of pre-fatigue cracking the stress intensity factor may not have been larger than 60% of the calculated K_Q. It is in fact 56 % as seen above.

11) The loading rate shall be such that the increase in stress-intensity factor is between 0.55m and 2.75 MPa√m/s. Testing was performed at 0.2 kN/s which gives 1.1 MPa√m/s.

Based on the above calculations KL3 proved not to give a valid result for K_{IC}. Similarly KT3 was not valid (criteria 7), as well as HKL2 (criteria 2).